# The STAR Forward Calorimeter System and Forward Tracking System

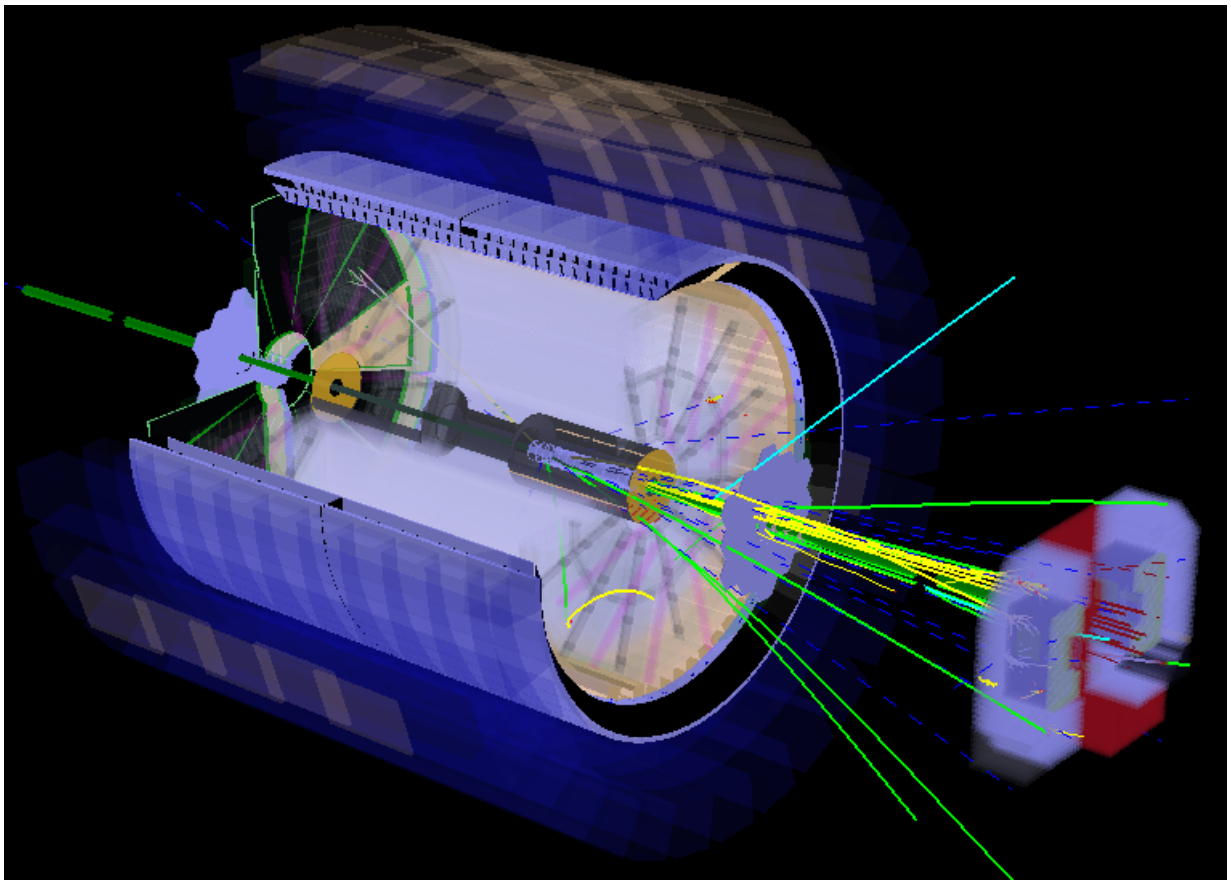

**January 2016**

This page intentionally left blank.

# 1 Executive Summary

The STAR collaboration proposes to construct a Forward Calorimeter System (FCS) and Forward Tracking System (FTS). The FCS and FTS will offer new detection capabilities at forward pseudo-rapidities and will enable a science driven program for future polarized p+p, polarized p+A, and A+A beam operations at RHIC in the time period after Beam Energy Scan phase II [1] and prior to the transition to eRHIC [2,3].

The main scientific goals of the polarized p+p, polarized p+A and A+A program are to study Quantum Chromo Dynamics (QCD) in the high and low Bjorken-*x* domain and to explore the properties of the strongly interacting Quark-Gluon Plasma (QGP). This program is driven by five overarching questions:

- *What is the nature of the spin of the proton?*
- *What is the multidimensional landscape of nucleons and nuclei?*
- *What is the nature of the initial state in nuclear collisions?*
- *What are the properties of the strongly interacting QGP?*

STAR's opportunities to address these and other questions were discussed in the STAR Decadal Plan for 2010-2020 [4] and subsequent Letters of Intent. The p+p and p+A document [5] is of particular relevance to the later part of the decade and the proposed FCS and FTS.

The proposed FCS and FTS upgrades were first envisioned in the STAR Decadal Plan [4] and represent a natural evolution of the growth of the STAR scientific program. Elements of these upgrades are anticipated to also become an integral part of the detector configuration at IP-6 in the eRHIC area, as outlined in the eSTAR LOI [6].

The envisioned beam operation periods with these upgrades and the primary science objectives are:

| **Species** | $\sqrt{s}$ | $L_{\text{delivered}}$ | **Goal** |
|---|---|---|---|
| Longitudinally polarized p+p | 500 GeV | 1 $\text{fb}^{-1}$ | Low *x* Gluon helicity |
| Transversely polarized p+p | 500 GeV | 1 $\text{fb}^{-1}$ | Transverse Momentum Dependent proton spin structure |
| transversely polarized p+A with 3 nuclei: C, Cu, Au | 200 GeV | 2.5 $\text{pb}^{-1}$ | Saturation and nuclear parton distributions |
| A+A: Au+Au (Pb+Pb) | 200 GeV | $10^9$ events | Longitudinal flow decorrelation, initial conditions, eta/s, multiple harmonics, event-shape engineering |

STAR proposes measurements of forward photons, electrons from $J/\psi$ and Drell-Yan processes, inclusive jet, dijet, and hadron/jet correlation probes at both 200 and 500 GeV center of mass energies, and demonstrates measurement capability and sensitivity through simulations. These measurements allow STAR to probe the fundamental structure of nucleons in new kinematic regimes, and where existing data still provide rather poor constraints. One aspect is the composition of nucleon spin in terms of quark and gluon degrees of freedom; the other is to go beyond the one-dimensional picture of nucleons in momentum-space by correlating the information on the individual parton contribution to the spin of the nucleon with its transverse momentum and spatial distribution inside the nucleon.

In p+A collisions, these measurements will enable STAR to study Cold Nuclear Matter (CNM). The proposed FCS and FTS provide kinematic access to very small momentum fractions $x$ in nuclei, facilitating investigations into the dynamics and nonlinear evolution effects in the regime of high gluon-density. The proposed upgrades and RHIC's extraordinary versatility are integral to these measurements.

In addition to QCD studies with polarized p+p and p+A collisions, the proposed upgrade will facilitate the determination of QGP properties in A+A collisions through improved measurements of the initial density fluctuations as well as the collective flow seeded by these fluctuations. The proposed forward upgrade will further quantify $\eta/s$ through improved understanding of initial conditions via measurements of longitudinal flow de-correlation, multiple harmonics and event-shape engineering in A+A collisions, and will allow studies of the possible existence of and limits on hydrodynamics and jet-medium interaction in small systems at RHIC energies.

In section 2 of this document, we paraphrase the scientific motivation for the FCS and FTS upgrades and beam operations. Section 3 presents an overview of the FCS and FTS and discusses their simulated capabilities. The respective designs are described in sections 4 and 5, followed by the management plan in section and current understanding of cost and schedule in section 6.

# 2 The Physics of the Forward Upgrade

## 2.1 Introduction

Quantum Chromodynamics (QCD), the theory of strong interactions, is a cornerstone of the Standard Model of modern physics. It explains all strongly interacting matter in terms of point-like quarks interacting via the exchange of gauge bosons, known as gluons. This strongly interacting matter is responsible for 99% of the visible mass in the universe. Over the past several decades, QCD has proven to be a remarkably rich theory. Many areas are subject to advanced calculational techniques and quite remarkable observations have been made in experiment.

RHIC has found that the dense QCD matter created in relativistic Au+Au collisions demonstrates very strong collective flow characteristic of a strongly-coupled liquid, rather than the weakly-coupled gas of quarks and gluons that had been expected. While the search for new phenomena (e.g. the critical point) continue to be at the forefront of hot QCD research, considerable efforts have been exerted to turn many qualitative observations into quantitative measurements. Excellent progress has been made in the last decade in quantitative extractions of shear viscosity ($\eta/s$) and transport coefficient ($\hat{q}$), and the inferred equation of state as a function of temperature in a Bayesian framework through the comparison of theoretical models to the vast amount of data obtained at RHIC and at the LHC.

The initial observation of a dramatic broadening of forward $\pi^0$-$\pi^0$ correlations in d+Au collisions provides indication that the non-linear QCD regime of gluon self-interaction may be accessible at RHIC and calls for a systematic exploration with alternate systems and polarization. Theoretical developments point to a potential connection between gluon saturation and the "ridge".

Longitudinally polarized p+p collisions have revealed that the spins of gluons with fractional momenta $0.05 < x < 0.2$ form a quite sizable and positive contribution to the proton spin. Transversely polarized p+p collisions show that the large-rapidity transverse single-spin asymmetries that had been observed at lower energies persist to RHIC energies where, in contrast to the lower energy results, the cross-sections can be described with perturbative QCD techniques.

These developments set the stage for compelling future research opportunities with STAR in the time period after the Beam Energy Scan phase II. The overarching questions are:

- *What is the nature of the spin of the proton?*
- *What is the multidimensional landscape of nucleons and nuclei?*
- *What is the nature of the initial state in nuclear collisions?*
- *What are the properties of the strongly interacting QGP?*

STAR's success has thus far been driven by the vigorous pursuit of a very well-developed mid-rapidity detector with particle identification capabilities. The proposed Forward Calorimeter System and Forward Tracking System will extend STAR's measurement capabilities to forward rapidities, which are essential to gain sensitivity to the thus-far unexplored gluon spin phenomena at small fractional momenta, $x$, and the gluon-dense environment in p+A collisions, and provides essential new measurement capabilities for A+A collisions. Together with its mid-rapidity counterpart, the FCS and FTS will provide the wide kinematic coverage necessary to address these questions prior to the transition to eRHIC.

## 2.2 Probing the Nucleon and Transverse Spin Phenomena in QCD

**Note: Section 2.2 and 2.3 represent the status of our understanding and thinking documented in the STAR pp /pA LoI from June 2014. Parts of the physics described has been updated in the RHIC SPIN WP (arXiv:1501.01220) and the RHIC QCD Plan from January 2016. Further some of the described measurements have already been realized during the 2015 RHIC run.**

Much of our present knowledge of nucleon structure comes from deep-inelastic lepton-nucleon scattering (DIS) experiments, with a great wealth of data on the unpolarized structure of the proton available from HERA [7]. From HERA, we have learned that quarks carry 50% of the momentum of the proton, with the other half carried by gluons, which dominate for $x$ <0.1.

Despite all that has been learned through DIS measurements, studying nucleon structure in a wide variety of reactions is essential in order to piece together a complete picture. Hadron-hadron interactions offer several advantages. Direct access to gluons is possible through parton-parton scattering, making the measurement of the spin contribution of the gluon to the spin of the proton a key component of the RHIC program.

W-Boson production and the Drell-Yan process are both golden probes to cleanly access antiquark distributions in hadron-hadron collisions. Drell-Yan processes will become an increasingly important part of the future RHIC p+p and p+A program. Comparing observations from DIS and hadronic interactions also allows us to test the assumptions of universality across processes in describing hadron structure and hadronization within the framework of perturbative QCD (pQCD).

In the high-energy limit of pQCD, calculations in which the quarks and gluons are treated as nearly free particles moving collinearly with their parent hadron, and in which hadronic interactions are assumed to factorize into a) parton distribution functions (PDFs) within the initial-state hadron, b) partonic hard-scattering cross-sections, and c) fragmentation functions (FFs) describing the hadronization of the scattered parton, have had tremendous success in describing hadronic cross-sections at high energies over the past several decades. The collider energies available at RHIC put high-$p_T$ reactions comfortably within a regime described by factorized pQCD. It is worth noting that the relevant perturbative scale in DIS is $Q^2$, while in hadron-hadron interactions it is the square of the transverse momentum ($p_T^2$) of the produced jet or particle, and while both $Q^2$ and $x$ are known in DIS, in hadron-hadron measurements the $p_T$ of the produced particle is correlated with $x$, but a given $p_T$ bin typically samples from a range of $x$ values.

At high energy, there remain two fundamental aspects of the nucleon partonic structure which are rather poorly determined by experiment. One is the nature of the nucleon spin; the other is to go beyond our current simple one-dimensional picture of nucleons by correlating the information on the individual parton contribution to the spin of the nucleon with its transverse momentum and spatial distribution inside the nucleon.

### 2.2.1 Gluon Polarization

The measurement of the gluon polarization in a polarized proton has been a major emphasis and strength of the spin physics program at RHIC since its inception [8]. RHIC has completed very successful polarized p+p runs at $\sqrt{s}$ = 200 GeV, $\sqrt{s}$ = 500 GeV, and $\sqrt{s}$ = 510 GeV. Table 2-1 summarizes the collision energies, STAR recorded luminosities, and the average polarization values for runs since 2006.

| Year | $\sqrt{s}$ (GeV) | Recorded Luminosity for longitudinally polarized p+p | <P> |
|---|---|---|---|
| 2006 | 200 | 6.8 $pb^{-1}$ | 57 |
| 2009 | 200 | 25 $pb^{-1}$ | 55 |
| | 500 | 10 $pb^{-1}$ | 39 |
| 2011 | 500 | 12 $pb^{-1}$ | 48 |
| 2012 | 510 | 82 $pb^{-1}$ | 50/53 |
| 2013 | 510 | 300 $pb^{-1}$ | 50/53 |
| 2015 | 200 | 50 $pb^{-1}$ | 60 |

Table 2-1: STAR recorded luminosities for collisions of longitudinally polarized proton beams at the indicated center-of-mass energy for runs since 2006. The bottom row reflects the STAR beam use request for 2015.

The previously recorded $\sqrt{s}$ = 200 GeV data have been analyzed and published [9,10,11,12]. The 2009 STAR data on the spin asymmetry $A_{LL}$ in the inclusive production of jets are shown in Figure 2-1, together with preliminary data at RHIC's top-energy of $\sqrt{s}$ = 510 GeV. The 2009 data are particularly impactful in perturbative QCD analyses of world-data on polarized parton distribution functions, where they provide the first direct evidence for positive gluon polarization in the Bjorken-$x$ range $x > 0.05$ at a level similar to the combined quark and anti-quark polarization. To illustrate its impact, the STAR collaboration has incorporated the 2009 data using the reweighting method developed by the NNPDF group [13], which allows the inclusion of new experimental data into an existing PDF set without the need to repeat the entire fitting process. The results are shown in Figure 2-2. The integral of $\Delta g(x,Q^2=10\ \mathrm{GeV}^2)$ over the range $0.05 < x < 0.5$ is $0.06 \pm 0.18$ for the original NNPDF fit and $0.21 \pm 0.10$ when the fit is reweighted using the STAR jet data. The DSSV group has performed a new global analysis [14] including the STAR jet $A_{LL}$ results. They find that the integral of $\Delta g(x,Q^2=10\ \mathrm{GeV}^2)$ over the range $x > 0.05$ is $\mathbf{0.20^{+0.06}_{-0.07}}$ at 90% C.L., consistent with the value STAR finds by reweighting the NNPDF fit. More recently, the NNPDF group has published a new analysis [15], again finding a significant contribution from gluon spin to the proton spin. This presents a highly significant advance over the previous body of world-data, as is illustrated by a comparison of the fit results in Figure 2-3, which is reproduced from the new DSSV analysis [14]. The "new fit" includes the 2009 jet $A_{LL}$ data, unlike the original DSSV and DSSV* fits which include the less precise 2006 data. A factor of three improvement in uncertainty in $\Delta g$ over the measured range in $x$ is seen.

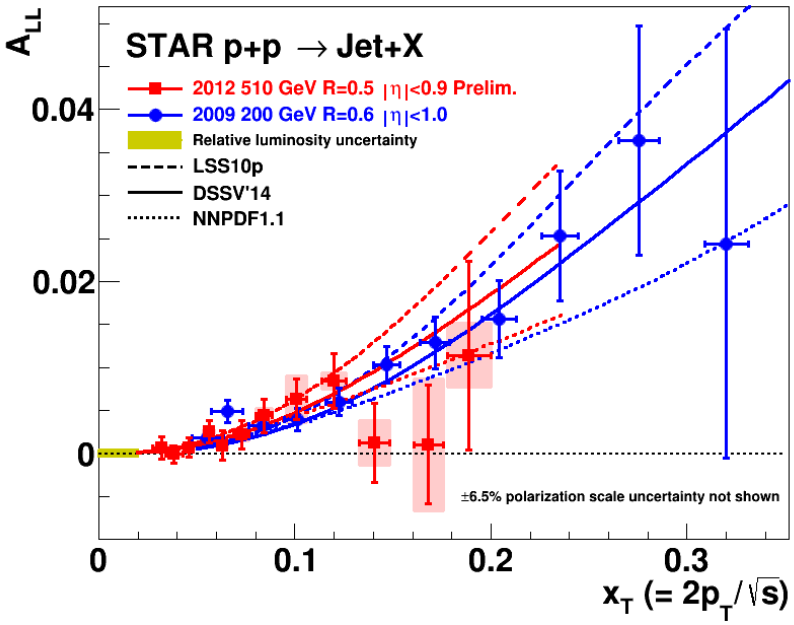


Figure 2-1 $A_{LL}$ vs. $x_T$ for inclusive jet production at mid-rapidity in 200 GeV (blue circles) [12] and 510 GeV (red squares) $p$+$p$ collisions, compared to predictions from three recent NLO global analyses [14,15,16] (blue curves for 200 GeV and red curves for 510 GeV).

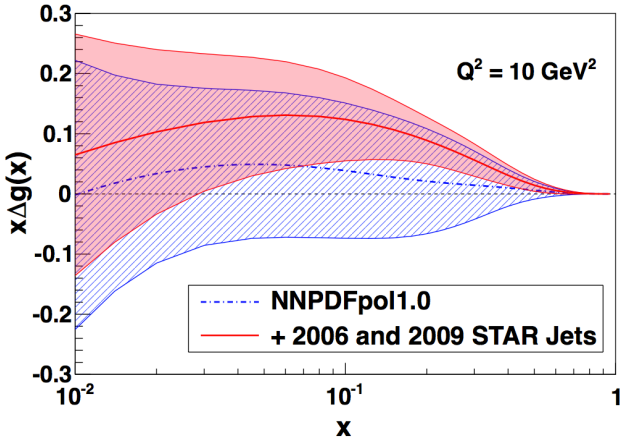


Figure 2-2: Gluon polarizations from NNPDF (blue dot-dashed curve, hatched uncertainty band), and from a modified version of NNPDF obtained by including the STAR 2006 and 2009 inclusive jet $A_{LL}$ results through reweighting (red continuous curve and uncertainty band).

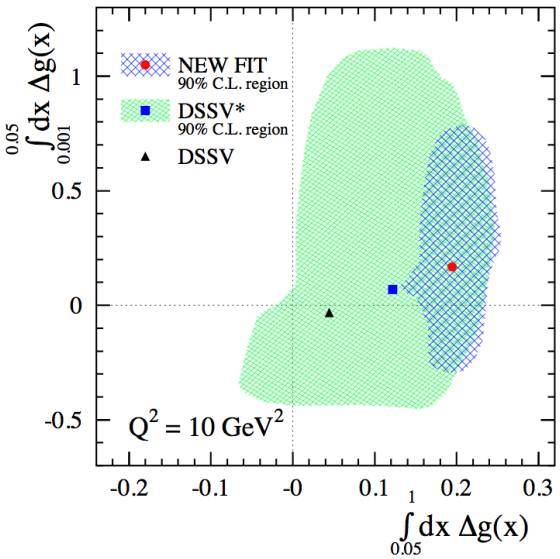


Figure 2-3: 90% confidence level areas in the plane spanned by the truncated moments of $\Delta g$ computed for $0.05 < x < 1$ and $0.001 < x < 0.05$ at $Q^2 = 10$ GeV$^2$. Results for the DSSV and DSSV* analyses, which include STAR 2006 data, and the new analysis [14] that includes the STAR 2009 data are shown.

The analysis of 2011-2013 data is in progress, with first preliminary data at the top RHIC energy having been released at the SPIN-2014 conference (c.f. Figure 2-2). Together with data collected in the proposed running period in 2015, a further improvement by a factor of about two in precision is anticipated as shown in Figure 2-4 and Figure 2-5. The top-energy data will also extend to 2.5 times lower $x$ values for equal jet $p_T$, down from $x \sim 0.05$ to $x \sim 0.02$.

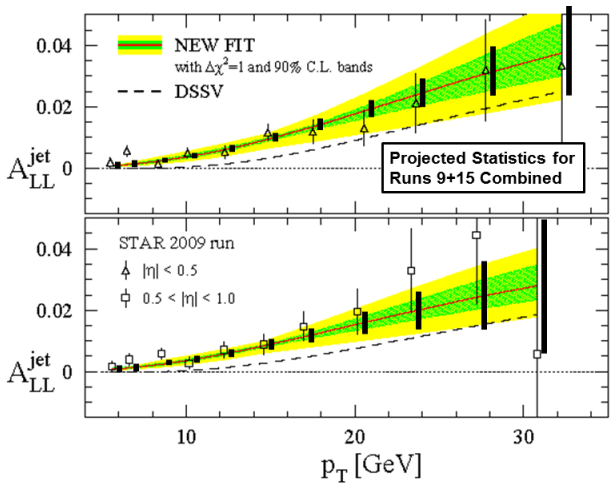


Figure 2-4: The projected statistical precision for $A_{LL}$ vs. $p_T$ for inclusive jets in 200 GeV $p$+$p$ collisions based on the combined data from the 2009 and 2015 RHIC runs, compared to the uncertainties from the DSSV-2014 fit, which included the 2009 inclusive jet results among the inputs.

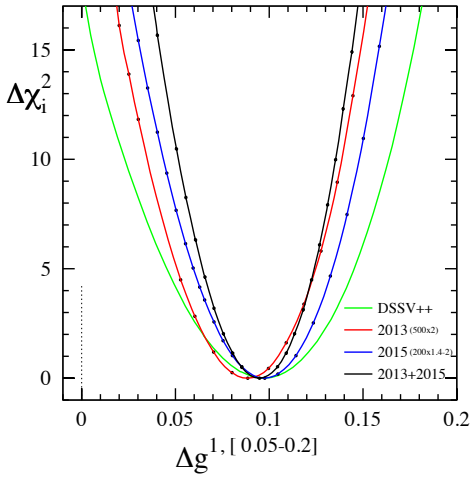


Figure 2-5: The improvement of the $\chi^2$ profile for the integrated gluon contribution in the $x$ region currently probed at RHIC for $\sqrt{s}$ = 200 GeV. The different curves represent including different data sets, red including the $\sqrt{s}$ = 510 GeV data from Run-12 and Run-13 (red), blue including the expected data from Run-15 (blue) and black represent a fit to all data at once.

The contour of the truncated $\Delta g$ integral for the measured and unmeasured $x$-region in Figure 2-3 demonstrates convincingly that the thus-far unobserved small-$x$ region is of paramount importance to the understanding of the gluon spin contribution to the proton spin. Future STAR analyses and proposed measurements aim to address this issue a) by using correlated probes to gain more direct sensitivity to $x$-dependence than is possible with inclusive probes and b) by extending the measurements to forward pseudo-rapidity with the proposed FCS and FTS. The combination forms a world-wide unique opportunity prior to eRHIC.

Measurements of beam-spin dependence of dijet production in STAR will allow better constraints of the underlying event kinematics to constrain the shape of the gluon polarization [17]. Initial dijet measurements with relevant precision have been obtained from data collected during the 2009 running period, Run 9 [18]. The invariant dijet mass, $M$, is related to the product of the initial partonic $x$ values, $x_1 \cdot x_2$, in $2 \rightarrow 2$ processes, whereas the pseudo-rapidity sum $\eta_3 + \eta_4$ is related to the ratio $x_1/x_2$ of the partonic $x$ values, since $M^2 = s \cdot x_1 \cdot x_2$ and $\eta_3 + \eta_4 = \ln(x_1/x_2)$ based on elementary four-vector kinematics. Measurements at both $\sqrt{s}$=200GeV and at $\sqrt{s}$=500GeV are preferred to maximize the kinematic region in $x$. The wide acceptance of the STAR experiment permits the reconstruction of dijet events with different topological configurations, i.e. different $\eta_3/\eta_4$ combinations, ranging from symmetric ($x_1 = x_2$) partonic collisions to asymmetric ($x_1 < x_2$ or $x_1 > x_2$) partonic collisions. In particular, it is the access to the large $\eta_3$ / $\eta_4$ region which allows to probe gluons in QCD processes at very small $x$-values. The proposed FCS and FTS will cover a nominal range in $\eta$ of $2.5 < \eta < 4.0$.

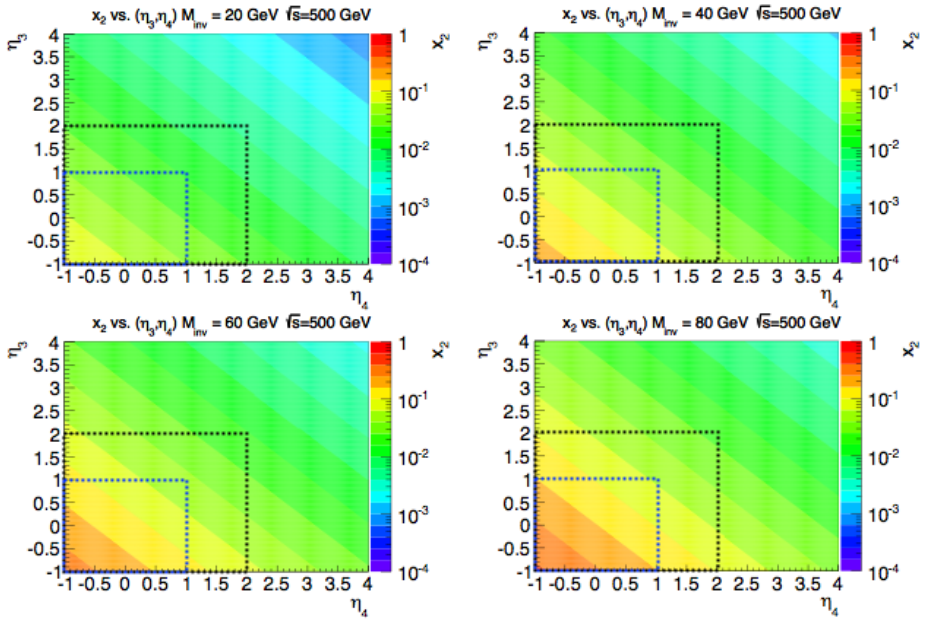


Figure 2-6: Low-$x$ coverage ($x_2$) shown as a color shade for dijet (2-to-2) final states showing $\eta_3$ and $\eta_4$ for four different invariant mass values of $M$ = 20, 40, 60 and 80 GeV.

Figure 2-6 illustrates the lower $x$-range covered for a dijet final state of four different invariants mass values of $M$ = 20, 40, 60 and 80 GeV. The actual $x$ values are displayed in a color shade as a function of $\eta_3$ and $\eta_4$ both for the current ($-1.0 < \eta < 2.0$) and the proposed forward ($2.5 < \eta < 4.0$) acceptance regions. The black and blue dashed lines indicate the region for which results have been released (black) and the region for which STAR has been fully instrumented (blue) without yet releasing any results as of now. One can clearly see that the current $\eta$-range only allows us to probe a region in $x$ of approximately $0.05 < x < 0.2$. Extending the current region to include the EEMC region of $1.1 < \eta < 2.0$ would expand the $x$ range of the measurements down to at least $10^{-2}$. The FCS and FTS, covering $2.5 < \eta < 4.0$, will extend the kinematic acceptance by an order of magnitude to $x$ values as low as $10^{-3}$, as is demonstrated in section 3.4.3.

### 2.2.2 Transverse Spin Phenomena

A natural next step in the investigation of nucleon structure is an expansion of our current picture of the nucleon by imaging the proton in both momentum and impact parameter space. At the same time we need to further our understanding of color interactions and how they manifest themselves in different processes. In the new theoretical framework of transverse momentum dependent (TMD) parton distributions we can obtain an image in both transverse and in longitudinal momentum space (2+1 dimensions). This has attracted renewed interest, both experimentally and theoretically, in transverse single-spin asymmetries (SSA) in hadronic processes at high energies, which have a more than 30 year history. Measurements at RHIC have extended the observations from the fixed-target energy range to the collider regime, up to and including the highest center-of-mass energies to date in polarized p+p collisions. Figure 2-7 summarizes the measured asymmetries from different experiments as functions of Feynman-$x$ ($x_F \sim x_1$-$x_2$).

The surprisingly large observed asymmetries are nearly independent of $\sqrt{s}$ over a very wide range. To understand the observed SSAs, one has to go beyond the conventional collinear parton picture in the hard processes. Two theoretical formalisms have been proposed to explain sizable

SSAs in the QCD framework. These are: transverse momentum dependent parton distributions and fragmentation functions, such as the Sivers and Collins functions discussed below; and transverse-momentum integrated (collinear) quark-gluon-quark correlations, which are twist-3 distributions in the initial state proton or in the fragmentation process. For many spin asymmetries, several of these functions can contribute and need to be disentangled to understand the experimental observations in detail, in particular the dependence on $p_T$ measured in the final state. The functions express a spin dependence either in the initial state (such as the Sivers distribution or its Twist-3 analog, the Efremov-Teryaev-Qiu-Sterman (ETQS) function [19]) or in the final state (via the fragmentation of a polarized quarks, such as the Collins function).

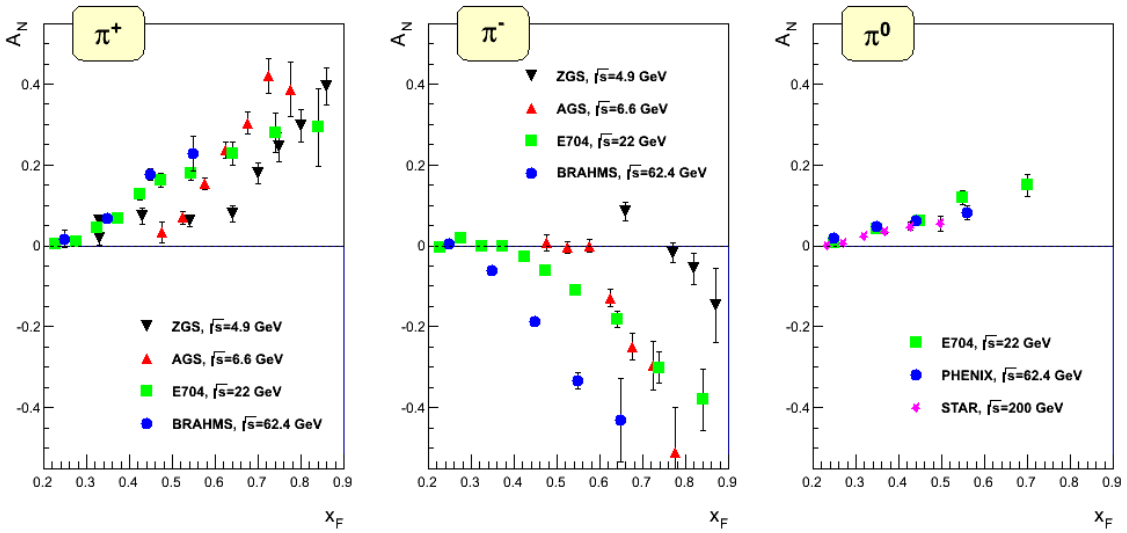


Figure 2-7: Transverse single-spin asymmetry measurements for charged and neutral pions at different center-of-mass energies as function of Feynman-*x*.

The Sivers function, $f_{1T}^{\perp}$, describes the correlation of the parton transverse momentum with the transverse spin of the nucleon. A non-vanishing $f_{1T}^{\perp}$ means that the parton distribution will be azimuthally asymmetric in the transverse momentum space relative to the nucleon spin direction. The Sivers function, $f_{1T}^{\perp}$, is correlated with the ETQS functions, $T_{q,F}$, through the following relation:

$T_{q,F}(x,x) = -\int d^2k_\perp \frac{|k_\perp|^2}{M} f_{1T}^{\perp q}(x,k_\perp^2)|_{SIDIS}$ [Eq. 2-1].

In this sense, a measurement constraining the ETQS function indirectly also constrains the Sivers function. We will use this connection repeatedly.

The Collins function, $H_1^{\perp}$, describes a correlation of the transverse spin of a scattered quark and the transverse momenta of the fragmentation products and as such can lead to an asymmetry of the distribution of hadrons in jets. Contrary to the Sivers effect, the Collins fragmentation function is universal among different processes: SIDIS, $e^+e^-$ annihilation, and p+p collisions. This is of special importance to the p+p case where it is always coupled to the chirally odd quark transversity distribution, which describes the transverse spin preference of quarks in a transversely polarized proton.

STAR has pioneered in the last years the research in p+p collisions to identify observables that will help to separate the contributions from initial and final states, and will give insight to the transverse spin structure of hadrons. In the following discussion, we will outline how the current and future STAR data and the FCS and FTS upgrades in particular will help to answer the following forefront questions:

- *Do the large transverse single-spin asymmetries survive at high center-of-mass energies?*
- *Can the subprocess responsible for $A_N$ be uniquely identified?*
- *Is the observed $p_T$-dependence of $A_N$ consistent with theory expectations in pQCD*
- *Can the TMD evolution, which is different from the well-known DGLAP evolution, be observed in the RHIC data?*

Our current understanding is based on the already taken or soon to-be-taken data sets listed in Table 2-2.

| Year | √s (GeV) | Recorded Luminosity for transversely polarized p+p | <P> |
|---|---|---|---|
| 2006 | 200 | 8.5 $pb^{-1}$ | 57 |
| 2008 | 200 | 7.8 $pb^{-1}$ | 45 |
| 2011 | 500 | 25 $pb^{-1}$ | 53/54 |
| 2012 | 200 | 22 $pb^{-1}$ | 61/58 |
| 2015 | 200 | 50 $pb^{-1}$ | 60 |
| 2016 | 500 | 400 $pb^{-1}$ (7w) / 900 $pb^{-1}$ (14w) | 50 |

Table 2-2: Luminosity and beam polarizations recorded by STAR in the past transverse polarized p+p runs from 2006 onward. The luminosities and polarizations listed for 2015 and 2016 are projected.

STAR primary contributions to transverse spin physics have been through the study of forward neutral pion production in p+p collisions (see, for example, ref. [20,21]). This effort has been extended to include the first measurements at $\sqrt{s}$ = 200 GeV of the transverse spin asymmetry $A_N$ for the $\eta$ meson [22]. The Run-11 data taken with transverse polarization at $\sqrt{s}$ = 500 GeV have revealed several surprising results. Figure 2-8 shows the transverse single-spin asymmetry $A_N$ for electromagnetic jets detected in the forward meson spectrometer (FMS) at $2.5 < \eta < 4.0$ as a function of the jet $p_T$ for different photon multiplicities and jet energy ranges. It can be clearly seen that with the increasing number of photons in the electromagnetic jet (increasing "jettiness" of the event) the asymmetry becomes smaller. Jets with an isolated $\pi^0$ have the largest asymmetry consistent with the asymmetry in inclusive $\pi^0$ events, as seen from the right-most panel in Figure 2-7. For all jet energies and photon multiplicities in the jet, the asymmetries are essentially flat as a function of jet $p_T$, a feature also previously observed for inclusive $\pi^0$ asymmetries. Recently, it has been proposed that in the collinear, twist-3 factorization approach a significant portion of the sizable inclusive pion asymmetries observed at forward pseudorapidity is due to twist-3 fragmentation functions coupled to transversity [23]. This calculation is the first one which showed a flat $p_T$ dependence for $A_N$, consistent with experiment [24]. The ability for this approach to describe adequately the effects observed in at SIDIS and in p+p collisions at RHIC is a potentially significant breakthrough in the long-standing mystery surrounding the non-zero inclusive asymmetries at forward pseudorapidity (e.g. Ref. [25]). Although this is a rapidly developing field, it is clear that the most desirable kinematic region for future study at RHIC is in the region of $\eta > 2$ covered by the proposed FCS and FTS.

To further study these effects, the transverse single-spin asymmetry $A_N$ of these electromagnetic jets was also measured requiring, in addition, a correlated away side jet in the rapidity range $-1 < \eta < 2$. Figure 2-9 shows clearly that for requiring an additional correlated away-side jet, the asymmetry for isolated forward $\pi^0$ mesons becomes smaller. For further details see

reference [26]. Both of these observations raise serious questions regarding how much of the large forward $\pi^0$ asymmetries are caused by 2→2 parton scattering processes.

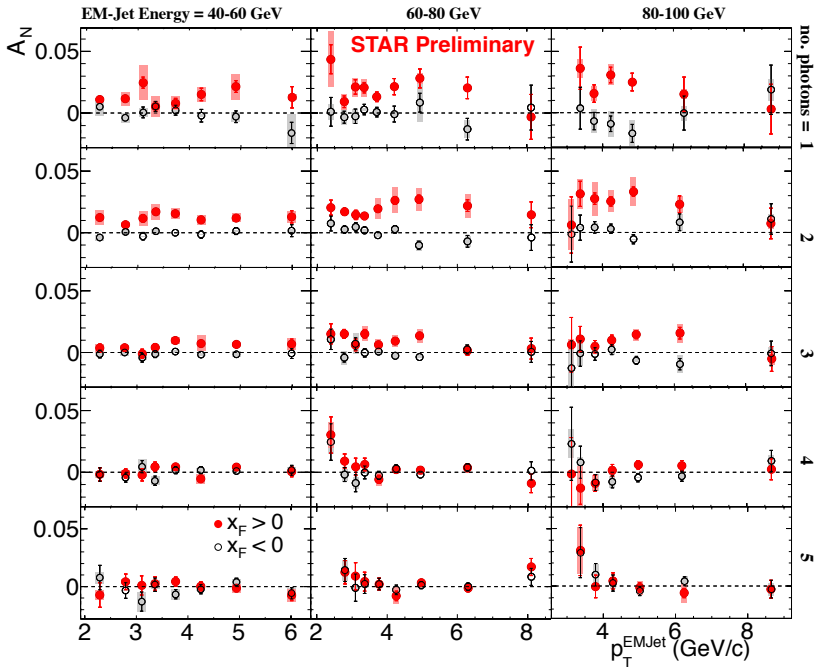


Figure 2-8: The transverse single-spin asymmetry $A_N$ for electromagnetic jets detected in the forward meson spectrometer ($2.5 < \eta < 4.0$) as function of the jet $p_T$ and the photon multiplicity in the jet in bins of the jet energy.

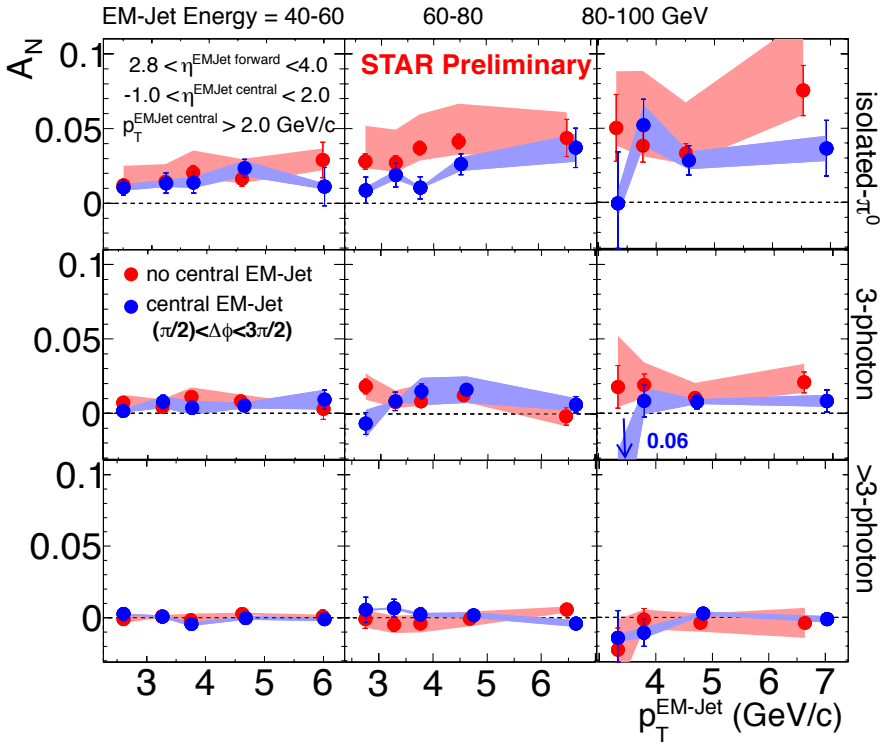


Figure 2-9: The transverse single-spin asymmetry $A_N$ for electromagnetic jets detected in the forward meson spectrometer ($2.5 < \eta < 4.0$) as a function of the jet $p_T$ and the photon multiplicity in the jet, in bins of the jet energy (red points). The blue points represent the transverse single-spin asymmetry $A_N$ if further a correlated away side jet in the rapidity range $-1 < \eta < 2$ was required. The blue and red bands represent the systematic

uncertainties.

To disentangle the different subprocesses it is important to identify less inclusive measurements (which are particularly sensitive to certain processes). Table 2-3 identifies observables that allow the separation of the contributions from polarization effects in the initial and final states, and will give insight to the transverse spin structure of hadrons. At this point we should emphasise that most observables in p+p collisions can only be related to the transverse spin structure of hadrons through the Twist-3 formalism, where only one hard scale is required. This is typically the $p_T$ of a produced particle or jet, which at RHIC is sufficiently large in much of the phase space. By contrast, the TMD framework requires two hard scales, $p_T$ and $Q$ with $p_T << Q$. Dijets, azimuthal dependences of hadrons within a jet, *W, Z,* or Drell-Yan production are observables in p+p collisions providing two such scales.

| **Initial State** | **Final State** |
|---|---|
| $A_N$ as function of rapidity, $E_T$, $p_T$ and $x_F$ for inclusive jets, direct photons and charmed mesons | $A_{UT}$ as a function of the azimuthal dependence of the correlated hadron pair on the spin of the parent quark (transversity × interference fragmentation function) |
| $A_N$ as a function of rapidity, $p_T$ for $W^{\pm}$, $Z^0$ and DY | Azimuthal dependences of hadrons within a jet (transversity × Collins fragmentation function) |
| | $A_N$ as function of rapidity, $p_T$ and $x_F$ for inclusive identified hadrons (transversity × Twist-3 fragmentation function) |

Table 2-3: Observables to separate the contributions from initial and final states to the transverse single-spin asymmetries. Two-scale processes are indicated in blue and one-scale ones in black.

An important aspect of the Sivers effect, which has emerged from theory, is its process dependence and the color gauge invariance. In SIDIS, the quark Sivers function is manifested in association with a final state effect from the exchange of (any number of) gluons between the struck quark and the remnants of the target nucleon. On the other hand, for the virtual photon production in the Drell-Yan process, the Sivers asymmetry appears as an initial state interaction effect. As a consequence, the quark Sivers functions are of opposite sign in these two processes and this non-universality is a fundamental prediction from the gauge invariance of QCD. The experimental test of this sign change is one of the open questions in hadronic physics (NSAC performance measure HP13) and will provide a direct verification of QCD factorization. The COMPASS experiment at CERN is pursuing this sign change through DY using a pion beam and new initiatives have been proposed e.g. at FNAL.

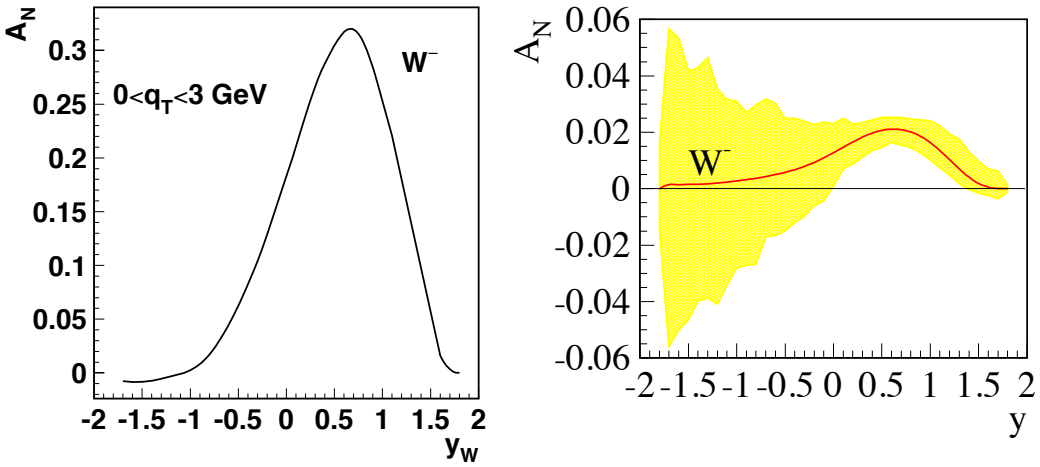


Figure 2-10: (left) Prediction for Sivers asymmetry $A_N$ as a function of $W^-$ boson rapidity at $\sqrt{s}$=500 GeV [31] **before any TMD evolution is applied. (right)** Theoretical predictions from reference [29] for $W^-$ for 0 GeV $< p_T <$ 3 GeV after TMD evolution is applied. The yellow bands represent the uncertainties for the asymmetry. At negative rapidity this is mainly caused by the currently unconstrained sea quark Sivers functions.

While the required luminosities and background suppressions for a meaningful measurement of asymmetries in Drell-Yan production are challenging, other channels can be exploited in p+p collisions which are similarly sensitive to the predicted sign change. These include prompt photons, $W^{\pm}$ and Z bosons, and inclusive jets. These are either already accessible with the existing STAR detector or need only modest upgrades and require continued polarized beam operations.

Figure 2-10 shows the predicted $A_N$ for $W^-$ **before** [31] (left) and after [29] (right) **TMD evolution is taken into account**. Lately, there have been several theoretical predictions for the transverse single-spin asymmetries for DY, $W^{\pm}$ and $Z^0$ bosons including TMD evolution, for examples see [27,28,29] and references therein. In all cases the asymmetries have been significantly reduced. The TMD evolution equations contain in addition to terms that can be calculated in QCD, non-pertubative terms, whose parameters need to be obtained from fits to data. Unfortunately there is not yet a consensus as to how to obtain and handle the non-pertubative input in the TMD evolution, for details see [30]. This complication leads to large uncertainties in the prediction for the DY, $W^{\pm}$ and $Z^0$ SSA, which can only be addressed by future measurements.
The transversely polarized data set in Run-2011 at $\sqrt{s}$ = 500 GeV allowed STAR to reconstruct the transverse single-spin asymmetries for $A_N$ for $W^{\pm}$ and $Z^0$ bosons. The measurement of the $A_N$ for $W^{\pm}$ bosons is especially challenging where, contrary to the longitudinally polarized case, it is required to completely reconstruct the $W$ bosons as the kinematic dependences of $A_N$ can not easily be resolved through the high $p_T$ decay lepton, for details see [31,32]. Due to the large STAR acceptance it was possible to reconstruct the $W$ boson kinematics from the recoil jet, a technique used at D0, CDF and the LHC experiments to reconstruct the $W$ boson kinematics. Figure 2-11 shows the transverse single-spin asymmetries for $A_N$ for $W^{\pm}$ as a function of the $W$ boson rapidity $y$. The asymmetries have also been reconstructed as a function of the $p_T$ of the $W$ boson. For the $Z^0$ boson the asymmetry could only be reconstructed in one bin in $y$ with the current limited statistics (25 $pb^{-1}$). Details for this analysis can be found in [33]. The analysis represents an important proof of principle, similar to the first Run-9 $W^{\pm}$ $A_L$ measurement.

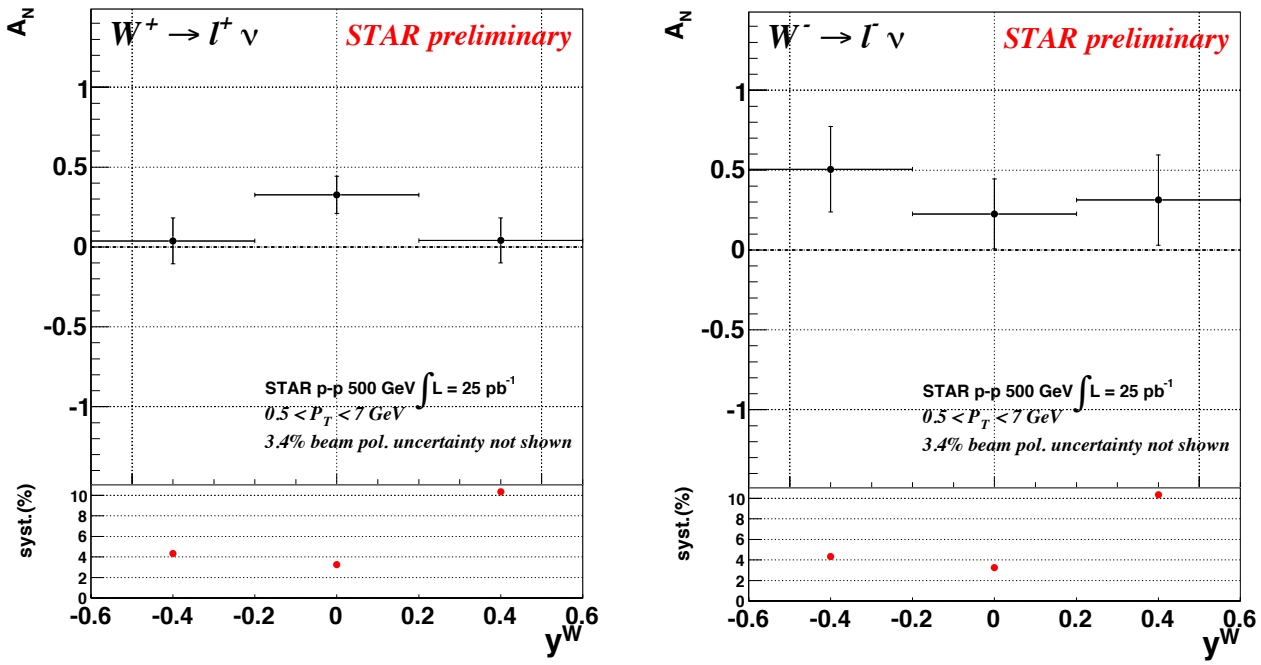


Figure 2-11: The transverse single-spin asymmetries for $A_N$ for $W^{\pm}$ as function of the $W$ boson rapidity $y$.

$W^{\pm}$ boson production provides an ideal tool to study the spin-flavor structure of sea quarks inside the proton. Such a measurement of the transverse single-spin asymmetry will provide the very first constraint on the sea quark Sivers function in an $x$-range where the measured asymmetry in the $\bar{u}$ and $\bar{d}$ unpolarized sea quark distribution functions, as measured by E866 [34], can only be explained by strong non-pQCD contributions. At the same time, this measurement is also able to access the sign change of the Sivers function, if the effect due to TMD evolution on the asymmetries is in the order of a factor of 5 reduction. Figure 2-12 shows the projected uncertainties for transverse single-spin asymmetries of $W^{\pm}$ and $Z^0$ bosons as a function of rapidity and $p_T$ for a delivered integrated luminosity of 400 (900) pb$^{-1}$ and an average beam polarization of 55%. The 400 (900) pb$^{-1}$ corresponds to a RHIC run of 7 (14) weeks, utilizing the concept of a dynamic $\beta^*$ squeeze through the duration of a RHIC fill. The dynamic $\beta^*$ squeeze provides a factor of 2 increase of the luminosity in a fill, compared to run-2013, as the luminosity profile through the fill is kept flat. Such a run is planned for 2016.

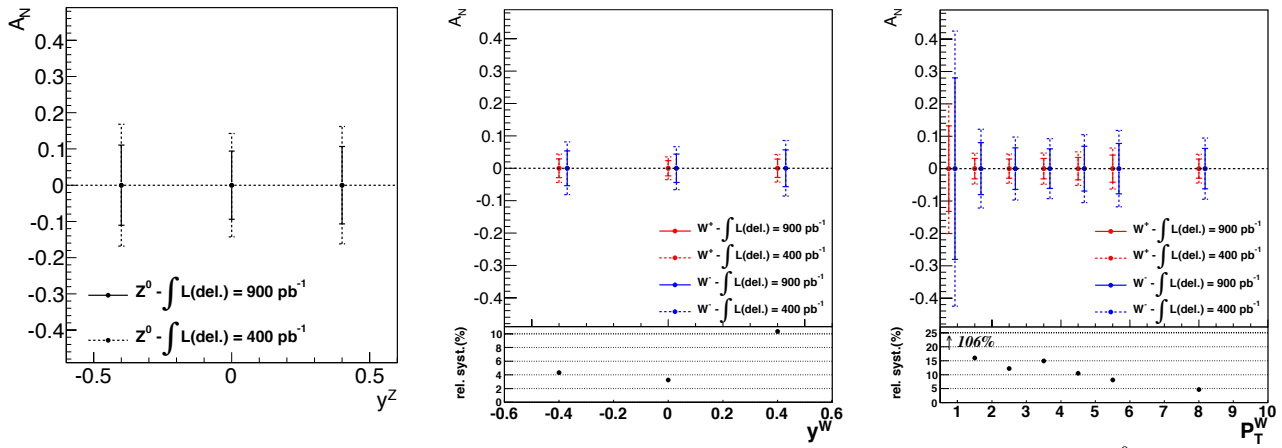


Figure 2-12: The projected uncertainties for transverse single-spin asymmetries of $W^{\pm}$ and $Z^0$ Bosons as a function of rapidity and $p_T$ for a delivered integrated luminosity of 400 (900) pb$^{-1}$ and an average beam polarization of 55%.

The ultimate test for the TMD evolution would be to measure $A_N$ for $W^{\pm}$, $Z^0$ boson and DY production. To obtain a significant measurement of $A_N$ for DY production, the DY leptons need to be detected between rapidities 2 and 4 for a lepton pair mass of 4 GeV and bigger. This is a highly non-trivial measurement, as backgrounds mainly due to QCD 2→2 processes need to be suppressed by a factor of ~$10^6$. STAR has proposed to make a proof-of-concept measurement of $A_N$ for DY during RHIC run-16, using the FMS, preshower and a post-shower. This measurement is anticipated to yield an important benchmark for simulations. The proposed FCS and FTS will provide the needed background suppression to reach a signal to background level of 0.5 to 100 as a function of the DY di-lepton mass. This would allow for a measurement with $\delta A_N$ of 0.02 in 4 bins in rapidity for $2 < \eta < 4$. The COMPASS experiment at CERN is pursuing this sign change using a pion beam in the years 2015 and 2016.

As described above, for a complete picture of the nucleon spin structure at leading twist one must consider not only unpolarized and helicity distributions, but also those involving transverse polarization, such as the transversity distribution, $h_1(x)$ [35, 36, 37]. The transversity distribution can be interpreted as the net transverse polarization of quarks within a transversely polarized proton [36]. Transversity is difficult to access due to its chiral-odd nature, requiring the coupling of the distribution to another chiral-odd distribution. Recently, semi-inclusive deep inelastic scattering (SIDIS) experiments have successfully probed transversity through two channels: the asymmetric distributions of single pions coupling transversity to the transverse-momentum-dependent (TMD) Collins fragmentation function [38]; and asymmetric distributions of dihadrons, coupling transversity to the "interference fragmentation function" (IFF) [39] in the framework of collinear factorization. Taking advantage of universality and robust proofs of TMD factorization for SIDIS, the recent results [40, 41, 42, 43] have been combined with $e^+e^-$ measurements [44, 45] isolating convolutions of Collins and IFFs for the first global analyses to extract simultaneously the transversity distribution and polarized fragmentation functions [46, 47]. In spite of this wealth of data, the kinematic reach of existing SIDIS experiments, where the range of Bjorken-$x$ values don't reach beyond $x \lesssim 0.3$, limits the current extractions of transversity.

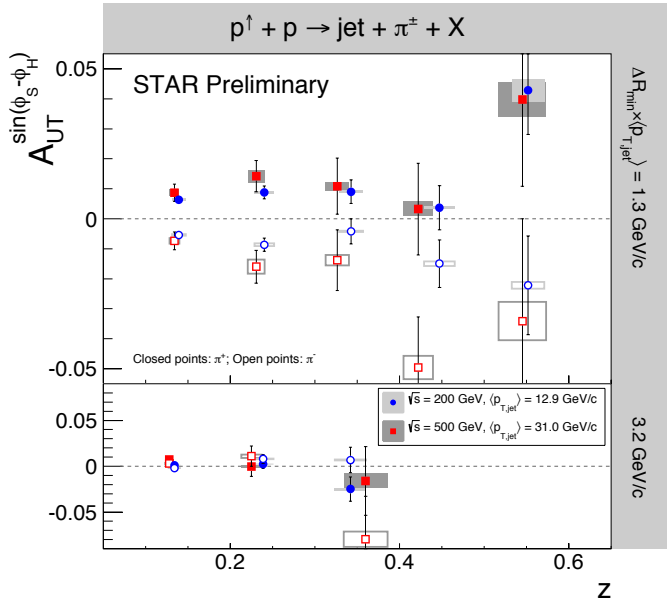


Figure 2-13: $A_{UT}^{\sin(\phi_S-\phi_h)}$ vs. $z$ for charged pions in jets at $0 < \eta < 1$ from p+p collisions at $\sqrt{s}$ = 200 GeV and 500 GeV by STAR. The $p_{T,jet}$ ranges have been chosen to

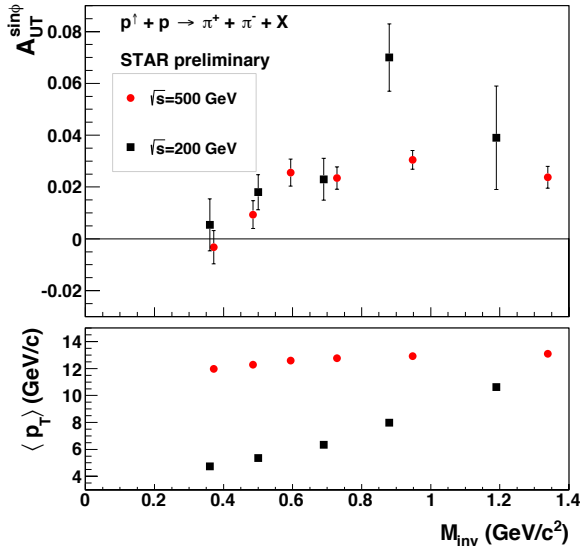


Figure 2-14: $A_{UT}^{sin\phi}$ as a function of $M_{\pi+\pi-}$ (upper panel) and corresponding $p_{T_{\pi+\pi-}}$ (lower panel). A clear enhancement of the signal around

sample the same parton $x$ values for both beam energies. The angular cuts, characterized by the minimum distance of the charged pion from the jet thrust axis, have been chosen to sample the same $j_T$ values ($j_T \sim z \times \Delta R \times p_{T,jet}$). These data show for the first time a non-zero asymmetry in p+p collisions sensitive to transversity × Collins FF.

the ρ-mass region is observed both at √s=200 GeV and 500 GeV by STAR for $-1 < \eta < 1$. These data show for the first time a non-zero asymmetry in p+p collisions sensitive to transversity × IFF.

Figure 2-13 and Figure 2-14 show the first observations of nonzero Collins [48] and dihadron asymmetries [49] in $p$+$p$ collisions at $\sqrt{s}$ = 200 and 500 GeV by STAR. These results are from transversely polarized data taken in 2006, 2011, and 2012, and demonstrate that transversity is accessible in polarized proton collisions at RHIC. STAR finds that the azimuthal asymmetry of pions in polarized jet production depends strongly on $j_T$, the momentum of the pion transverse to the jet thrust axis. The upper panel of Figure 2-13 shows that large asymmetries are found when a wide range of $j_T$ values ($j_T \sim z \times \Delta R \times p_{T,jet}$) are accepted, whereas the lower panel shows that much smaller asymmetries are found when the measurement is restricted to larger values of $j_T$. In both cases, the 200 and 500 GeV measurements are consistent. A comparison of the transversity signals extracted from the Collins effect and IFF measurements will explore questions about universality and factorization breaking, while comparisons of measurements at 200 and 500 GeV will provide experimental constraints on evolution effects. Probing transversity in p+p collisions also provides broader access to the various quark flavors than is available in SIDIS.

Both the Collins and dihadron asymmetries depend directly on the partonic spin transfer parameter $\hat{a}_{TT}$, which approaches unity as one moves toward forward scattering in the partonic center of mass, where $\cos\theta^* \to 1$. Furthermore, transversity remains quite poorly constrained for $x > 0.3$. Extending the measurements of transversity to the high-$x$ region provides access to the tensor charge $\int_0^1 (\delta q^a(x) - \delta \bar{q}^a(x)) dx = \delta q^a$ [50] a quantity essential to understand the nucleon structure at leading twist and calculable in lattice calculations.

The high-$x$ region is accessible with precision only with forward instrumentation, such as the FCS and FTS.The planned STAR upgrades for the second half of this decade include expansion of the TPC tracking capability by about one half of a unit of pseudorapidity as well as charged-particle tracking capability and hadronic calorimetry with the FCS and FTS. Tracking upgrades are critically necessary for Collins and dihadron measurements that require robust charge-sign discrimination. Simulated capabilities with the FCS and FTS are discussed further in section 3.3.

## 2.3 Probing Gluon Dense Cold Nuclear Matter

STAR's quest to understand QCD processes in Cold Nuclear Matter (CNM) centers on the following fundamental questions:

- *What are the dynamics of partons at very small and very large momentum fraction (x) in nuclei, and at high gluon density. What are the nonlinear evolution effects (i.e. parton saturation)?*
- *What are the pQCD mechanisms that cause energy loss of partons in CNM, and is this intimately related to transverse momentum broadening?*
- *What are the detailed hadronization mechanisms and time scales and how are they modified in the nuclear environment?*

Various aspects of these questions are being pursued by experiments and facilities around the world. Deep inelastic scattering on nuclei addresses many of these questions with results from HERMES at DESY [51], CLAS at JLab [52], and in the future at the JLab 12 GeV upgrade and eventually an Electron-Ion Collider [53]. This program is complemented with hadron-nucleus reactions in fixed target p+A experiments at Fermilab (E772, E886, and soon E906) [54] and at the CERN-SPS. The combination of RHIC p+Au and LHC p+Pb data provides an unprecedented large lever-arm in center-of-mass energy and makes a beam-energy scan at RHIC, modulo surprising discoveries, a low priority for upcoming p+A runs. The unique ability of RHIC to run different beam species on the other hand, will be one of the priorities in p+A runs at the end of the decade and, likewise, the unique RHIC capability to probe the nucleus with polarized proton beams may yield compelling new insights, in particular if the initial RHIC polarized p+A run-15 will yield one or more surprises.

### 2.3.1 Physics of high Gluon Densities and small-*x* in Nuclei

The main emphasis of the 2015 and later p+A runs is to determine the initial conditions of the heavy ion nucleus before collision. Our current understanding of nuclear parton distribution functions (nPDFs) is still very limited. Figure 2-15 shows a summary of some of the most recent nPDFs. The central values and their uncertainties for up-valence quarks, up-sea quarks and gluons are shown [55]. The yellow bands indicate regions in Bjorken-*x* where the fits are not constrained by data. This plot shows clearly that high precision data over a wide *x*-$Q^2$ range are needed. Such data are needed for different nuclei as the *A*-dependence of nPDFs cannot be predicted from first principles in pQCD.

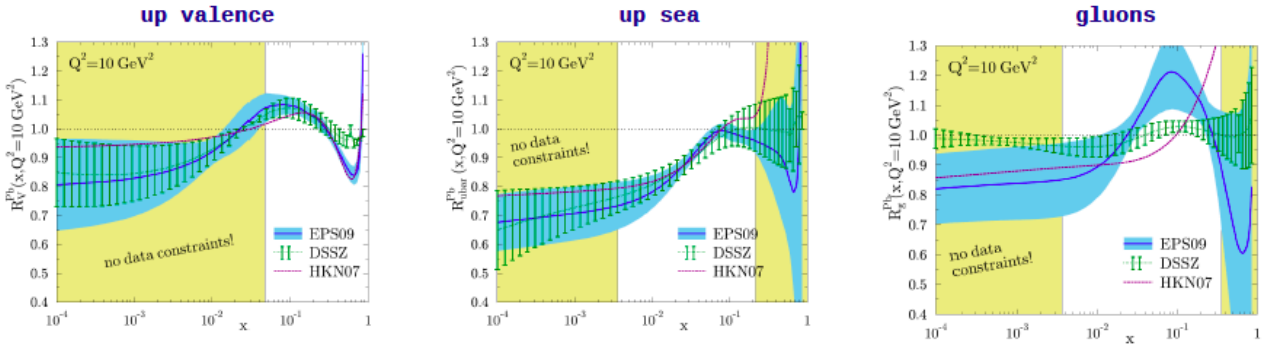


Figure 2-15: A summary of some of the most recent nPDFs. The central values and their uncertainties for up valence, sea quarks and gluons are shown. The yellow bands indicate regions in *x* where the fits are not constrained by data.

It is worth noting that the uncertainties in $R_{\text{gluon}}$ for heavy nuclei are strongly $Q^2$ dependent, with $Q^2$ in hadron-hadron interactions being the square of the transverse momentum ($p_T^2$) of the produced jet or particle (see Figure 2-16).

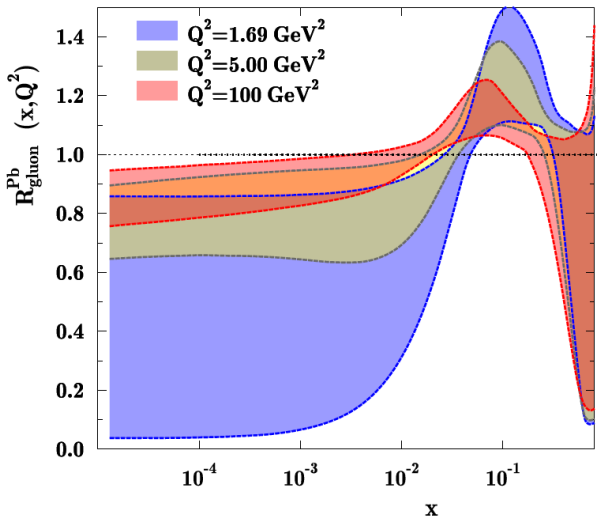


Figure 2-16: $R_{gluon}$ for Pb from EPS-09 for different $Q^2$ values.

In the frame where the nucleus is relativistic, its wave function consists of densely packed quarks and gluons, which constantly split and merge with each other. At high enough energies the density of the gluons is so high that the saturation regime is reached, characterized by strong gluon fields and scattering cross-sections close to the unitarity bound. The saturated wave function is often referred to as the Color Glass Condensate (CGC) and is reviewed in detail in [56]. Current measurements at RHIC strongly suggest that the suppression of single hadrons [57,58] and back-to-back dihadron correlations [59] in d+Au collisions observed at forward rapidities at RHIC [60] can be interpreted as hints for the onset of saturation effects. This would go beyond the modification of nPDFs predicted by pQCD fits to the current world data. The interpretation that the onset of saturation effects has been seen is not unique, however, for two main reasons.

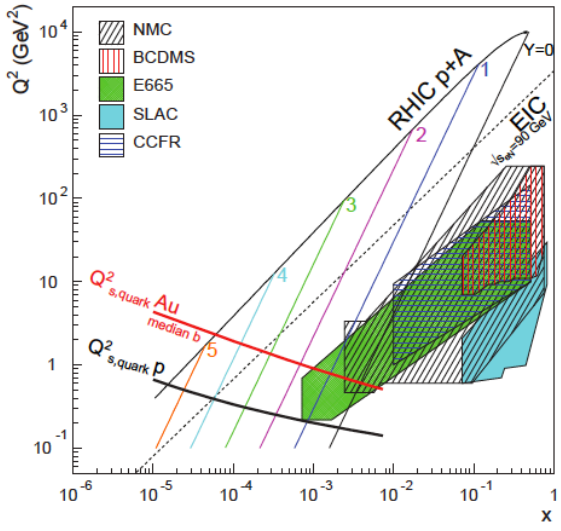


Figure 2-17: The kinematic coverage in the $x$-$Q^2$ plane for p+A collisions at RHIC, along with previous $e$+A measurements, the kinematic reach of an electron-ion collider (EIC), and estimates for the saturation scale $Q_s$ in Au nuclei and protons. Lines are illustrative of the range in $x$ and $Q^2$ covered with hadrons at various rapidities.

Firstly, as shown in Figure 2-17, for the kinematic reach of RHIC energies the saturation scale is moderate, on the order of a few GeV$^2$. Therefore, measurements sensitive to the saturation scale are by necessity limited to semi-hard processes, and effects due to kinematic limits must be fully addressed.

Secondly, and more importantly, in measurements to date in d(p)+A collisions both the entrance and exit channels have components that interact strongly, leading to severe complications

in the theoretical treatment. In d(p)+A collisions, these complications can be ameliorated by removing the strong interaction from the final state, using photons $W^{+/-}$, $Z^0$ and Drell-Yan electrons. Beyond this, the possibility of using polarized protons at RHIC to probe saturation phenomena is just beginning to be explored [61,62], utilizing the large transverse single-spin asymmetries observed in p+p collisions at forward rapidity (which do not require a polarized ion beam) to explore the onset of saturation.

The polarized p+Au in 2015 will be a first step. Its luminosity will allow STAR to make a first systematic study involving rare processes requiring high luminosity. In the text below, a list of the key measurements for Run-15 are given. No *systematic* scan in beam species is proposed for run-15, even though a very modest data sample may be obtained with an additional nucleus beam (likely Al). The understanding of the initial partonic structure of nuclei would greatly benefit from a systematic scan in beam species in later years with the proposed FCS and FTS.

1. Dihadron correlations are still the golden channel at RHIC to observe saturation. The away-side peak in the dihadron correlations represents the back-to-back contribution to the coincidence signal as function of the azimuthal angle difference between the two hadrons in a p+A collision. The correlations are predicted to be diminished with decreasing target nucleus size from p+p to p(d)+Au if saturation sets in. A recorded luminosity of 300 $nb^{-1}$ in Run-15 would give the unique opportunity to vary the trigger and associated particle $p_T$ from low to high values and thus crossing the boundary between saturated and non-saturated regimes as shown in Figure 2-17 and reinstate the correlations for central p+A collisions for forward-forward $\pi^0$'s.

2. Single transverse spin asymmetry in polarized proton-nucleus collisions: As a result of exciting recent theoretical developments, the scattering of a polarized proton on an unpolarized nuclear target appears to have the potential to extend and deepen our understanding of QCD. The nuclear effects on $A_N$ may shed important light on the strong interaction dynamics in nuclear collisions. While the theoretical approaches based on CGC physics predict that hadronic $A_N$ should decrease with increasing size of the nuclear target [63,64,65], some approaches based on pQCD factorization predict that $A_N$ would stay approximately the same for all nuclear targets [66]. Figure 2-18 shows the projected statistical uncertainties for the ratio $A_N$ measured in transversely polarized p+p and p+Au during run-15, which will be sufficient to measure the first transverse spin observables in p+A. The nuclear dependence, however, must be measured in the p+A run at the end of the decade.

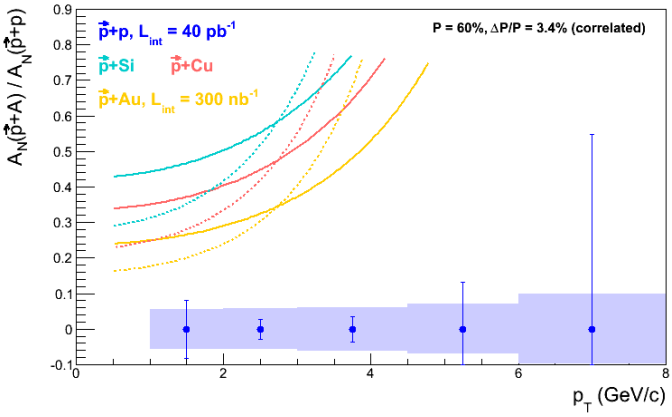


Figure 2-18: The projected statistical and systematic uncertainties for the ratio of $A_N^{pA}/A_N^{pp}$ measured for $\pi^0$'s in the STAR FMS for the requested transverse p+p and p+A running for Run-15. The colored curves follow Eq. 17 in Ref. [51] assuming $Q_s^p$ = 1 GeV (solid) and $Q_s^p$ = 0.5 GeV (dotted) with $Q_s^A = A^{1/3}\, Q_s^p$.

3. $R_{pA}$ for direct photons in the rapidity range $3<\eta<4$:
Direct photons are one of the key channels to separate strong interactions in the entrance and exit channels in d(p)+A collisions, because they have no strong interaction in the final state. The projected uncertainties are small enough to provide a constraint on $R_{gluon}$ at a $Q^2$ between 9 and 40 GeV$^2$ (see Figure 2-16).

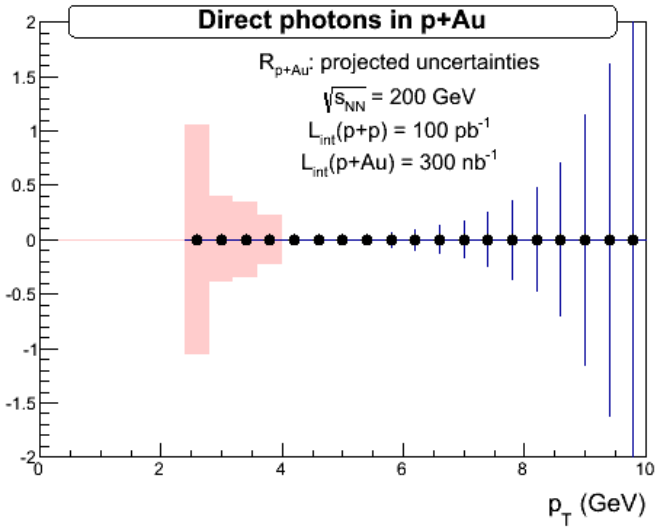


Figure 2-19: $R_{pA}$ for direct photons measured with the FMS and its preshower in the rapidity range $3<\eta<4$. including detector performance and cuts.. The statistical uncertainties are based on recorded luminosities of 100 pb$^{-1}$ for p+p and 300 nb$^{-1}$ for p+Au. The systematic uncertainties are due to the remaining backgrounds..

4. $J/\psi$-production in ultra-peripheral collisions (UPCs) and subsequent leptonic decay provides access to the spatial gluon distribution by measuring the distribution of $d\sigma/dt$. As follows from the optical analogy, the Fourier-transform of the square root of this distribution is the source distribution of the object probed. To study the gluon distribution in the gold nucleus, events need to be tagged where the photon is emitted from the proton. To study STARs capabilities for such a measurement, Monte Carlo simulations events with the Sartre event generator [67,68] have been performed. Sartre is a p+A ($e$+A) event generator specialized for diffractive exclusive vector meson production based on the bSat dipole model [69] and its linearization, the bNonSat model [70]. Figure 2-20 (left) shows the probed $x$-$Q^2$ plane for events, where the "UPC-photon" is emitted by the proton-beam ("p-shine") in UPCs. Figure 2-20 (middle) shows the rapidity distribution for the $J/\psi$-meson for events the "UPC-photon" is emitted by the proton-beam and for events where the photon is emitted by the Au-beam ("Au-shine") after the following cuts have been applied to enhance the p-shine process:
   - no hit in the ZDC to veto the Au-breakup to ensure coherent scattering.
   - detecting the scattered proton in the Roman Pots (RPs) ($-0.016 > -t > -0.2$ GeV$^2$)
   - both $J/\psi$ decay leptons are in $-1 < \eta < 4$
   - cut on the $p_T^2$ of the scattered Au, calculated as the $p_T^2$ of the vector sum of the proton measured in the RPs and the $J/\psi$ to be larger than 0.02 GeV$^2$.

   The background from the Au-shine case is expected to be suppressed with these selections as seen in Figure 2-20 (right). With an integrated delivered luminosity of 2.5 pb$^{-1}$ ~7k $J/\psi$-mesons survive the cuts in the p-shine case. This statistics will allow the measurement of $d\sigma/dt$ for coherently produced $J/\psi$-mesons. This distribution can be further used to obtain information about the gluon distribution in impact parameter space $g(x,Q^2,b)$ through a Fourier transform [71]. For the 2015 p+A run it will only be possible to measure the $J/\psi$-meson rapidity

distribution due to the limited luminosity. The *A*-dependence will require a systematic scan in beam species as is proposed with the FCS and FTS.

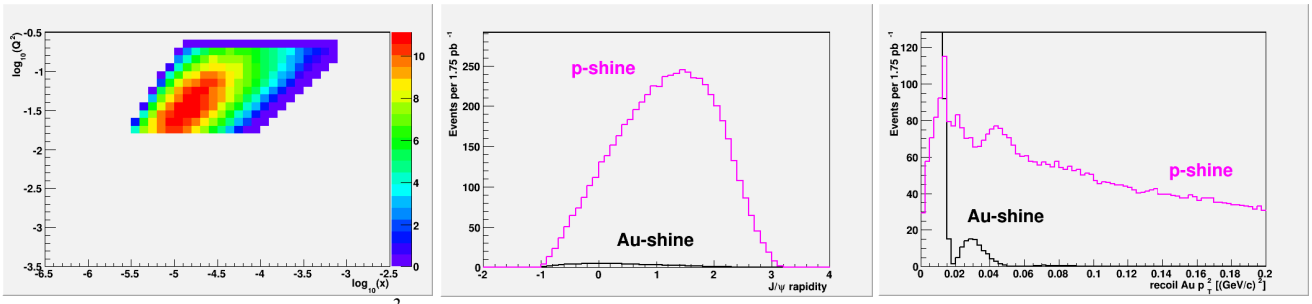


Figure 2-20: (left) The probed $x$-$Q^2$ plane for events for p-shine events. (middle) Rapidity distribution for the $J/\psi$-meson for p-shine and Au-shine events after applying all cuts listed. (right) $p_T^2$ of the scattered Au, calculated as the $p_T^2$ of the vector sum of the proton measured in the RPs and the measured $J/\psi$.

In the following text, we describe measurements that can only be done with proposed FCS and FTS.

As shown above, hard probes in p+A(d+A) collisions at RHIC can, with sufficient luminosity, provide us with new constraints on the nPDFs, especially at scales where the DGLAP evolution is expected still to be applicable, i.e., at $Q > Q_s$. Given the kinematic constraints at RHIC, very forward hadron production measurements (low-$x$) are not well suited to study leading-twist shadowing since the $Q^2$ values are substantially too low. Typically nPDFs are calculated at most down to $Q^2$ ~1.69 GeV$^2$. Of special importance at RHIC will be measurements of correlated charm in p+A collisions at mid- or slightly forward rapidities or gamma-jet correlation measurements at forward rapidities (see section 2.3.2), which will help to pin down the nuclear gluon distributions, while Drell-Yan pairs are expected to set further constraints on the nuclear effects for the sea quark distributions. The Drell-Yan process, $q\bar{q} \rightarrow \gamma^* \rightarrow l^- l^+$, plays a special role among interactions with hadron beams. In contrast to hadronic final states, in Drell-Yan scattering the values of $x_1$, $x_2$, and $Q^2(=M^2)$ can be reconstructed on an event-by-event basis. In addition, factorization has been proven, rather than just assumed, for Drell-Yan di-lepton production. As such, for many years Drell-Yan cross-sections have played a key role in constraining sea quark distributions in nucleon and nuclear PDF fits. (For example, see the discussions in [72,73].)

When measured in the forward direction, Drell-Yan di-lepton production in p+A collisions at RHIC can provide access to sea quark distributions in the nucleus at $x < 0.001$, as is illustrated in Figure 2-21. This is nearly an order of magnitude lower in $x$ than the current nuclear data from deep-inelastic scattering experiments, and over an order of magnitude lower in $x$ than the Drell-Yan data that currently provide five of the primary inputs for EPS09. Furthermore, measurements of the Drell-Yan nuclear dependence at RHIC can also provide significant constraints on the nuclear gluon distribution at very low $x$ via evolution [72]. As such, Drell-Yan measurements at RHIC will provide essentially model-independent information about the nuclear modifications of the gluon distribution well into the $x$ regime where the $\pi^0$-$\pi^0$ correlation measurements indicate gluon saturation may be important. It is noted that forward $J/\psi$ production will be measured concurrently with Drell-Yan scattering. $J/\psi$ production in these kinematics is dominated by $gg$ fusion, so this will provide complementary information about the gluon density at very low $x$.

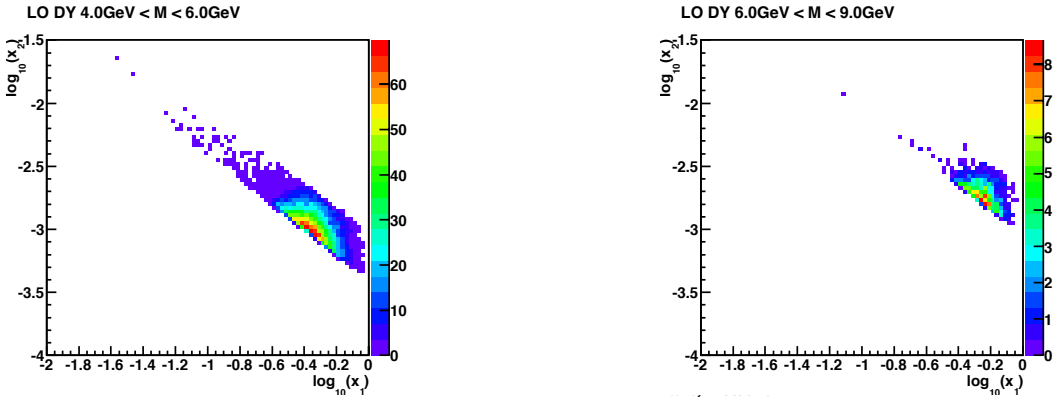


Figure 2-21: The $x_1$-$x_2$ distribution for DY production for 2 bins of the lepton pair mass at $\sqrt{s}$ =200 GeV with the leptons being in the rapidity range $2.5 < \eta < 4.0$.

### 2.3.2 Direct Photon plus Jet

The analysis of the angular dependence of two-particle correlations in hadronic collisions has proven to be an essential tool for testing the underlying QCD dynamics [74]. In forward-forward correlations facing the p(d) beam direction one selects a large-$x$ parton in the p(d) interacting with a low-$x$ parton in the nucleus. For $x < 0.01$ the low-$x$ parton will be back-scattered in the direction of the large-$x$ parton. Due to the abundance of gluons at small $x$, the backwards-scattered partons are predominantly gluons, while the large-$x$ partons from the p(d) are predominantly quarks.

Direct photon plus jet (direct γ+jet) events, predominantly produced through the gluon Compton scattering process, $g+q \rightarrow \gamma+q$, are sensitive to the gluon densities of the nucleon and nuclei in p+p and p+A collisions. Through measurements of the longitudinal double-spin asymmetry in polarized p+p collisions and azimuthal correlations in p+A collisions for direct γ+jet production, one can study the gluon helicity density and gluon saturation phenomena at small $x$. Unlike dijet production that is governed by both the Weizsäcker-Williams and dipole gluon densities, direct γ+jet production only accesses the dipole gluon density, which is better understood theoretically [75]. On the other hand, direct γ+jet production is experimentally more challenging due to its small cross-section and a large background contribution from dijet events in which photons from fragmentation or hadron decay could be misidentified as direct photons. We have studied the feasibility to perform direct γ+jet measurements with the upgraded STAR detector in polarized p+p collisions at $\sqrt{s}$=500 GeV and unpolarized p+p and p+Au collisions at $\sqrt{s_{NN}}$=200 GeV. PYTHIA-8.189 [76] is used to produce direct γ+jet and dijet events. In order to suppress dijet background, the leading photon and jet are required to be balanced in transverse momentum, $\left|\phi^{\gamma} - \phi^{jet}\right| > 2\pi/3$ and $0.5 < p_T^{\gamma}/p_T^{jet} < 2$. Both the photon and jet have to be in the forward acceptance $2.8 < \eta < 3.7$ with $p_T > 4.5$ (3.2) GeV/$c$ in 500 (200) GeV p+p collisions. The photon needs to be isolated from other particle activities by requiring the fraction of electromagnetic energy deposition in the cone of $\Delta R$=0.1 around the photon is more than 95% of that in the cone of $\Delta R$=0.5. Jets are reconstructed by an anti-$k_T$ algorithm with $\Delta R$=0.5. After applying these selection cuts, the signal-to-background ratio is around 3:1 [77]. The expected number of selected direct γ+jet events is around 1.2 million with 500 pb$^{-1}$ delivered luminosity in polarized p+p collisions at $\sqrt{s}$=500 GeV. Such a measurement would constrain the gluon helicity density in $0.0003<x<0.003$ (see Figure 2-22). The expected number of selected direct γ+jet events is around 100k with 500 pb$^{-1}$ (2.5pb$^{-1}$) delivered luminosity in p+p (p+Au) collisions at $\sqrt{s_{NN}}$=200 GeV. We conclude that a

measurement of direct photon-hadron correlation from p+A collisions is feasible (see Figure 2-22), which is sensitive to the gluon density in $0.001<x<0.005$ in the Au nucleus where parton saturation is expected.

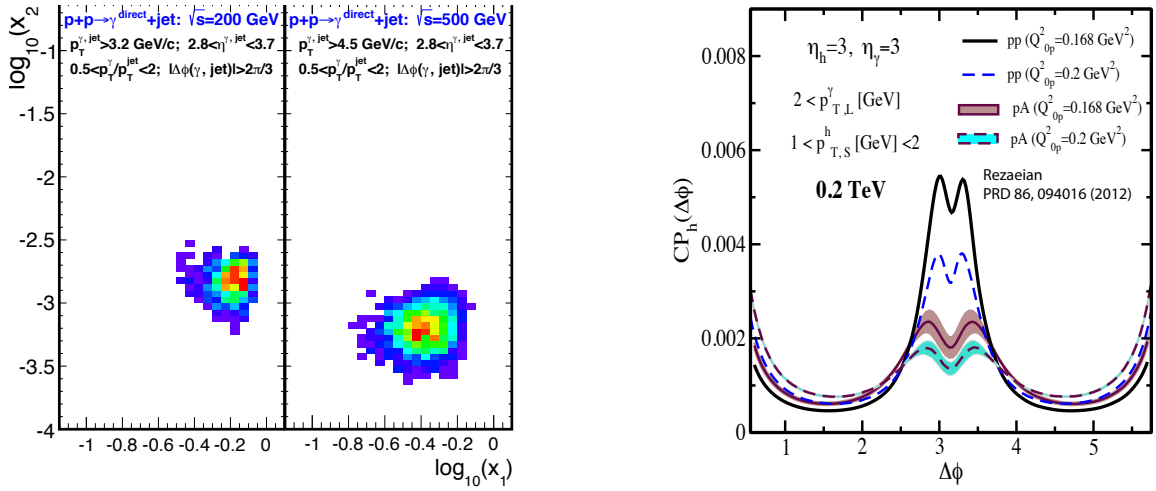


Figure 2-22: Left: Bjorken-$x$ distributions of hard scattering partons in direct γ+jet production after event selections described in the text in p+p collisions at $\sqrt{s}$=200 and 500 GeV, respectively. Right: γ-hadron azimuthal correlation in minimum bias p+p and p+Au collisions at $\sqrt{s_{NN}}$=200 GeV. The curves are obtained with two different initial saturation scale of proton $Q^2_{0p}$=0.168 and 0.2 GeV$^2$ and the corresponding initial saturation scale in the nucleus within $Q^2_{0A}$~3-4$Q^2_{0p}$ (c.f. [75]).

### 2.3.3 Energy Loss in Cold Nuclear Matter

One of primary observables for measuring cold nuclear matter effects is the production of J/$\psi$ in p+A collisions. Since $J/\psi$ are produced in hard collisions, their yields are expected to scale as the nuclear thickness function $T_{AB}$, for collision species A and B, in the absence of nuclear modifications. In p+A collisions, the observed yields can be affected by both modifications to the parton distribution functions (an initial-state effect), which can also include saturation effects at large enough gluon densities, as well as energy loss in the cold nuclear medium (a final-state effect) [78]. At mid to forward rapidity, both of these effects result in a suppression of the $T_{pA}$-scaled yields. At very forward rapidity, the energy loss mechanism is expected to become dominant, making it easier to differentiate between the two effects. Figure 2-56 shows the predicted effect of CNM energy loss on the $R_{pA}$ of $J/\psi$ as a function of rapidity [78, 79], where $R_{pA}$ is the ratio of the $T_{pA}$-scaled particle yields in p+A collisions to the cross-section measured in p+p collisions.

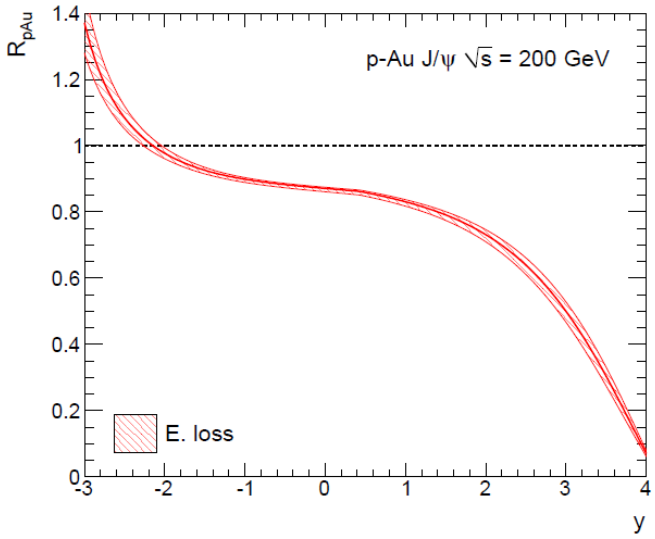


Figure 2-23: Predicted $R_{pA}$ for $J/\psi$ at $\sqrt{(s_{NN})}$=200 GeV as a function of rapidity [78, 79].

PHENIX has measured $R_{dAu}$ for $J/\psi$ at backward to forward rapidity, but the measurement does not extend up to $y > 3$, where the suppression is predicted to be largest. Figure 2-57 (left) shows the PHENIX publication of this measurement in d+Au collisions [80] in the range $-2.2<y<2.2$. The theoretical calculation [104], including both energy loss and modified PDF's, agrees with the data well. At these rapidities, the effect of energy loss is not as strong as at more forward rapidity. The models are able to describe the current data with and without saturation effects and with different values of "q-hat" varying the parton energy loss. More forward measurements have been performed at the LHC, by both the LHCb experiment [81] and the ALICE experiment [82] at a higher collision energy of $\sqrt{s_{NN}}$=5 TeV. Figure 2-57 (right) shows the result from the LHCb experiment compared to theoretical calculations. The $J/\psi$ is measured for $p_T<14$ GeV/$c$ (with mean $p_T$ between 2.5 and 3.0 GeV/$c$). For this measurement at the LHC collision energy, the models including only initial-state effects are not so distinguishable from those containing effects from final-state effects. The measurement for $1.5<y<4.0$ is consistent with LO EPS09 and nDSg [83] (two different parameterizations of the nuclear-modified gluon distribution functions) calculations, NLO EPS09 [84], as well as those calculations including both initial-state effects and final-state energy loss (curves labeled "E. loss") [78].

The result from ALICE [82] is in a similar kinematic range and is consistent with the LHCb result. The same calculation shown for RHIC collision energy in Figure 2-23 [78] is also in Figure 2-24 (right) for LHC collision energy. In this calculation, the suppression is predicted to be larger at forward rapidity at RHIC.

With the planned forward upgrades, STAR will be able to measure $J/\psi$ for $2.5<y<4.0$ through the mass reconstruction of electron-positron pairs. Tracking in the FTS together with the calorimetry of the planned FCS will provide good electron/positron candidates for the invariant mass calculation. The Pre-Shower in the FCS will provide further rejection of photons as well as hadrons.

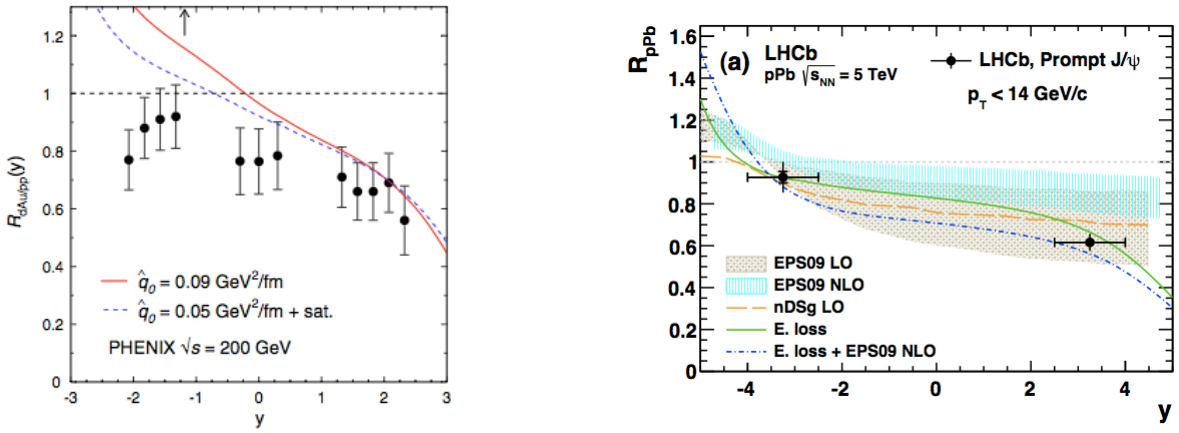


Figure 2-24: (Left) PHENIX measurement of CNM effects of $J/\psi$ production in d+Au collisions relative to p+p collisions for $-2.2<y<2.2$ at $\sqrt{(s_{NN})}$=200 GeV [80] compared to a theoretical calculation [78]. (Right) LHCb measurement of $J/\psi$ production in p+Pb collisions relative to p+p collisions for $1.5<y<4.0$ and $-5.0<y<-2.5$ at $\sqrt{(s_{NN})}$=5 TeV [81] compared with theoretical calculations [78, 83, 84].

### 2.3.4 The Ridge in p+A Collisions

One of the novel discoveries in high-energy heavy-ion collisions is the finite two-particle correlation at small azimuthal opening ($\Delta\phi$) with large pseudo-rapidity separation ($\Delta\eta$). It is generally referred to as the "ridge." It was first discovered in Au+Au collisions at RHIC [85]. It was observed after subtraction of the elliptic flow background and is postulated to be due, at least in part, to high-order anisotropic flows. High-order hydrodynamic flows are more sensitive than elliptic flow to the hydrodynamic properties of the collision medium, such as the shear viscosity to entropy density ratio ($\eta/s$). The longitudinal decorrelation effects complicate the situation and the forward rapidity coverage for correlation measurements is essential for a robust extraction of $\eta/s$.

The long-range ridge has been observed in small systems: p+p [86], p+Pb [87,88] collisions at the LHC (see Figure 2-25), and d+Au [89] collisions at RHIC. In these cases the ridge was observed after subtraction of a uniform background. The resemblance to the heavy-ion ridge raised the interesting possibility of elliptic flow in small-system collisions. The elliptic anisotropy parameter ($v_2$) extracted from the ridge correlations in these small systems is comparable to that from heavy-ion collisions. Furthermore, the $v_2$ parameter has a characteristic mass dependence suggestive of hydrodynamic origin (c.f. Figure 2-26).

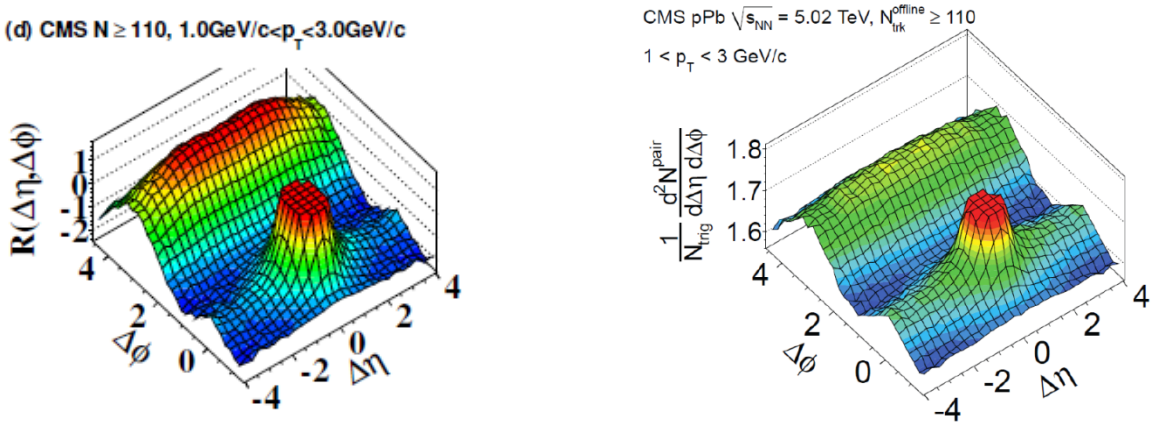


Figure 2-25: Two-p particle correlation in high-multiplicity p+p collisions [86] (left panel) and p+Pb collisions [87] (right panel).

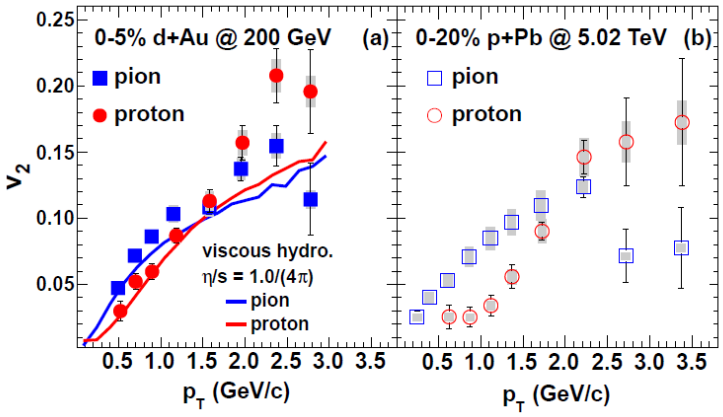


Figure 2-26: Pion and proton elliptic anisotropy parameter $v_2$ as a function of $p_T$ in central d+Au collisions at RHIC [89] (left panel) and central p+Pb collisions at the LHC [88] (right panel).

Hydrodynamic flow is a final-state effect. A large anisotropic flow at moderate to high $p_T$ must be accompanied by strong jet-quenching due to the hot-medium effect in A+A collisions. However, no large jet-quenching effect has been observed in these small systems; measurements of nuclear modification factors are consistent with unity [90]. In fact, the small-system collisions were originally motivated as reference to gauge any possible initial-state effects for jet-quenching measurements in heavy-ion collisions. Measurements of small-system collisions indicate Cronin enhancement and cold nuclear matter effect at moderate $p_T$, but no significant final-state effects. This raises the question whether the ridge correlation may be an initial-state effect.

One possibility is the Color Glass Condensate (CGC) where the two-gluon density is enhanced at small $\Delta\phi$ over wide range of rapidity [91]. There were hints of the CGC from the forward measurements in d+Au collisions; for example, the back-to-back dijet correlation is suppressed at forward rapidities measured by STAR. If gluon saturation happens at forward rapidity at RHIC energy, it might also be observable at mid-rapidity at the LHC. The ALICE measurement of dihadron correlations, while indicating a back-to-back ridge formation, however, shows no evidence of suppression of the back-to-back jet-correlations [90]. While the $x$-ranges probed in the partonic processes at forward rapidities at RHIC and at mid-rapidity at the LHC are similar, differences are expected to exist in the dynamical interplay in particle production at these energies.

The second Fourier coefficient, related to the elliptic anisotropy parameter $v_2$, of the dihadron azimuthal correlations at large $\Delta\eta$ in d+Au collisions measured by STAR shows strong a $\Delta\eta$ dependence (see Figure 2-27). The parameters are approximately equal between high and low forward multiplicity triggered events and between backward (Au-going) and forward (d-going) rapidities. This suggests that the $v_2$ parameter of the correlations between particles is universal, and does not fit naturally into the hydrodynamic picture.

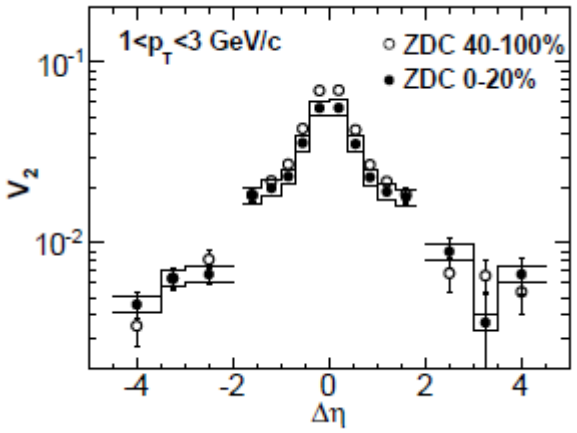


Figure 2-27: The $\Delta\eta$ dependence of the second harmonic Fourier coefficient in low and high ZDC-Au activity d+Au collisions. Error bars are statistical and boxes indicate 10% systematic uncertainties of the high-activity data.

Further analysis of STAR d+Au data showed that yield of the near-side ridge yield is approximately proportional to the away-side correlated yield. This is shown in Figure 2-28. The linear fit to the $\Delta\eta$ <-1 data points, depicted by the dashed line, indicates that the ratio of the near-side ridge to the away-side jet is consistent with a constant. The constancy of this ratio is remarkable given that the away-side jet correlated yield changes by nearly order of magnitude from TPC-TPC correlations (both particles are at mid-rapidity) to TPC-FTPC correlations (one particle is at midrapidity and the other particle is at forward rapidity). At this large $\Delta\eta$, contributions from the near-side jet to the ridge yield should be negligible. However, the proportionality may suggest that the near-side ridge is somehow correlated to jet production. Could it be caused by color connection between the mid-rapidity jet and beam jets?

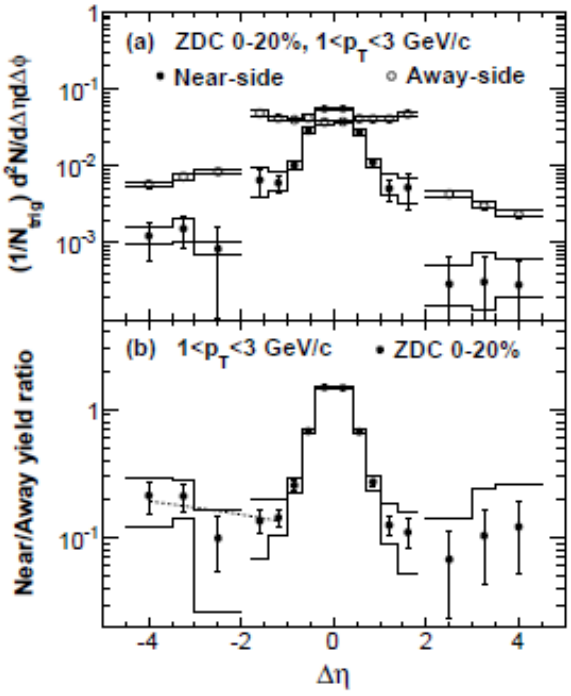


Figure 2-28: The $\Delta\eta$ dependence of (a) the near-side ($|\Delta\phi|<\pi/3$) and away-side ($|\Delta\phi-\pi|<\pi/3$) correlated yields in high ZDC-Au activity d+Au collisions. Error bars are statistical and boxes indicate systematic uncertainties (for $\Delta\eta>2$ in (b) the lower bound falls outside the plot). The dashed curve in (b) is a linear fit to the $\Delta\eta<-1$ data points.

The current d+Au data from STAR have rather low statistics. A significant increase in statistics is desired in order to investigate the d+Au ridge more differentially. The current d+Au data with a large $\Delta\eta$ gap were afforded by the STAR forward time-projection chambers (FTPCs) which have since been decommissioned. The planned FCS covers a pseudo-rapidity range similar to the FTPC's

and could therefore be used in their place. The energy measured by the hadronic calorimeter will be mainly from charged pions, protons and neutrons. Correlations between the calorimeter energy and the mid-rapidity charge particles, with a large $\Delta\eta$ gap, will be ideal to investigate the physics mechanisms of the expected near-side ridge in pA collisions. The discrimination of the different possible physics mechanisms, final-state hydrodynamics or initial-state effects, will further our knowledge of QCD.

## 2.4 Probing Hot and Dense Nuclear Matter

RHIC was built to create and study the properties of Quark-Gluon Plasma [92,93] (QGP), a matter that permeated the universe up until one microsecond after the big bang. Experiments at RHIC were the first to establish the existence of a QGP phase in Au+Au collisions that reached temperatures approximately 250 thousand times hotter than the center of the sun. In another key discovery at RHIC, the hottest matter ever created by humans was also found to be the most perfect fluid known in nature, with a shear viscosity to entropy ratio, $\eta/s$, near the lower bound of a quantum limit [94] established through both string theory calculations and Heisenberg's uncertainty principle. Using heavy-ion collisions to measure the properties of the QGP requires dynamical models that describe the collisions with sufficient accuracy that transport properties like $\eta/s$ can be inferred from measurements of the distributions and correlations of produced particles. Accurate descriptions of the collisions required many advances spurred by the experimental flexibility of the RHIC collider to study different system sizes and collision energies. One prominent example is the realization that because the QGP phase is characterized by such a low $\eta/s$, density fluctuations from the initial state are transferred into the final state and show up as long-range pseudo-rapidity correlations like "the ridge". These correlation functions can also be characterized by their Fourier harmonics $v_n$ that are then compared to multi-phase model calculations [95,96] to extract information about the thermodynamic and transport properties of the QGP phase.

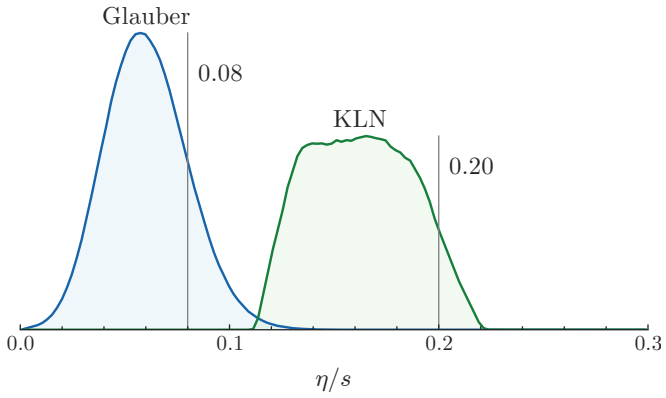


Figure 2-29: Posterior distributions from a Bayesian analysis of heavy ion data. Preferred values for $\eta/s$ change depending on whether a CGC (KLN) or Glauber based initial condition are used [100].

While these multi-phase models have been shown to provide a good description of particle production in heavy ion collisions, several uncertainties remain in them that compromise our ability to improve on the precision of our estimates of $\eta/s$ and other properties of the QGP. The initial conditions are a critical component of the models and provide the input for the low viscosity

hydrodynamic phase. Although recognition of the need to include density fluctuations from the initial state led to an order of magnitude reduction [97,98] in the uncertainties on η/s, our uncertainties in the correct physics of the initial state, whether gluon saturation or Glauber, are still problematic. Two prominent models, fKLN-CGC and MC-Glauber [99], were recently shown to lead to a factor of two discrepancy in the $\eta/s$ inferred within a Bayesian framework through model to data comparisons [100]. To further complicate the picture, while that calculation showed a preference for the MC-Glauber model, measurements of $v_2$ in central U+U collisions have been shown to prefer the CGC based IP-Glasma model over the MC-Glauber model [101,102]. Providing experimental access to the nature of the initial state in heavy ion collisions is therefore important for the successful study of the emergent properties of finite temperature QCD and important insights on the initial state can be garnered from the study of the rapidity evolution of the correlation functions in A+A and p+A collisions.

In addition to uncertainties in the initial state, uncertainties remain in the physics of the hydrodynamic models themselves that need to be addressed [103]. One prominent question is to what extent thermal fluctuations during the expansion phase contribute to the correlations observed in the data? These fluctuations have not been implemented into hydrodynamic models in a rigorous way but early calculations and basic causality considerations indicate that these thermal fluctuations will lead to longitudinal correlations with widths of approximately two units in pseudo-rapidity. These correlations are therefore expected to be at or beyond the edge of the acceptance of the STAR TPC. The correlations induced by thermal fluctuations can again; introduce uncertainty in the extraction of $\eta/s$ from the correlation functions measured in heavy ion collisions [108]. They in-fact mimic viscous effects and can lead to an overestimate of the actual viscosity. The most promising experimental method to estimate their contribution is to measure the pseudo-rapidity dependence of correlation functions.

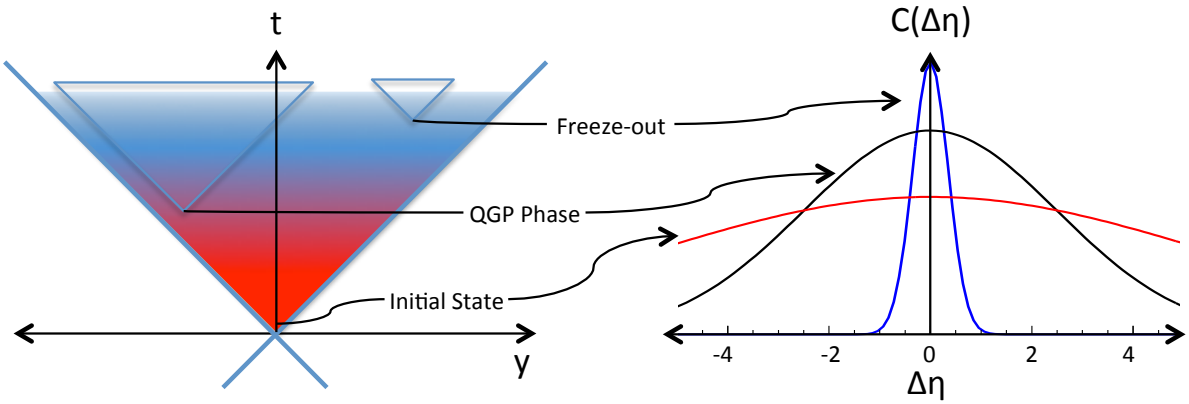


Figure 2-30: An illustration of the rapidity ($y$) and time evolution of a heavy ion collision (left). An illustration of correlations of various widths in $\Delta\eta$ (right). Causality precludes correlations from later stages from growing as wide as those from earlier stages.

Both of these pressing uncertainties can be addressed by extending the longitudinal acceptance of the STAR detector. At RHIC, it is possible to build upgrades that reach near beam rapidity; or even beyond for lower energies (as in the Beam-Energy-Scan program). In addition, past history demonstrates that a wide pseudo-rapidity acceptance provides crucial information about the physics of effects observed at mid-rapidity. Indeed, wider pseudo-rapidity coverage was essential to linking the ridge correlation to fluctuations in the very early phase of the collisions. A study of the details

of that phase will also require this capability. It is a high priority to make these measurements at RHIC because the QGP is expected to have its smallest *η/s* value near the transition region ($T$=$T_c$). RHIC collisions spend relatively more time in that region and are therefore best suited for studying the most perfect liquid known in nature. Indeed, model calculations have found that the average η/s value needed to reproduce measurements at RHIC is smaller than the *η/s* needed for the LHC. Statistical analyses based on modern Bayesian methods [100,104] have shown that data taken from the LHC alone, do not constrain the value of *η/s* at $T_c$ as well as data taken from RHIC alone: simply put, RHIC provides the best constraint on *η/s* at $T_c$. Building on the discovery of the perfect liquid, measurements at RHIC will remain crucial for mapping out the temperature dependence of *η/s* and other transport properties. Fig.2-31 shows the results of a very recent theoretical calculation using event-by-event 3+1 dimensional viscous relativistic hydrodynamic simulations from Ref [148,149]. In this simulation it was shown that a precise measurements of the pseudo-rapidity dependence of the flow harmonics is instrumental in determining the transport properties of QCD matter and the longitudinal fluctuations of the initial state of heavy ion collisions. However, due to large uncertainties and limited acceptance of the currently available measurements, only limited conclusion can be drawn on the temperature dependence of the transport parameters. Our forward upgrade program will focus on reducing the large uncertainty in the pre-existing data of different flow harmonics over a wide range of rapidity allowing more precise determination of the temperature dependence of the transport parameters such as *η/s(T)*.

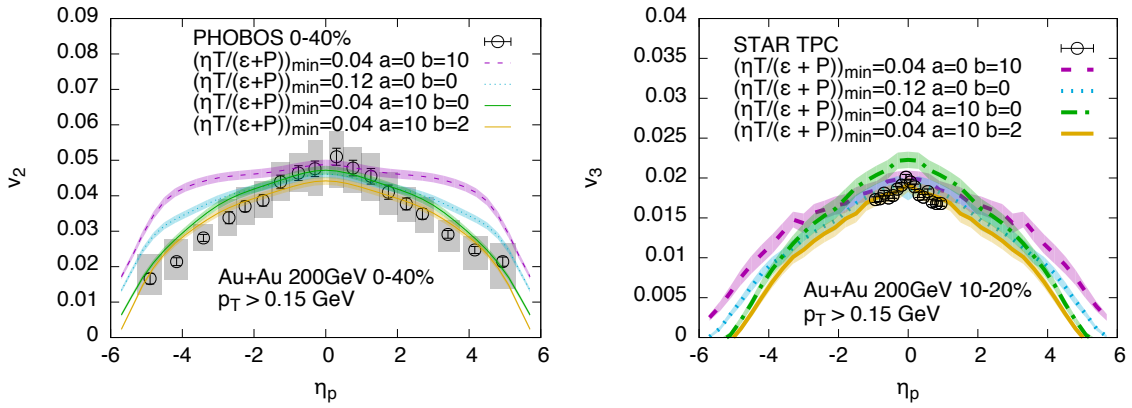


Figure 2-31: Model calculations [148,149] compared to the measurements of the pseudo-rapidity dependence of elliptic and triangular flow of charged particles produced in heavy-ion collisions at RHIC. The comparisons are made to previous PHOBOS and STAR measurements and for hydrodynamic simulation with 3 dimensional initial condition and different parameterization for the temperature dependence of *η/s*. A more precise measurement compared to the pre-existing data will be essential to constrain the *η/s*.

Correlations from flow, in particular their event-by-event fluctuations, have been a crucial tool for understanding the space-time picture of heavy-ion collisions and the properties of the QGP phase. However, event-by-event QGP dynamics in the longitudinal directions remain poorly understood. Such studies are vital to adequately constrain the current suite of sophisticated theoretical frameworks that incorporate not only realistic initial conditions and the interactions of hard processes with the medium, but also 3+1 viscous hydrodynamics coupled to hadronic transport codes. In addition to uncertainties in the initial state, uncertainties remain in the physics of the hydrodynamic models themselves that need to be addressed. Correlations induced by thermal fluctuations or mini-jets can also introduce uncertainty in the value of η/s extracted from correlation functions measured in heavy-ion collisions [108]. By mimicking viscous effects these correlations can lead to an overestimate of the actual viscosity. The most promising experimental method to estimate their contribution is to measure the pseudo-rapidity dependence of correlation functions.

New flow observables, that help further elucidate the space-time picture of the QGP evolution in both the transverse and longitudinal directions, will be enabled by our forward upgrade program. These novel measurements will enhance our understanding of QGP at 200 GeV and provide a crucial step towards completion of the mission of the RHIC heavy-ion program. Active theory and experimental explorations of new measurements in longitudinal correlations have produced several promising tools in probing initial sources, nuclear stopping, longitudinal pressure/flow, and hydrodynamic fluctuations throughout the evolution. Examples of these proposed measurements are: mixed harmonic correlations of reaction planes, torque (twist) of event shape, the Legendre coefficients of the two-particle pseudo-rapidity correlation functions [139–141] and Principal Component Analyses [142, 143]. In combination with similar measurements at the LHC, and the existing large set of published data on the event-averaged flow, they will also provide necessary constraints on the temperature evolution of the QGP properties.

The following table summarizes the physics measurements relevant to the STAR forward upgrade project and what other upgrades (iTPC[105], EPD[106]) in STAR are relevant to those measurements. We emphasize that some of the detectors provides redundant or complementary information for the same measurements. However, each detector has different strengths.

| Physics Measurements<br><br>Detector | Acceptance | Longitudinal Decorrelation | Mixed flow harmonics | Flow phases | Event-shape engineering | Ridge and jet-medium (pA) |
|---|---|---|---|---|---|---|
| Forward Calorimeter (**FCS**) | $-2.5>\eta>-4.2$ $E_T$ (photon, hadrons) | Necessary | One of these detectors necessary, LHC proven success with FCS | Important to have at least one of these two detectors | At least one of these three detectors is necessary. Priority: EPD, FTS, FCS. | Necessary |
| Forward Tracking (**FTS**) | $-2.5>\eta>-4.2$ charged particles | Complementary to FCS | | | | Necessary |
| Event-Plane Detector (**EPD**) | $2<\lvert\eta\rvert<4.5$ w/ phi segment multiplicity | Good to have | Important | Necessary for F/B correlation | | Good to have |
| Inner TPC (**iTPC**) | $\lvert\eta\rvert<1.7$ charged track/PID | Necessary acceptance | Important for extending the eta coverage around midrapidity | | | |

Table 2-4: Physics measurements with the proposed forward upgrades and with other STAR upgrades that are relevant to those measurements.

### 2.4.1 Longitudinal decorrelation of Anisotropic Flow in Heavy-Ion Collisions

Calculations of the number of participating nucleons, Npart, and the associated eccentricity vector, $\varepsilon_n = \varepsilon_n e^{in\Psi_n}$, separately for the forward-going and backward-going nuclei, show that $N_{part}^{F} \neq N_{part}^{B}$ and $\boldsymbol{\varepsilon_n^F \neq \varepsilon_n^B}$ in most events. This suggests that in a single event the entropy production, and the shape of its transverse profile, at early times could exhibit a large forward-backward (FB) asymmetry and twist. These initial fluctuations result in signals that survive the medium's expansion and appear in the final state as a FB asymmetry in the particle multiplicity [$dN/d\eta\ (\eta) \neq dN/d\eta\ (-\eta)$] and vn [$v_n(\eta) \neq v_n(-\eta)$], as well as FB-twist of the observed event plane angles [$\phi_n(\eta) \neq \phi_n(-\eta)$]. Measurements of the η dependence of the multiplicity fluctuations and event plane decorrelations therefore directly probe the initial state and early time dynamics of the QGP. These results will also serve as critical constraints to the full 3+1D event-by-event viscous hydrodynamic models that are currently under development. If these FB fluctuations and decorrelations are

ignored, our understanding of the temperature dependence of η/s will be, at best, incomplete, as initial measurements at LHC suggest these effects are quite significant [144].

Below we illustrate the impact of longitudinal fluctuations on extracting η/s at mid-rapidity and then come to the experimental observables with forward upgrade.

### *Impact of longitudinal fluctuations on extracting η/s at mid-rapidity*

Most recent event-by-event hydrodynamic studies employ either a Glauber or CGC model of parton production for the initial transverse energy density distribution. In the Monte Carlo (MC) Glauber models it is assumed that the initial energy density is proportional to the transverse density of the number of wounded nucleons, or a linear combination of the number of wounded nucleons and binary nucleon-nucleon collisions. The MC models with CGC initial conditions use the Kharzeev-Levin-Nardi (KLN) [107] description of initial gluon production per wounded nucleon pair. These new implementations including fluctuating or bumpy initial energy density distributions via event-by-event simulations affect both the transverse momentum spectra and the azimuthal anisotropic flow compared to event-averaged smooth initial conditions.

Fluctuations in the initial energy density are expected to come from soft interactions of overlapping nucleons and also incoherent semi-hard parton scatterings in each binary nucleon collision. The fluctuations have been studied with a hydrodynamic model [108], assuming that mini-jets from semi-hard parton scatterings are assumed to be locally thermalized and give rise to non-vanishing initial local flow velocities. Fluctuations in the initial flow velocities lead to harder transverse momentum spectra of final hadrons due to non-vanishing initial radial flow velocities. In addition, initial fluctuations in rapidity distributions lead to expanding hot spots in the longitudinal direction and are shown to cause a sizable reduction of final hadron elliptic flow at large transverse momenta.

To investigate the effect of longitudinal fluctuations on hadron spectra the authors [108] compare their event-by-event hydro calculations, using the initial conditions from full AMPT results, with that using a tube-like smooth initial longitudinal distribution. In the tube-like initial condition, the initial energy density and transverse flow velocity from AMPT results in the central rapidity region are used and these transverse fluctuations are assumed to persist along the longitudinal direction with an envelope function in rapidity. Alternatively, the elliptic flow from a one-shot AMPT initial condition is the average of many AMPT events each rotated by a random angle to a common participant plane ("one-shot" initial condition). Shown in Figure 2-32 are the elliptic flow values of identified charged hadrons in semi-central (30%–40%) Au+Au collisions at the RHIC energy $\sqrt{s_{NN}}$=200 GeV with the full AMPT initial conditions (solid lines) compared to the initial conditions with a tube-like structure in the longitudinal direction (dot-dashed lines) and the one-shot AMPT with tube-like longitudinal distribution initial conditions (dashed lines). The event-by-event fluctuations in the tube-like AMPT initial conditions significantly reduce elliptic flow of the final hadrons with respect to the event planes compared to the one-shot AMPT initial conditions. The full AMPT initial conditions have hot spots in the longitudinal direction. The expansion of such longitudinal hot spots will dissipate more transverse energy into the longitudinal direction. This in turn decreases noticeably the value of the elliptic flow at large $p_T$ compared to the results from tube-like event-by-event AMPT initial conditions. Since anisotropic flow, at large $p_T$ in particular, is used to extract transport coefficients (such as shear viscosity) from comparisons between experimental data and viscous hydrodynamics, the inclusion of fluctuations in the initial rapidity distribution in the hydrodynamic calculations is necessary for more quantitative studies.

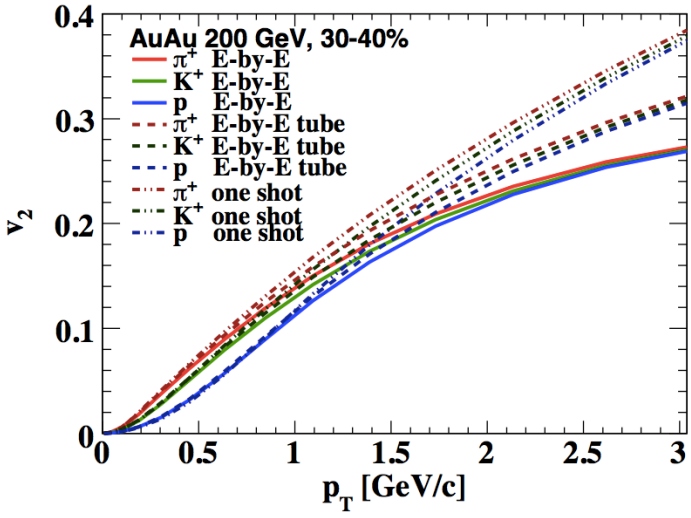


Figure 2-32: Ideal Hydrodynamic simulation of the elliptic flow measured at mid-rapidity as a function of $p_T$ under different conditions of longitudinal fluctuations.

### *Experimental Measurements*

The high granularity and large acceptance forward detectors, FCS and FTS, will enable STAR to perform a detailed investigation of the event-by-event flow fluctuations in the longitudinal direction. Recent detailed calculation via AMPT and event-by-event hydrodynamic model [108,109] suggest that it holds great potential to uniquely probe the early time dynamics of heavy ion collisions that so far defies explanation. As explained above, the strong decorrelation of the event plane angle and flow magnitude are naturally related to the independent fluctuation of the *N*part in the two colliding nuclei. The observed magnitude depends on the particle production mechanism, initial flow, and the thermalization mechanism. They are also naturally expected to have very strong dependences on the beam energy.

Figure 2-33 shows measurements of the event plane decorrelations and comparison to the hydrodynamic simulation from CMS [145]. In comparison to the LHC, RHIC has a more compressed rapidity window, this is predicted to result in stronger FB signals. Based on the LHC results it is therefore critical to measure and interpret such signals, and their effects on the medium's evolution, at RHIC. Our forward upgrade program will provide a unique ability to accurately determine η/s at it's minimum near the phase boundary. However, the present RHIC results have limited sensitivity due to low statistics and large systematical uncertainty from detector non-uniformity in the forward rapidity. These comparisons show the importance of datasets with high statistics and detector uniformity at forward rapidity with fine granularity.

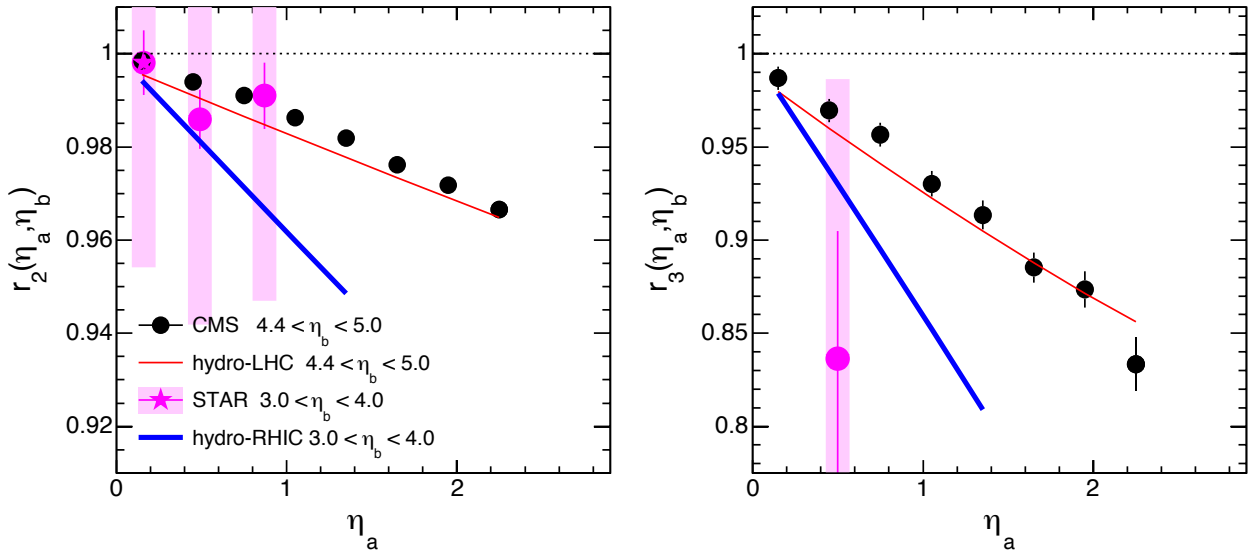


Figure 2-33: The comparison of the decorrelation of $v_2$ (left panel) and $v_3$ (right panel) between $\eta_a$ and $\eta_{-a}$ with reference detector chosen at certain $\eta_b$ range between CMS data (circles), STAR data (star), and hydrodynamic model calculations for LHC (thin lines) and RHIC (thick lines) energies. The correlator $r_n$ is calculated from the two-particle flow coefficients $V_{n\Delta}$ as: $r_n(\eta_a, \eta_b)=V_{n\Delta}(-\eta_a, \eta_b) / V_{n\Delta}(\eta_a, \eta_b)$. The model describes the CMS data and predicts a much stronger effect at RHIC even in the smaller $\eta_a$ range. The large uncertainty of the STAR measurement is due to limitations in the available statistics and detector performance.

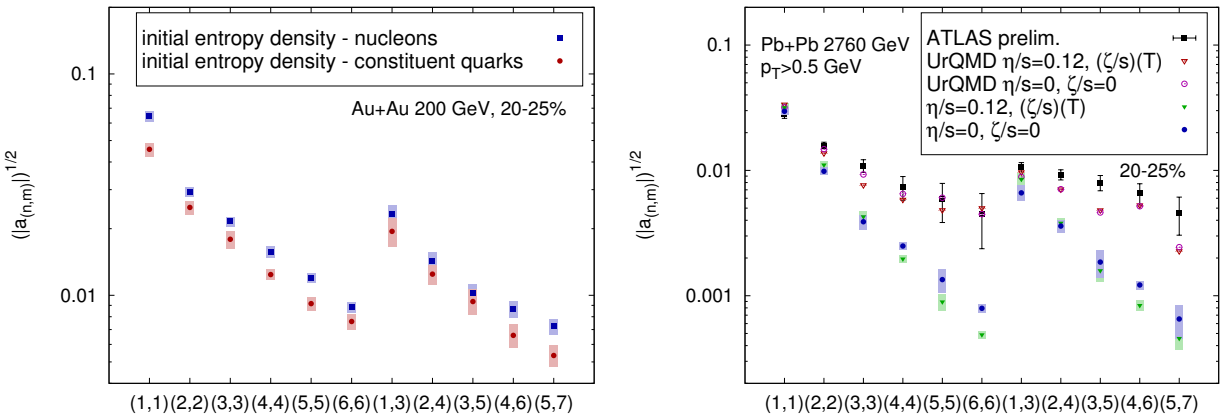


Fig-33a : Two-particle pseudorapidity correlations a_{n,m} expanded in the basis of Legendre polynomials[150] for different combinations of orders n & m. Model calculations [148,149] are done with 3 + 1 dimensional viscous hydrodynamic simulation for RHIC(left panel) and LHC(right panel). The model calculations shown in the right panel are compared to the LHC data.

A new observable has been recently introduced by the ATLAS collaboration [150] to characterize the structure of the longitudinal fluctuation which is referred a_{n,m}. It is defined in terms of the decomposition of the two-particle pseudo rapidity correlations in the basis of Legendre polynomials. Measurement of a_{n,m} done at LHC has been compared to a recent 3 + 1 dimensional viscous hydrodynamic simulation in Ref [148,149]. The study has shown that the coefficients a_{n,m} are not sensitive to the transport properties of the QGP. It is however sensitive to the initial state longitudinal fluctuations and the hadronic re-scattering and decays at the final stages of the collisions. With the future upgrade, measurements of this observable at RHIC over

wide range of rapidity can provide insight about energy dependence of the longitudinal fluctuations, further constraining the initial state models of heavy ion collisions. Also since the effect of the hadronic phase is different at lower collision energies, the measurements at RHIC will be allowing ways to constrain the hadronic afterburner used in state-of-the art hydrodynamic simulations.

Another longitudinal decorrelation study was carried out by an AMPT model calculation [109], as shown in Figure 2-34 and Figure 2-35, where the correlation between the observed event plane in two rapidity ranges with a gap of $\Delta\eta$ is calculated as $C_n(\Delta\eta) \sim \cos n(\Phi_n(\eta_A) - \Phi_n(-\eta_B))$ with $\Delta\eta = |\eta_A - \eta_B|$. A strong decorrelation is observed for both $n = 2$ and $n = 3$ in all centralities with increasing $\Delta\eta$. Hence the effect should be easily measurable. It is interesting to see that the decorrelation effect is much stronger at RHIC energies than that at the LHC energies. Measuring these longitudinal flow decorrelations, as well as the forward-backward (FB) asymmetry (possible with two event-plane detectors), would provide a better understanding of the longitudinal dynamics of heavy-ion collisions, as well as inputs for tuning of the event-by-event 3+1D viscous hydrodynamic models.

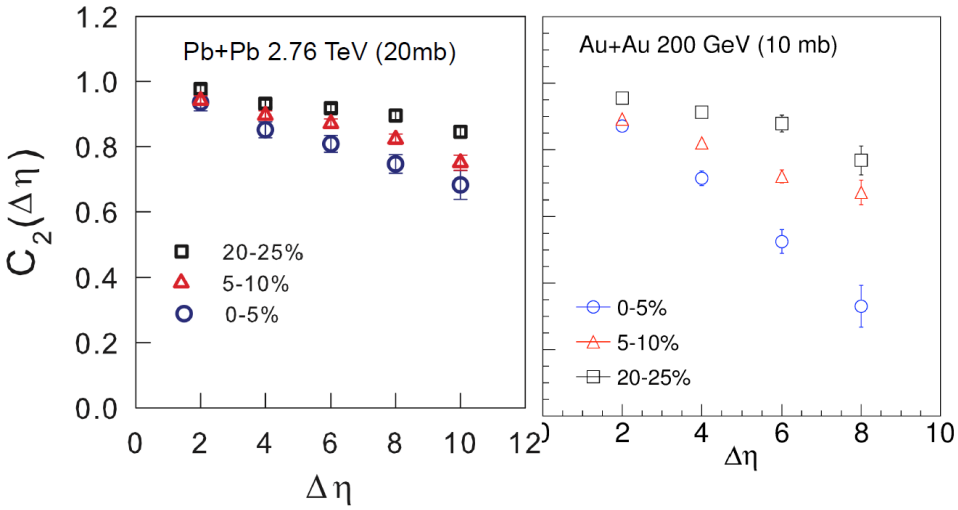


Figure 2-34: AMPT simulations of $v_2$ decorrelation as a function of pseudorapidity at the LHC and at RHIC with given parton cross-sections.

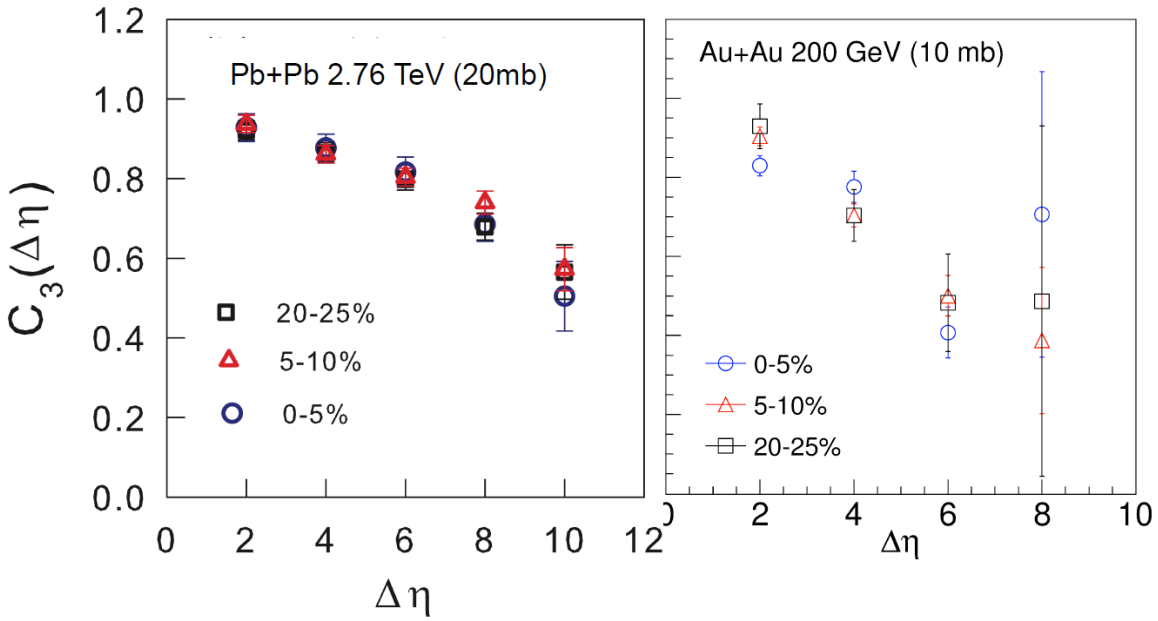


Figure 2-35: AMPT simulations of $v_3$ decorrelation along the pseudorapidity at the LHC and RHIC with given parton cross-sections.

A hydrodynamic simulation of longitudinal decorrelation of elliptic flow has been performed [109], taking into account the STAR forward calorimeter detector resolution. The transverse energy distribution is defined by the particle transverse spectra as:

$$\frac{dE_T}{d\eta d\phi} = \sum_{i=\pi^{\pm},K^{\pm},p} \int \frac{dN_i \sqrt{p_T^2 + m_i^2}}{d\eta p_T dp_T d\phi} p_T dp_T$$

and the flow vector ($Q_n$) can be defined from the transverse energy as:

$$\mathbf{Q_n} = Q_n e^{in\Phi_n} = \frac{1}{E_T^{tot}} \sum_{j=1}^{N} E_T^j e^{in\phi_j},$$

with $Q_n$, the flow correlation function between two different rapidities, defined as follows:

$$C_n(A,B) = \frac{< Q_n(A) Q_n(B) e^{in[\Phi_n(A) - \Phi_n(B)]} >}{\sqrt{< Q_n^2(A) >} \sqrt{< Q_n^2(B) >}}$$

Figure 2-36 shows the simulation results for different detector energy resolution, and for comparison with multiplicity measurements. It is interesting to observe that the measurements are not very sensitive to energy resolution within the predicted detector resolution range, and the calorimetry measurement is more sensitive to decorrelation than the multiplicity measurement, possibly due to the energy weight which may be more directly coupled with energy fluctuation.

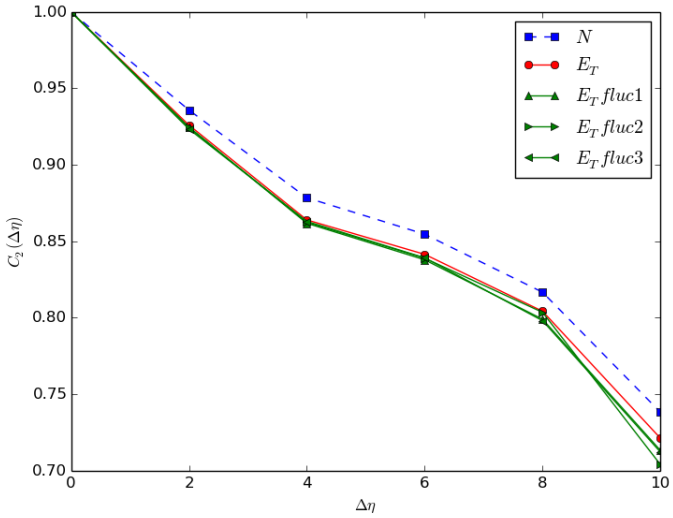


Figure 2-36: Hydrodynamic simulation of elliptic flow decorrelation in the form of $C_2$ as a function of pseudorapidity distance ($\Delta\eta$) at RHIC with STAR Forward Calorimeter detector resolutions [109] with three different energy resolutions.

### 2.4.2 Mixing and Phases of flow harmonics

In the transverse direction, current state-of-art flow correlation measurements are focused on a large class of new multi- harmonic observables, which are sensitive to higher-order eccentricity fluctuations in the initial state and mode-mixing effects in the final state evolution. The interplay between these two contributions leads to non-trivial correlations between multiple event planes of different order. Many such event plane correlators have been measured at the LHC [146, 147], and have been shown to be sensitive to the nature of the initial density fluctuations and dynamics of the collective evolution, as well as the EOS and temperature dependence of the η/s (see Fig. 2-37). Measurements of these observables at RHIC at mid- and forward-rapidities, and, very importantly, as a function of pT , are expected to provide strong constraints on the space-time picture and medium properties at lower temperatures. These measurements require correlations of the flow signal in several non-overlapping pseudo-rapidity windows. The limited detector coverage of STAR and PHENIX currently prevent such studies at RHIC but the forward upgrade program will provide such capabilities. Construction of correlations between mid-rapidity and forward rapidity can be performed with an event plane detector (EPD) with fine granularity. However, experiments at the LHC (ATLAS and CMS) have shown the importance, and power, of using energy flow from forward calorimetry to construct correlations at forward rapidity. Forward tracking and calorimetry provide the necessary energy and momentum measurements at the different rapidities used for these novel correlation functions.

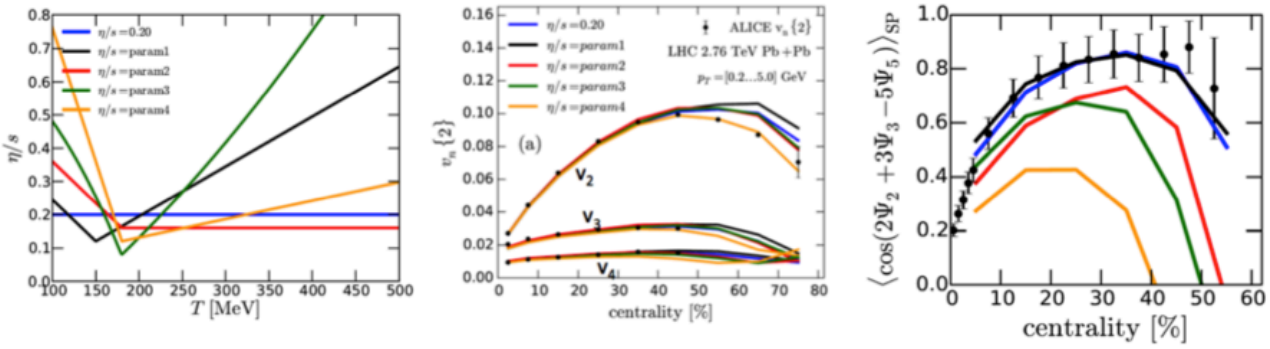


Figure 2-37: The predictions from an ebye viscous hydrodynamic model calculation of the $v_n$ (middle panel) and one example event plane correlator (right panel) for five different temperature-dependent η/s (left panel) at the LHC energy. The comparison shows that the EP correlators can distinguish the five predictions obtained with same <η/s> but different temperature dependence, while the inclusive $v_n$ measured at one collision energy can not.

STAR has been in the forefront of anisotropy measurements throughout the entire RHIC program. Many of the previous measurements have relied on the TPC to provide both the event plane and the $v_n$ measurement using independent sub-events, and often with only a small $\eta$ gap in between. These requirements effectively reduce the available statistics, but yet can't completely remove non-flow effects, especially significant for high $p_T$ anisotropy measurements. This limitation is especially severe for BES, due to smaller particle multiplicities and flow signals. One important capability, enabled by the STAR forward upgrade, will be the independent measurement of the event plane in the forward rapidity $2.5 < \eta < 4$ with significant gap from TPC ($|\eta| < 1.5$). Studies by the LHC experiments show that the rapidity gap is very important to suppress various auto-correlation effects, such as jet fragmentation and resonance decays. Many anisotropy measurements previously limited by systematics or statistics are now possible, for example:

- Detailed measurements of $v_n(p_T,\eta,\text{PID})$ for $n = 1$ to 5, which allow detailed control of initial state geometry and QGP transport properties.
- Leading single particle, photon or jet $v_n$ out to very high $p_T$ to probe jet tomography or the path-length dependence of jet quenching.
- Event plane angle dependent dihadron correlations to probe the jet-medium response benefit from enhanced EP resolution and reduced jet bias.
- Improved anisotropy study of other rare probes, such as $J/\psi$, heavy flavor including $D$ meson or single leptons, and di-leptons.

One important insight revealed by the measurements of event plane correlations and hydrodynamic model calculations is that a given flow harmonics $v_n$ is driven not only by the associated eccentricity, $\varepsilon_n$, but also receives contributions from lower order flow harmonics via non-linear mode-mixing effects in the final state (like overtone in music instruments). The elliptic flow $v_2$ and triangular flow $v_3$ are primarily driven by the ellipticity vector $\varepsilon_2$ and triangularity vector $\varepsilon_3$ of the initially produced fireball [110,111].

The physics potential for the full exploration of flow correlation depends on the detector coverage in η, $p_T$ and PID (assuming full coverage in azimuth). As Fig. 2-38 demonstrates, the STAR forward upgrade extends the two-particle phase-space in η (in terms of $\eta_1 \times \eta_2$) by a factor of 2 with $p_T$ information [from $(2+1x2)^2=16$ to $(3.4+2)^2=29$]. Having the $p_T$ information in the forward

detector will make it possible to study the differential transverse flow in forward rapidity, where the space-time picture of the QGP is expected to be very different. By correlating that with information at mid-rapidity, they also provide detailed information on the $p_T$ dependence of the longitudinal asymmetry and decorrelation effects. In turn, this information will elucidate the space-time dynamics of the QGP in the longitudinal direction and hence provide unique/critical input for current theoretical effort in tuning the 3+1D hydrodynamic models.

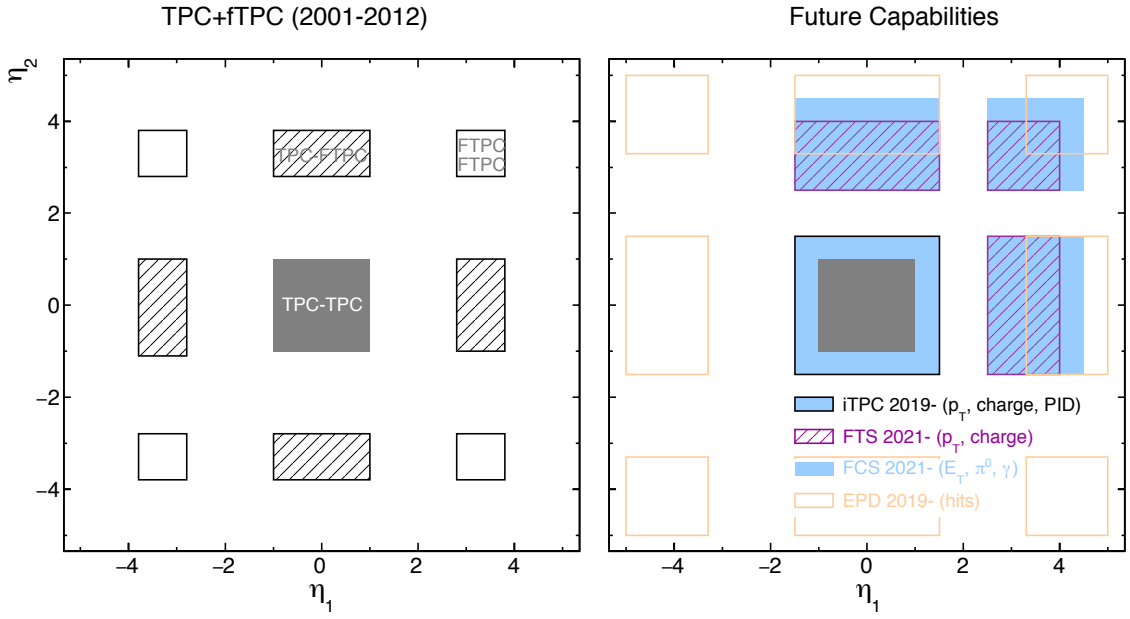


Figure 2-38: (left panel) The pseudorapidity coverage in $\eta_1 \times \eta_2$ of the STAR detector prior to the removal of FTPC in 2012. (Right panel) The projected $\eta_1 \times \eta_2$ acceptance after the iTPC and forward upgrade.

Finally, STAR can take advantage of the flexibility of the RHIC machine to measure these observables in different collision systems and beam energies. As an example, it would be highly desirable to measure the $p(v_2)$ and event plane correlations in U+U and Cu+Au collisions where the QGP properties are similar to Au+Au collisions but with completely different collision geometry. For the measurement of event plane correlations in STAR, experiences from LHC experiments [112] show that it is very important to have multiple non-overlapping detectors that provide independent measurement of $\phi_n$ as well as cross-checks to control the systematic uncertainties.

### 2.4.3 Event-shape engineering

The granularity and large acceptance of the forward detectors will enable STAR to sort events according to their apparent ellipticity or triangularity and then measure the $vn$ signal in the mid-rapidity with the TPC (see Figure 2-39). This event shape engineering technique was proposed in Ref. [112], and recently successfully applied to ALICE and ATLAS data analysis [113]. The proposed implementation in STAR would be to first Fourier expand the multiplicity in the EPD, and then study the response of the collective flow signals (including radial flow) at mid-rapidity via TPC to various EPD selected shapes. The study performed by the ATLAS collaboration shows that the $v_2$-$v_n$ correlation with in a fixed centrality not only provides a means to directly separate the linear and non-linear effect in $v_4$ and $v_5$ but also the intrinsic initial geometry correlation between $E_2$ and $E_n$. Figure 2-40 shows that the measured $v_2 - v_4$ contains a quadratic term that is

proportional to $v_2^2$ and $v_2 - v_5$ correlation contains a linear term that is proportional to $v_2 v_3$, consistent with expectation. On the other hand, the significant anti-correlation between $v_2$ and $v_3$ seems to be entirely due to anti-correlations between $\varepsilon_2$ and $\varepsilon_3$. Hence the $v_2$-$v_n$ correlations provide information on both initial geometry and final state non-linear mode mixing. Similar event-shape engineering measurements hold great promise at the future RHIC heavy ion program and can be performed with the utilization of the forward detectors in STAR.

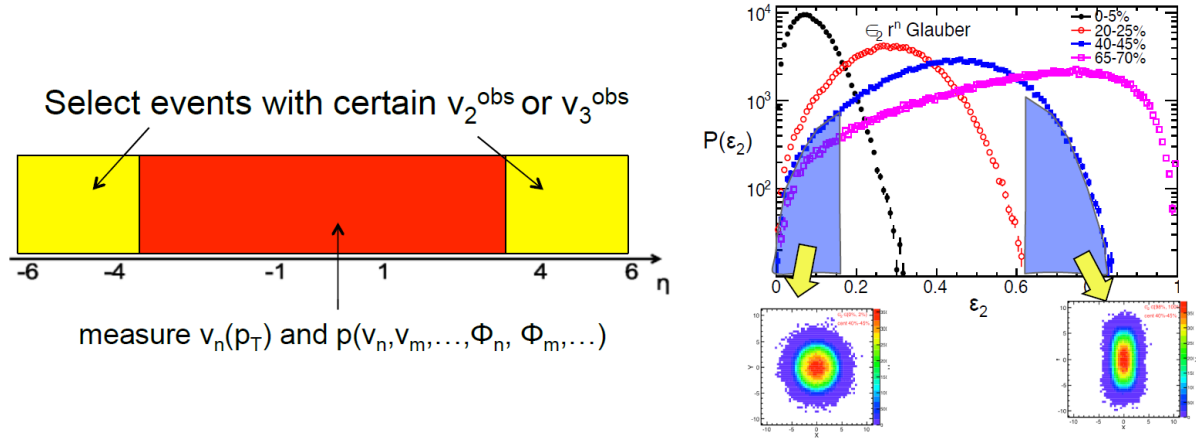


Figure 2-39: Schematic view of the event-shape selection technique (left panel) and the expected variation in the ellipticity $e_2$ (right panel).

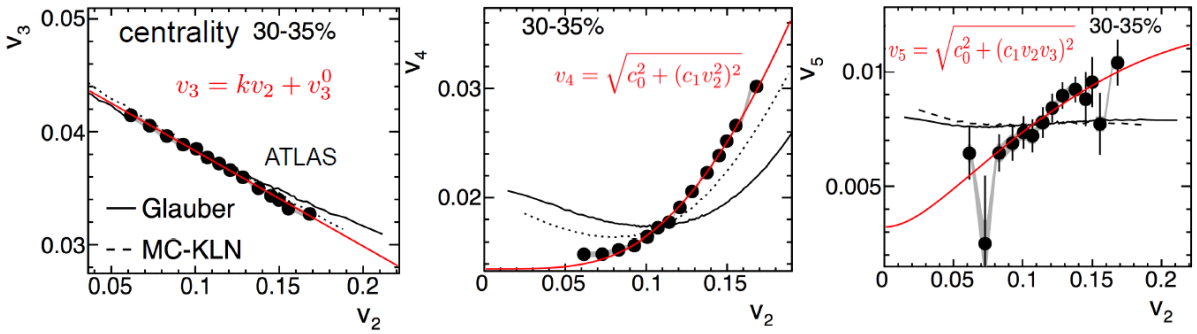


Figure 2-40: The correlations between $v_2$ and $v_3$ (left panel), $v_2$ and $v_4$ (middle panel), $v_2$ and $v_5$ (right panel) at the LHC. Each data point corresponds to one event shape class based on $v_2$ observed in the forward rapidity window $3.3<|\eta|<4.8$.

### 2.4.4 Jet-medium interaction

High-$p_T$ hadrons and jets are strongly suppressed in heavy-ion collisions compared to pp and p/dA collisions. It is generally accepted that the suppression is due to partonic energy loss due to jet-medium interactions. The energy lost by high-$p_T$ particles reemerges as low-$p_T$ particles—high-$p_T$ particle yields are suppressed and low-$p_T$ particle yields are enhanced. How the low-$p_T$ particles are distributed relative to the original jet direction should shed light on the jet-interaction mechanisms. Measurements of these types of jet-correlations are challenging because at low $p_T$ the anisotropically flowing background dominates the jet dependent correlation. The subtraction of this flow background involves large uncertainties because not all of the hydrodynamic flow parameters are measured to the required precision. Furthermore, there is a fundamental limit that anisotropic

flows are measured intrinsically by two-particle correlations that are also used for jet-correlation measurements.

STAR has recently devised an experimental method to robustly subtract anisotropic flow background by using a data driven technique. Figure 2-41 illustrates the analysis method utilizing only the main TPC. First we ask for a high-$p_T$ trigger particle within the pseudo-rapidity range of $0.5<\eta<1$. To enhance the probability that the away-side jet also resides in the same $\eta$ region, we then further select events with a large $p_T$ recoil (the summed $p_T$ in the azimuthal hemisphere opposite to the trigger particle $|\Delta\phi|>\pi/2$). Dihadron correlations in the "close-region" of $0<\eta<0.5$ and in the "far-region" of $-0.5<\eta<0$ are then analyzed. Given the width of the away-side jet in $\eta$ its contribution is significantly larger in the close-region than in the far-region, but the underlying flow backgrounds are identical; assuming little $\eta$ dependence in this range. By subtracting the correlation in the far-region from that in the close-region, we obtain the away-side jet-correlation signal completely devoid of flow contributions. The measured signal will only be the partial away-side jet-correlation, but the correlation shape is a robust measurement. The correlation shape measurement provides insights on the away-side jet-medium interactions.

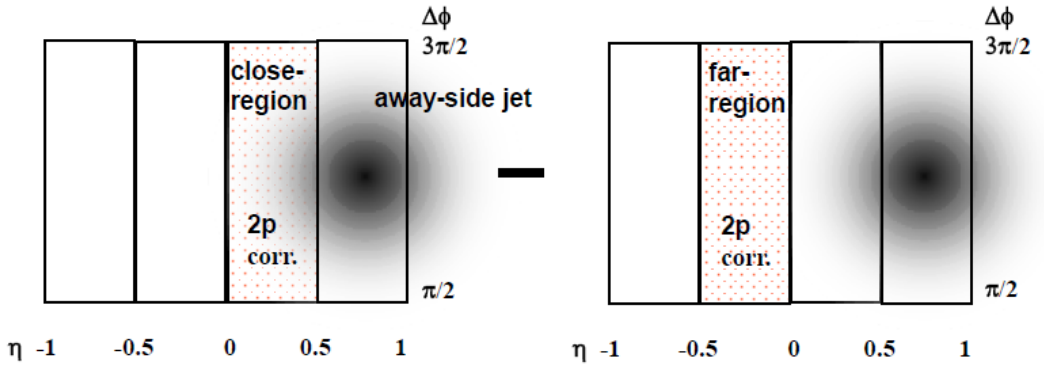


Figure 2-41: Schematic illustration of the methodology of the novel away-side jet correlation analysis.

# 3 Forward Upgrade Overview and Simulation

## 3.1 Forward Calorimeter System

The STAR forward upgrade is motivated mainly by exploration of QCD physics in the very high and low regions of Bjorken *x*. Previous STAR efforts using the FPD and FMS detectors and the recently refurbished FMS and a new pre-shower detector upgrade for Runs 2015-2017 have demonstrated that there are outstanding QCD physics opportunities in the forward region. In order to go beyond what STAR has/will achieve with the currently existing forward detector system, a forward detector upgrade with superior detection capability for neutral pions, photons, electrons, jets and leading hadrons covering a pseudo-rapidity region of 2.5-4.5 in the years beyond 2020 is proposed.

The design of the FCS' is a follow up development of the original proposed FCS system and is driven by detector performance, integration into STAR and cost optimization. The big reduction in the cost for the FCS' is achieved by replacing the originally proposed W/ScFi SPACAL ECal with the refurbished PHENIX sampling ECal. In addition, the FSC' will utilize the existing Forward Preshower Detector ($2.5 < \eta < 4$) operated in STAR since 2015. The proposed FCS' system will have very good (~ 8%$\sqrt{}$ (E)) electromagnetic and (~ 70%/$\sqrt{}$ (E)) hadronic energy resolutions. FCS' consists of 2000 of the 15552 existing PHENIX EMCal towers and 480 HCal towers covering an area of approximately 3 m × 2 m. The hadronic calorimeter is a sandwich lead scintillator plate sampling type, based on the extensive STAR Forward Upgrade and EIC Calorimeter Consortium R&Ds. Both calorimeters will share the same cost effective readout electronics and APDs as photo-sensors. It can operate without shielding in a magnetic field and in a high radiation environment. By design the system is scalable and easily re-configurable. Integration into STAR will require minimal modification of existing infrastructure.

In the past three years we carried out an extensive R&D program to develop sampling calorimeters for the STAR forward upgrade and the EIC barrel and forward/backward calorimeters including successful test beam runs of full-scale prototypes at FNAL. To have an easy re-configurable calorimeter system was one of the main design goals for the system.

The STAR BNL Electronics Group proposed to design and build a generic digitizer system ("Detector Electronics Platform", DEP) which would be cheap, fast & modular and could be used for many different applications within STAR and its upgrades and serve as a platform for future readout systems at EIC. The basic board would consist of 32 12bit ADCs running in sampling mode at 8x the RHIC clock. The ADC would be followed by a fast FPGA capable of running various digital filters and other typical trigger algorithms such as: pedestal & zero subtraction, charge integration, moderate timing information (to <1ns), highest-tower, tower sums etc. The system will be capable of connecting up to 5 such boards (for a total of 160 channels) into a compact & cost-effective chassis. The data will be sent to a DAQ PC over a fast optical link and will have enough bandwidth to work in full streaming mode for typical occupancies, if so desired. It would also house the STAR TCD interface for the RHIC clock and Trigger command, which would also act as a Slow Controls Interface if needed. An interface to current or future STAR DSM boards will also be provided. Readout of FCS' will be based on DEP with a backup option based on extending the existing QT readout system currently used in the FMS and FPS. Both options of the FCS readout schemes are cost wise the same.

Indiana University and the STAR BNL Electronics group will collaborate to design and

build frontend electronics for the FCS'. The calorimeter will use 1000 FEE boards each providing readout for one (HCAL) or four (EMCAL) towers using S8664-55 Hamamatsu APD's. The elements of the FEE board will include: Low noise preamplifiers based on BF862 JFET's, pulse shaping circuits, cable drivers designed to bridge either the DEP or existing QT boards, and temperature-compensated bias voltage regulators to provide a stable (<<1%) gain of the APD's. The bias voltage regulator and slow controls interface will be based on the successful FEE design for the STAR FPS; the preamplifier will be based on an Indiana University design for the aCORN experiment and on other BF862-based folded cascode designs. A multi-drop power & control interface cable will connect ~20 or more FEE boards to an output of the control interface box (TUFF-II), based on the TUFF box of FPS. This development is closely tied with an ongoing EIC generic detector R&D.

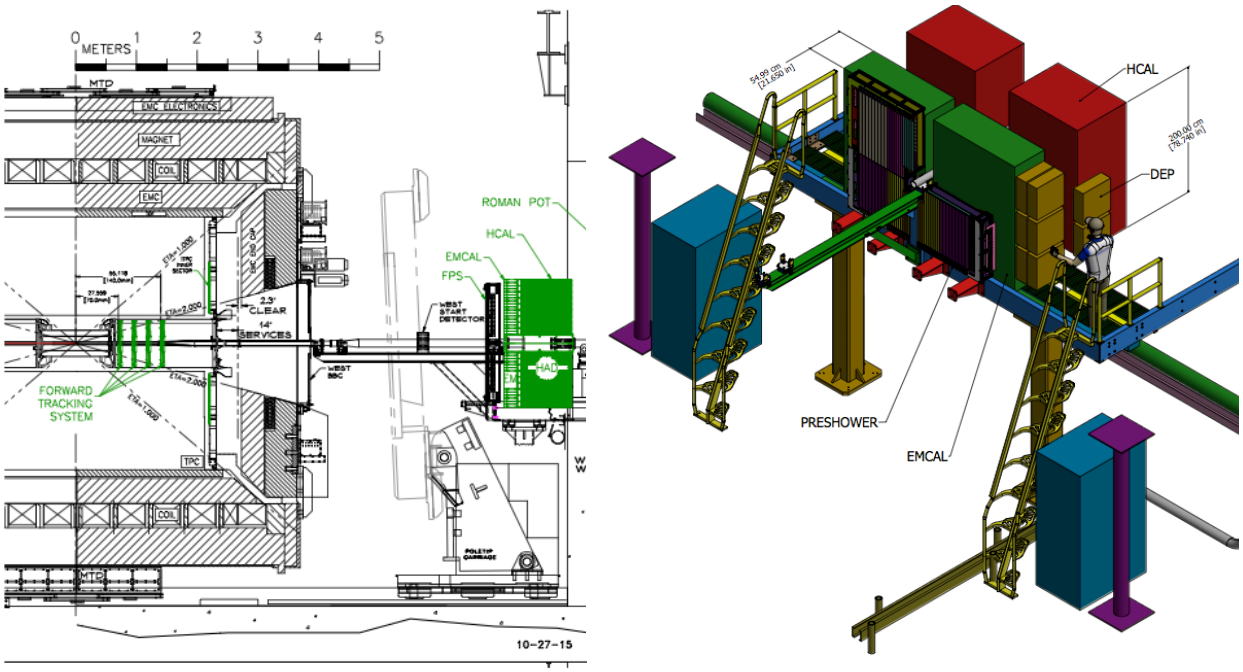


Figure 3-1: Location of the FCS at the West side of the STAR Detector system and a GEANT model of the FCS in the STAR simulation software

Figure 3-1 shows the location of the proposed FCS at the West side of the STAR detector system and a schematic description of the FCS in the STAR Monte Carlo simulation software. The read-out for the EMCal will be placed in the front so that there will be no significant dead gaps between the EMCal and the HCal. Wave-length shifting slats are used to collect light from the HCAL scintillating plates to be detected by photon sensors at the end of the HCal. Multiple Silicon PMTs will be used to read out each EMCal and HCal module, 4 for EMCal and 8 for HCal, respectively.

We developed a novel construction technique for HCal by stacking Lead and Scintillator plate in-situ. Students and post-docs just before the test run constructed an array of 4×4 prototype HCal modules at the FNAL test beam site. We envision that a full HCal detector can be assembled at the STAR experimental hall within a few months during the summer shutdown period.

## 3.2 Forward Tracking System

In addition to the Forward Calorimeter System, a Forward Tracking System (FTS) is also under consideration for the STAR forward upgrade project. Such an FTS has to cope with the STAR 0.5 T Solenoid magnet field to discriminate charge sign for transverse asymmetry studies and those of electrons and positrons for Drell-Yan measurements. It needs to find primary vertices for tracks and point them towards the calorimeters in order to suppress pile-up events in the anticipated high luminosity collisions, or to select particles from Lambda decays. It should also help with electron and photon identification by providing momentum and track veto information. In heavy ion collisions, it should be able to measure transverse momentum of charged particles in the range of $0.2<p_T< 2$ GeV/c with 20-30% momentum resolution. In order to keep multiple scattering and photon conversion background under control, the material budget of the FTS has to be small. These requirements present a major challenge for detector design in terms of position resolution, fast readout, high efficiency and low material budget.

STAR has considered the Silicon detector technology. STAR has gained considerable experience in the technology from the Intermediate Silicon Tracker (IST) construction in recent years.

Silicon detectors have been widely used in high-energy experiments for tracking in the forward direction. For example, Silicon strip detectors have been successfully used at many experiments: the Dzero experiment at the Tevatron, CMS and LHCb at the LHC, and PHENIX at the RHIC. More recent designs incorporate hybrid Silicon pixel detectors, which resulted in the improvement of position resolutions and removal of ghost hits, but unfortunately they also significantly increased the cost and material budget. According to preliminary Monte Carlo simulations, charge sign discrimination power and momentum resolution for the FTS in the STAR Solenoid magnet depends mostly on phi resolution, and is insensitive to the r-position resolution. Therefore a Silicon mini-strip detector design would be more appropriate than a pixel design. We are evaluating a design that consists of four to six disks at $z$ locations at about 70 to 180 cm. Each disk has wedges covering the full $2\pi$ range in $\phi$ and 2.5-4 in $\eta$. The wedge will use Silicon mini-strip sensors read out from the larger radius of the sensors. Compared to the configuration of reading out from the edges along the radial direction, the material budget in the detector acceptance will be smaller since the frontend readout chips, power and signal buses and cooling lines can be placed outside of the detector acceptance.

STAR will continue to evaluate these technology options for the FTS design. Continued R&D efforts are needed to demonstrate the technical feasibility of these options through Monte Carlo simulations and detector prototyping.

## 3.3 Detector Simulations

The sections below report on a number of simulations, both standalone and in the STAR simulation framework, that have been performed for the proposed FCS and FTS.

### 3.3.1 FCS detector simulations

The FCS has been implemented in the STAR simulation framework. STAR simulations have been performed to assess the response to single particles and jets, and to obtain response parametrizations. A sideview of the geometry is shown in Figure 3-1 (left). The electromagnetic section is modeled as 120 × 80 towers of 2.6 × 2.6 × 17 $cm^3$ size. Each tower contains W-powder and 780 scintillating fibers of 0.47 mm diameter. The hadronic section is positioned directly downstream of the electromagnetic section and consists of 30 × 20 towers of 10 × 10 × 81 $cm^3$ size. The simulated single-electron energy and geometrical response is shown in Figure 3-2.

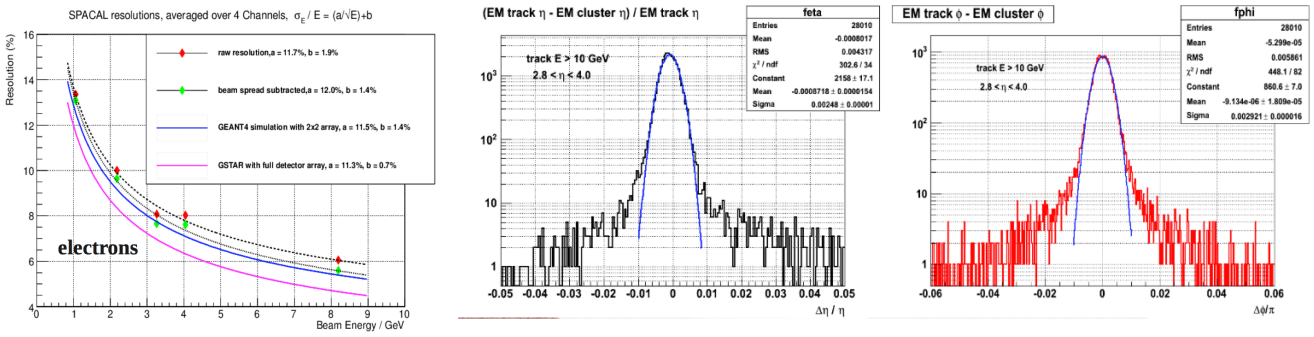


Figure 3-2: (left) The simulated FCS energy response to single electrons (purple), together with simulations and data from FNAL testbeam experiment T-1018; (middle) the simulated position resolution in pseudo-rapidity using a cluster-finder adapted from the existing STAR Forward-Meson-Spectrometer analysis package; (right) the corresponding azimuthal response.

The simulation of single-hadron response is considerably more involved than the electromagnetic response and typically requires tuning to obtain agreement with data. Figure 3-3 shows the single-hadron results from the same set of simulations as in Figure 3-2. The energy and transverse momentum response for jets, identified and reconstructed with the anti-$k_T$ algorithm and a cone size of 0.7, is shown in Figure 3-4.

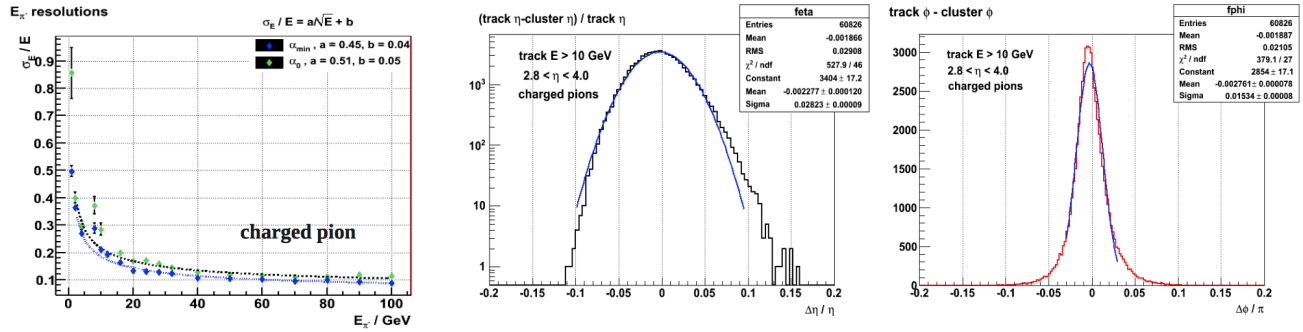


Figure 3-3: as in Figure 3-2, for single-hadrons.

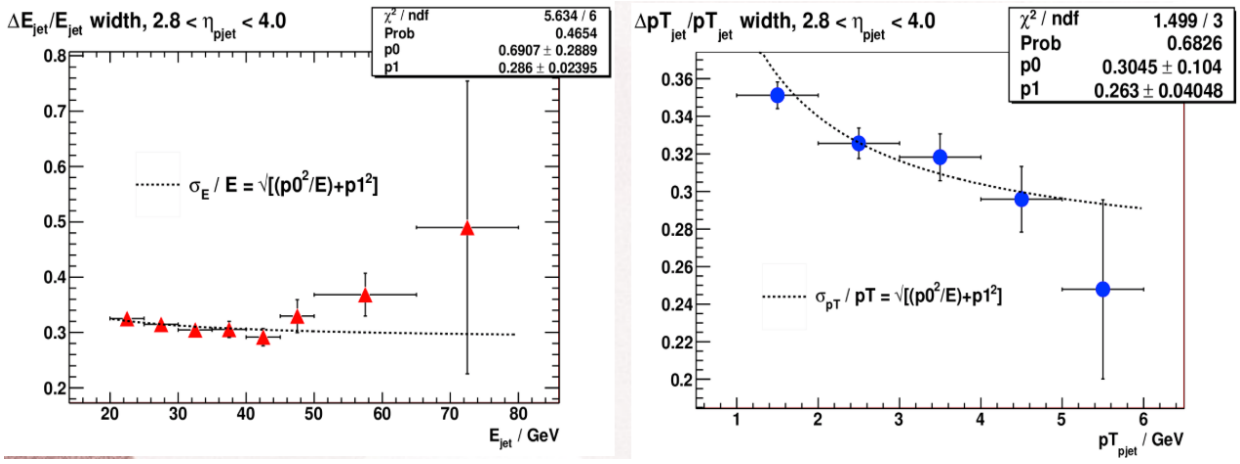


Figure 3-4: Simulated (points) and parametrized (curves) jet energy and transverse-momentum resolution with the FCS.

The simulation of hadronic response, in particular, is the topic of continued study in STAR. A prototype FCS has been constructed and used in test-beam experiment T-1018 at FNAL [114], as

part of ongoing STAR and EIC R&D. The combined electromagnetic and hadronic calorimeter geometry for the prototype, consisting of 4×4 electromagnetic and 4×4 hadronic towers, has recently been (re-)modeled in standalone GEANT4-based simulations [115]. Figure 3-5 shows the significant advance that has been made. Although these updated responses have not yet been propagated in the simulated physics observables, they are not expected to lead to qualitative changes.

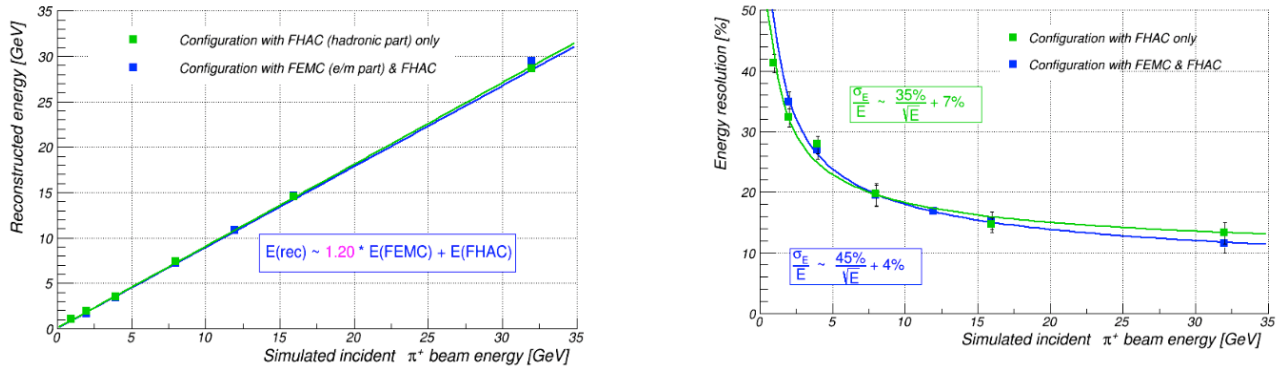


Figure 3-5: (Left) Simulated response linearity of the electromagnetic and hadronic sections, FEMC and FHAC, of the small-scale FCS prototype with incident hadron energies of up to 32 GeV. (Right) Simulated energy resolutions for this configuration.

### 3.3.2 Silicon-based FTS detector simulations

Below we evaluate the FTS design with 4-6 disks with realistic MC geant simulations. An FTS layout is shown in Figure 3-6, in which six FTS disks are placed at $z$ = 70, 93.33, 116.66, 140, 163.33, and 186.66 cm, respectively. In the simulations, each FTS plane has 12 wedges covering 2π in azimuthal angle $\phi$ and 2.5-4 in pseudo-rapidity $\eta$. Each wedge has 128 $\phi$ times 8 $\eta$ Silicon Mini-strips.

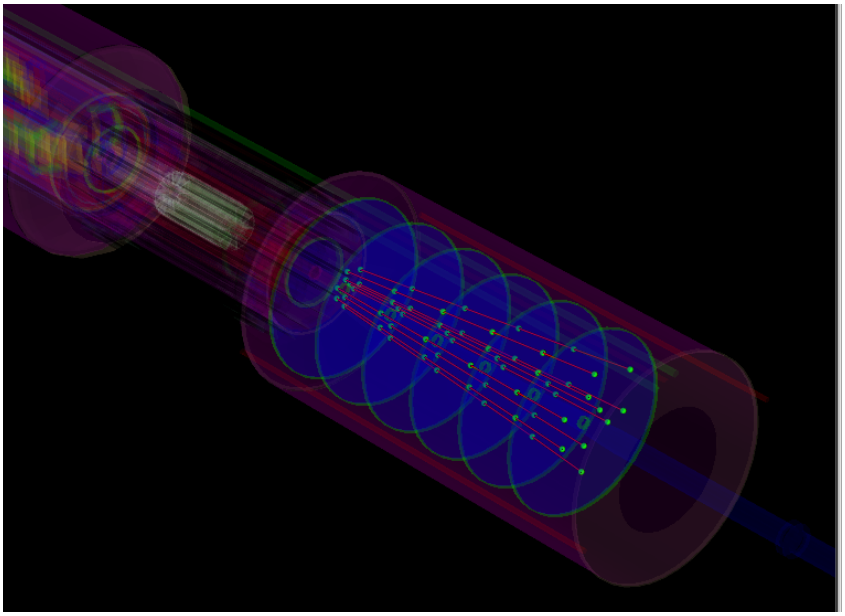

Figure 3-6: Layout of a Forward Tracking System consisting of six radially oriented Silicon Mini-strip planes located at at $z$ = 70, 93.33, 116.66, 140, 163.33, and 186.66 cm, respectively. Each of the planes includes 12 wedges, each with 128 strips in $\phi$ at a fixed radius and 8 strips in the radial direction at a fixed $\phi$ value.

The material budget per FTS disk is assumed to be 0.4% $X_0$. With the HIJING simulation, the occupancy in the most central (head-on) Au+Au collisions at $\sqrt{s_{NN}}$=200 GeV is estimated to be 5% (9%) at $\eta$ = 2.5 (4) for the first disk. For the fourth disk, the occupancy is 7% (13%) at $\eta$ = 2.5 (4). The higher occupancy for the disk further away from the collision center is due to the multiple-scattering effect.

The FTS geometry is implemented in AgML. Geant hits are available in standard hit tables. The simulation is fully integrated into STAR production simulation and reconstruction chain. The hits are segmented in radial and azimuthal directions according to the configurations mentioned above. The hits are placed at the center of the struck element. Multiple hits in the same segment are merged. These hits are exported to StEvent and read as input into the Stv Tracker. The next step is to perform Stv tracking finding, in which we use the standard Stv seed finder based on Sti seed finder used for nearly a decade. We then follow the track with the search window 5x track propagation error and require 4 consecutive hits to form a seed in the FTS. Finally we do Stv tracking fitting based on Kalman Track fitter in the distance of closest approach frame. FTS tracking is expected to run as a afterburner, after tracking in the TPC. We expect the primary vertex to be available for use when FTS tracks are reconstructed. Thus in the fitting, we also utilize Monte Carlo vertex with 50 micrometers uncertainty. In the following, we examine the tracker performance over a range of $p_T$ and under different track densities required for physics cases.

We input negatively charged pion particles in the simulation with uniform azimuthal angle and pseudo-rapidity distributions in the range of 2.5<eta<4.0. Three transverse momentum cases are studied: 0.2, 1 and 2 GeV/c and four track densities of 1, 10, 100, and 1000 per event are investigated.

Figure 3-7 shows the reconstructed transverse momentum (the nominal value) and its standard deviation (the bar) for charged pions at $p_T$=0.2, 1, and 2 GeV/c for 4 different track densities: 1, 10, 100, and 1000. The $1/p_T$ resolution has no strong track density dependence and is 16%, 22%, and 30% for $p_T$=0.2, 1, and 2 GeV/c, respectively.

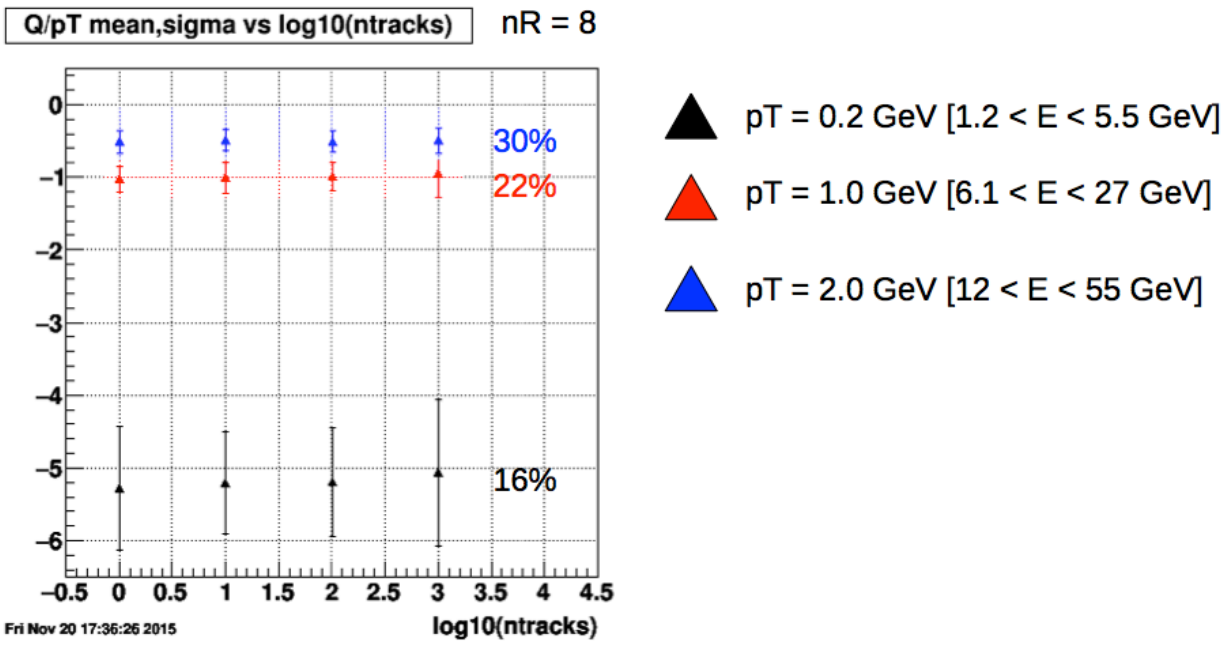


Figure 3-7: The reconstructed transverse momentum (the nominal value) and its standard deviation (the bar) for charged pions at $p_T$=0.2, 1, and 2 GeV/c for 4 different track densities of 1, 10, 100, and 1000 per event.

We also find that the track finding efficiency for the primary tracks (the tracks generated at the collision point) is about 80-90% when the track density is below 100 per event and drops significantly toward high density event. In addition, we increase the radial segmentation from 8 to 16, 32, and 64 and find no significant improvement on the momentum resolution and tracking efficiency.

Decreasing the number of the FTS disks will save the budget significantly. We have evaluated another two configurations, one with 4-disk configuration and the other with 5-disk configuration. For each configuration, instead of positioning each disk center at (0,0) at the transverse plane, we add additional offsets to the disk centers as shown in Figure 3-8 and rotate the disk by 360/ndisk degree, in which ndisk is 4, 5, 6 for the three cases individually.

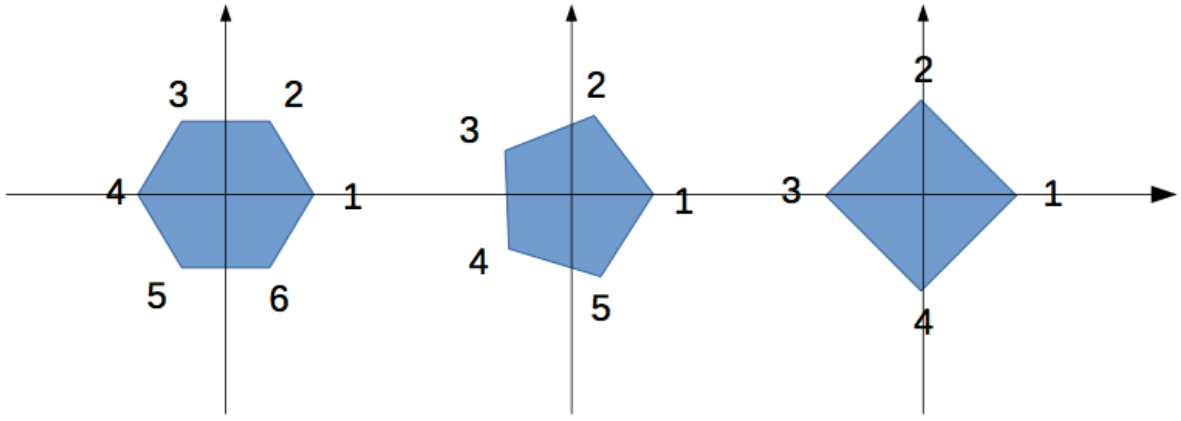

Figure 3-8: The offsets for each disk center in the transverse plane for 6-disk, 5-disk, and 4-disk configuration cases. For each configuration, every disk center is offset differently by 1 mm radially.

Figure 3-9 shows the performances of the 4-disk and 5-disk cases compare to the 6-disk

case. We find that the momentum resolution does not change when we reduce the disk number from 6 to 4. However, the efficiency is reduced from 95% to 80% when the track density per event is below 100.

We also find that adding 1 mm radial offsets to each disk center significantly improves the tracking. It removes degeneracies in the fits. It also enables us to reconstruct tracks with $p_T$ as large as 3 GeV, with 1 sigma charge sign separation. We note that the sagittas for the tracks of $p_T$=2 GeV/c at eta=2.5 are 125 μm, 500 μm, and 889 μm at disk 1, 4, and 6, respectively. The sagittas for the tracks of $p_T$=2 GeV/c at eta=4 are 6 μm, 25 μm, and 44 μm at disk 1, 4, and 6, respectively. For 2 GeV/c at eta=4, the sagitta that we are trying to measure is less than the azimuthal width of the proposed detector elements. With ideal alignment, one either gets all hits at the same phi location in which case the circle (helix) model fails; or discs 1 through N see one phi location, and discs N+1 through 6 see the next phi location, causing an overestimate of the curvature, and an underestimate of the $p_T$. Non-ideal alignment obscures this effect.

To summarize, we evaluate the silicon-based forward tracking system performance. We find that with 4 to 6 disk configuration, the forward tracking system can provide momentum measurements for charged particles in the range of $0.2<p_T<2$ GeV/c with 20-30% $1/p_T$ resolution. We note that the 4-disk configuration will reduce the tracking efficiency quite significantly, from 95% to 80%. We also find that the tracking efficiency will decrease in a high-density event, where further optimizations are clearly needed. Considering that 4 hits are minimum requirements for the tracking and that an imperfect detector acceptance is always the case in reality, we recommend at least a 5-to-6-disk configuration for the physics cases proposed here.

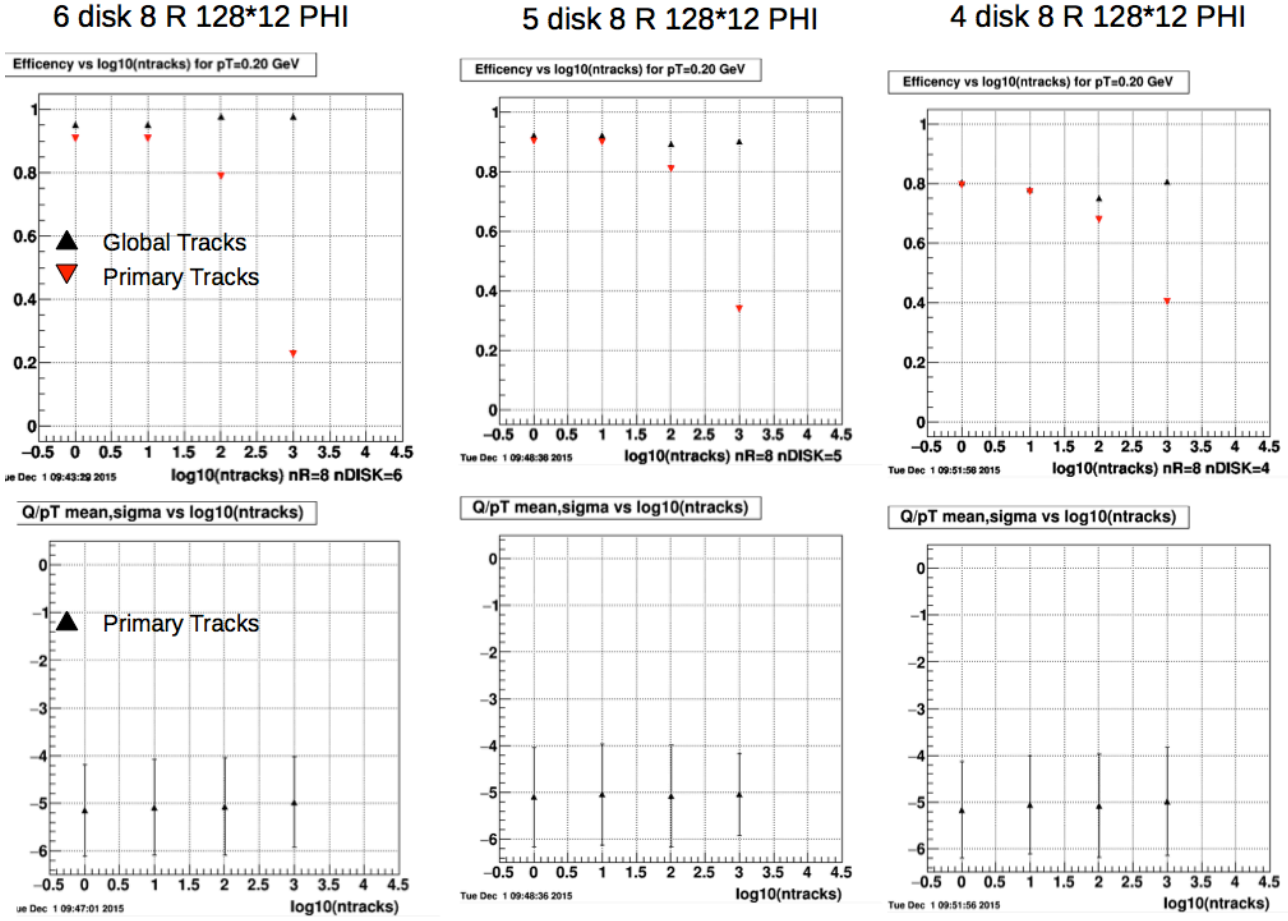


Figure 3-9: The tracking finding efficiency for primary and global tracks (top panels), and the momentum resolution (bar of the data points in bottom panels) for negatively charged pions at

$p_T$=0.2 GeV/c as a function of track density per event.

In addition, a simulation study based on the EICROOT frame has been performed to investigate the performance of the propose FTS. The study uses a full geometrical modeling of the existing STAR detectors as well as the FTS in GEANT4. Tracks are generated either with a flat distribution in $p_T$, eta and phi, or according to the distribution from the Hijing generator. Track finder and fitter are based on offline reconstruction codes developed by the HERMES and OLYMPUS experiments:

- Track finder: global "tree search" in {q, phi, 1/p} parameter space (assuming vertex is ~known); individual-hit-to-parameter-space Hough transform; embedded Kalman-filter-based ambiguity resolution logic.
- Track fitter: Kalman filter node chain of variable length (multiple hits per plane possible, etc); material effects included (multiple scattering for hadrons as a process noise model); fixed-location linearized Runge-Kutta track propagation in the magnetic field; automatic iterative outlier hit rejection based on the smoother $c^2$ (optional); specifically tuned for forward spectrometer geometries.

Configurations with 6 disks have been studied extensively with the disks located at Z= 62.0cm, 83.3cm, 106.7cm, 140.0cm, 163.3cm, and 186.6cm, respectively (see Figure 3-10).

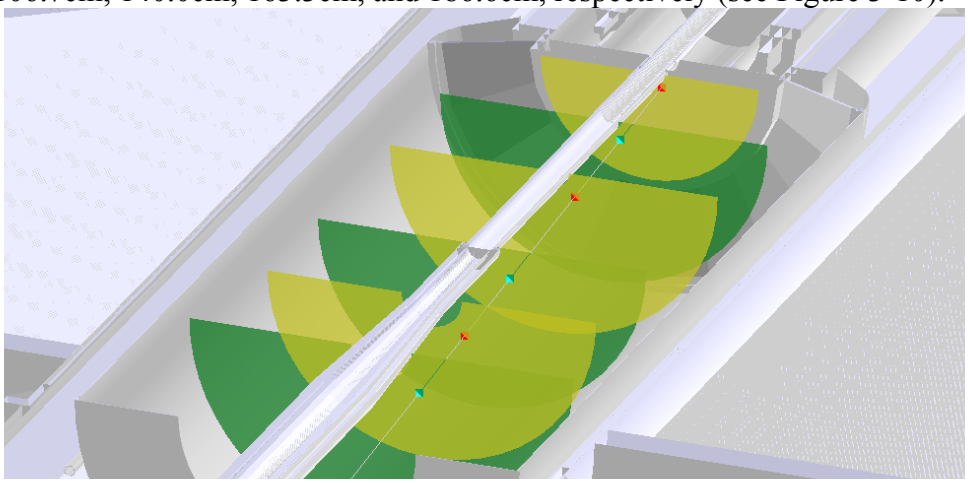

Figure 3-10 Forward Tracking System and other components of the STAR experiment in the forward direction. Also shown is the trajectory of a charge pion and the associated hits on the FTS disks.

The configurations include:

A. Disks are made of Silicon pixel sensors with a thickness of 0.2 mm and pitch size of 20*20 microns;
B. Disks are made of Silicon ministrip sensors with a thickness of 0.4 mm and 128*12 strips in phi at any given radius, and each strip has a 1 cm[1] length along the radius direction;
C. Same as B but the number of strips is 128*12*2 in phi at any given radius.

The results of the simulation can be summarized as the following:

- Track finding efficiency is well above 90% (see Figure 3-11).
- Transverse momentum resolution for $p_T$<2 GeV/c is better than 20%, 10% and 5% for theta=3, 5 and 8 degree[2], respectively, for configuration A. There is no strong bias in the

[1] Due to a limitation in the version of EICROOT that was used in this study, only strips with constant radial length can be used. However, the pT resolution is found to be insensitive to the strip length by varying the strip length by a factor of 2.

[2] Theta=3, 5, 8 degree correspond to eta=2.660, 3.131, 3.643, respectively.

reconstructed $p_T$ (see Figure 3-12).

- Transverse momentum resolution for $p_T$<2 GeV/c is better than 50%, 40% and 25% for theta=3, 5 and 8 degrees, respectively, for configurations B and C. The bias is as large as 20% at theta=3 degree, and is less than 5% at theta=5 and 8 degree (see Figure 3-13).
- There is no obvious improvement by configuration C than B (see Figure 3-14).

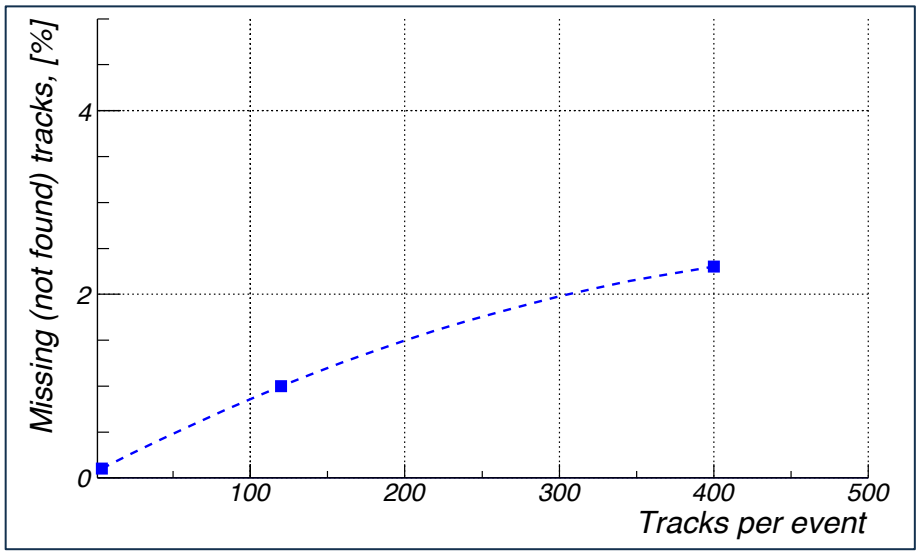


Figure 3-11 Track finding inefficiency as a function of number of tracks per even in 2.5<eta<4. The track kinematic distributions are based on Hijing simulation.

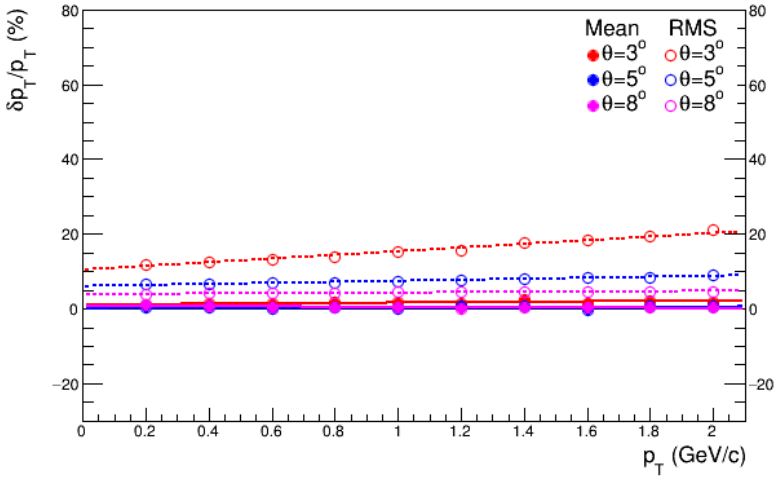


Figure 3-12 Mean and RMS of reconstructed transverse momentum distribution as a function of generated transverse momentum for configuration A.

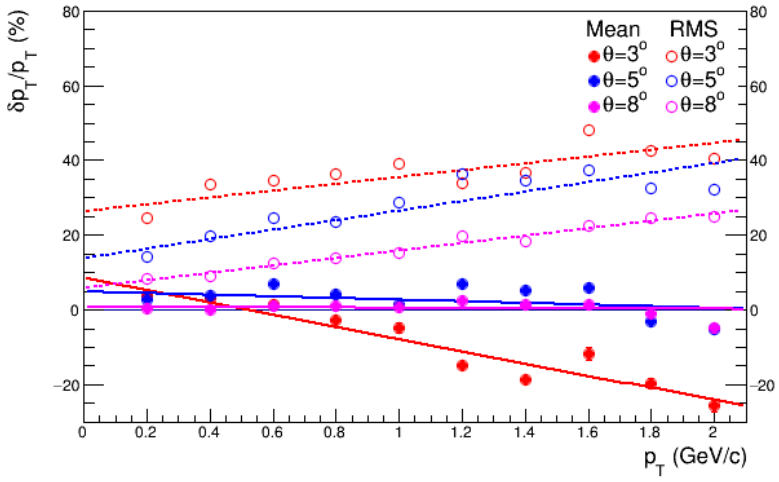


Figure 3-13 Mean and RMS of reconstructed transverse momentum distribution as a function of generated transverse momentum for configuration B.

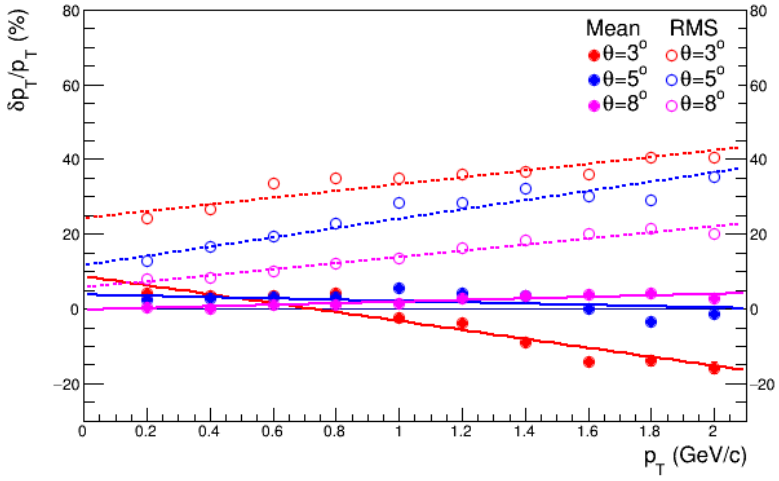


Figure 3-14 Mean and RMS of reconstructed transverse momentum distribution as a function of generated transverse momentum for configuration C.

## 3.4 Physics Simulations

The measurement of jets and of Drell-Yan production processes are of key importance to the science of the proposed FCS and FTS. These topics are discussed below in sections 3.4.1 and 3.4.2. Section 3.4.3 describes two of the key measurements that are enabled by the FCS and FTS and quantifies the anticipated measurement precision.

### 3.4.1 Jet measurements

We have studied how in single- and di-jet events, the jet pseudorapidity $\eta$ and $p_T$ are related to the underlying partonic variables $x_1$ and $x_2$. We also studied the matching between reconstructed jets and scattered partons and the resolutions with which the parton axis can be reconstructed from the reconstructed detector jets. The latter is important to evaluate how well azimuthal asymmetries around the outgoing parton axis will be reconstructed by looking at asymmetries of reconstructed particles around the reconstructed jet axis.

For this study we used 500k events simulated with Pythia Tune A at $\sqrt{s}$=500 GeV and a minimum partonic $p_T$ (CKIN3) of 3 GeV. We then used a fast simulation of the detector resolutions

of the STAR barrel and the forward upgrade. For the purpose of this study we assumed a tracking detector with three planes at distances from the interaction point of 70 cm, 105 cm and 140 cm. Each plane is comprised of 1.2% radiation lengths of material with resolutions in the azimuthal direction between 0.11 and 0.85 mm/$\sqrt{12}$. Furthermore, we simulated a detector subsystem combining hadronic and electromagnetic calorimeters (FCS) with $0.58/\sqrt{E}$ hadronic resolution and an electromagnetic resolution of $0.11/\sqrt{E}$. In this setup, except for those tracks with very low energy, the track momentum is reconstructed in the FCS and the tracking is used mainly for charge discrimination. Jets were reconstructed with an anti-$k_T$ algorithm with a radius of 0.7. An association between reconstructed jets and scattered partons is defined to be a distance in $\eta$-$\phi$ space of less than 0.5.

In the following, we refer to reconstructed jets as "detector jets" and jets found using stable, final state particles "particle jets." The outgoing partons in the event are determined by using the corresponding entries in the Pythia record, so there is no partonic jet finding.

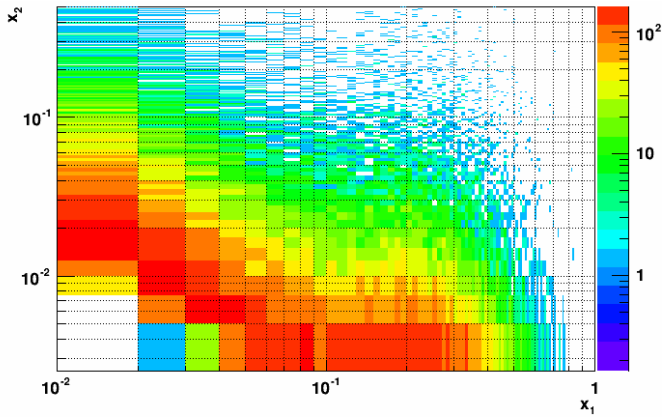


Figure 3-15: Distribution of the partonic variables $x_1$ and $x_2$ for events with a jet with $p_T > 3$ GeV/$c$ and $2.8 < \eta < 3.5$. $x_1$ values of around 0.6 can be reached whereas $x_2$ goes as low as $7\times10^{-3}$.

Figure 3-15 shows the regions of $x$ that can be accessed by jets in the forward region. A minimum jet $p_T$ of 3 GeV/$c$ was chosen to ensure that the momentum transfer is sufficiently high for pQCD calculations to be valid. At high $x$, values of $x$~0.6 should be reachable. This compares well with the current limit of SIDIS measurements, *x~0.3*, and encompasses the region in $x$ that dominates the tensor charge. To investigate the possibility of selecting specific $x$ regions, in particular high $x$, the dependence of $x$ on the jet $p_T$ and pseudorapidity was studied.

Figure 3-16 shows $x_1$ as a function of jet $p_T$ and Figure 3-17 and Figure 3-18 show the $\eta$ dependence for two $p_T$ bins. For both the $\eta$ and $p_T$ dependences one can observe two bands: One that exhibits an $\eta$ or $p_T$ dependence and one that remains at low $x$. Based on the profile plots in Figure 3-17 and Figure 3-18, high $x$ can be reached with small dilution for high $\eta$ and $p_T$.

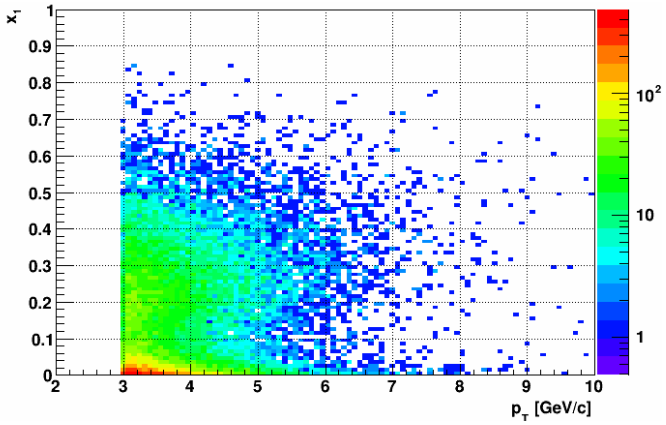


Figure 3-16: $x_1$ versus jet $p_T$. As expected, there is a correlation between the $x$ accessed and the $p_T$ of the jet. However, there is an underlying band of low $x_1$ values. This can be improved by further restricting the $\eta$ range of the jet. Here $2.8 < \eta < 3.8$.

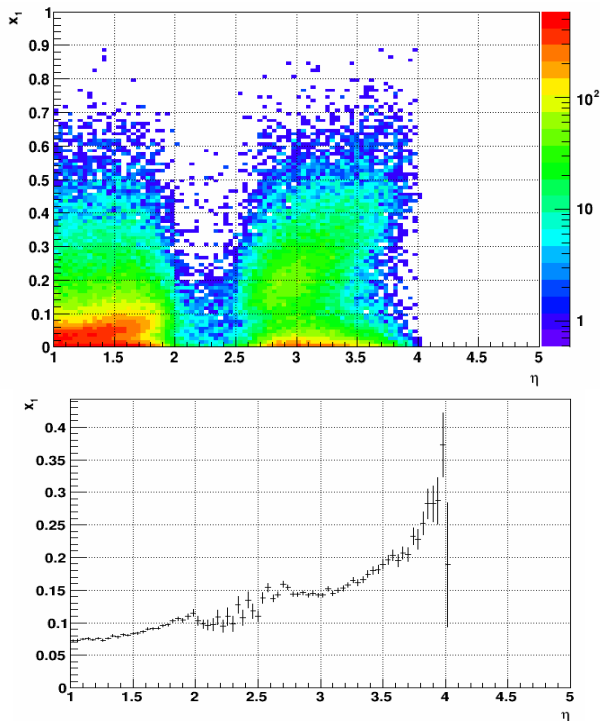


Figure 3-17: $x_1$ vs jet $\eta$. The upper figure shows a 2D histogram and the lower figure the profile plot. Here a minimum jet $p_T$ of 3 GeV/$c$ was required. One can see that the events are split into two bands. One exhibits a strong correlation with $\eta$, whereas the other is flat at low $x_1$. In the region of the forward upgrade $x_1$ values between 0.15 and 0.3 are accessible.

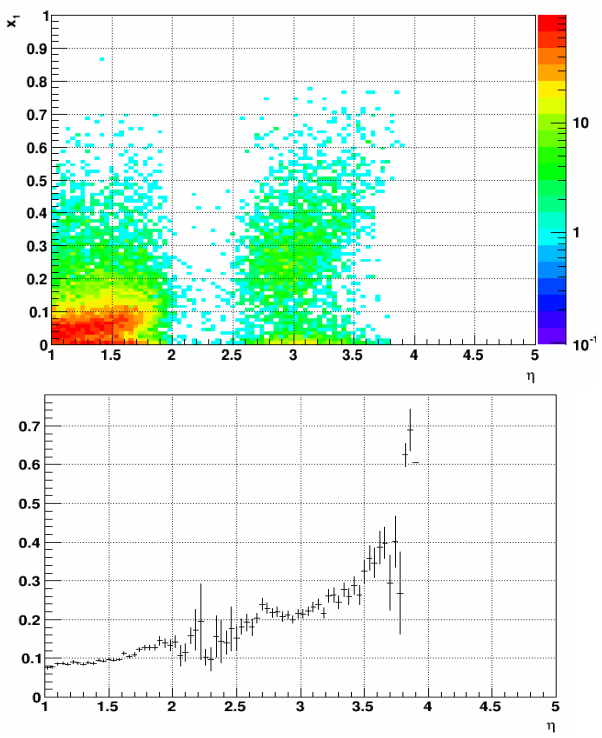


Figure 3-18: Same as in Figure 3- but with a minimum jet $p_T$ of 5 GeV/$c$. This shows that additional $p_T$ cuts allow one to push the accessible mean $x$ to higher values. In this case, $x_1$ values between 0.2 and 0.4 are achievable.

For measurements of azimuthal asymmetries of jets or hadrons within a jet to probe the transverse spin structure of the nucleon it is important to reconstruct reliably the outgoing parton direction. Therefore, the matching of reconstructed jets to scattered partons was studied (Figure 3-19). Figure 3-20 and Figure 3-21 show the mean distance of partons to associated detector jets and detector jets to associated particle jets. In general, matching and parton axis smearing improves with $p_{T,}$ which may be connected to the jet multiplicity that rises with transverse momentum. Figure 3-22 and Figure 3-23 give the $p_T$ and resulting $z$ smearing for the reconstructed jets. Here, $z$ is defined as the fractional energy carried by the fragmenting hadron. The reconstruction of the transverse momentum is poor, but z exhibits a more favorable correlation. Possible explanations are compensation between jet and hadron momentum smearing and the domination of the $z$ correlation by high multiplicity jets where the jet $p_T$ reconstruction is more reliable.

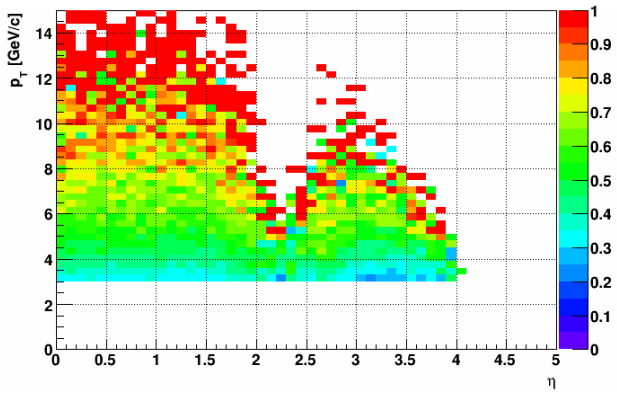


Figure 3-19: Matching Fraction between detector jets and partons. The matching fraction at low $p_T$ is only around 50%, but grows to over 90% for high $p_T$. Unfortunately, the statistics at high $p_T$ in the forward region is small.

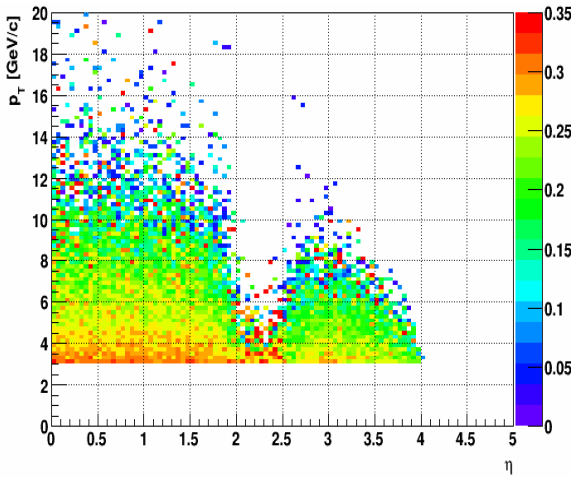


Figure 3-20: Mean distance between matching parton and detector jets. For most jets the mean distance in $\eta-\phi$ space is around 0.2, but depends strongly on the jet $p_{\mathrm{T}}$.

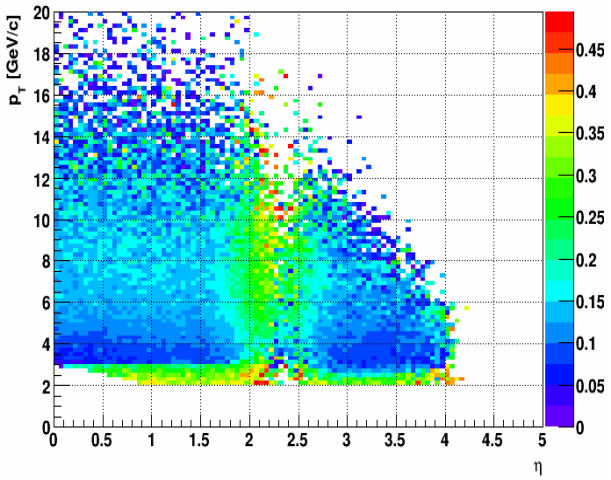


Figure 3-21: Mean distance between detector and particle jets. Detector and particle jets are closer to each other than the detector jets to the parton. The regions of large distance are caused by the lack of coverage between barrel and forward instrumentation and the lower minimum $p_{\mathrm{T}}$ cut for the particle jets.

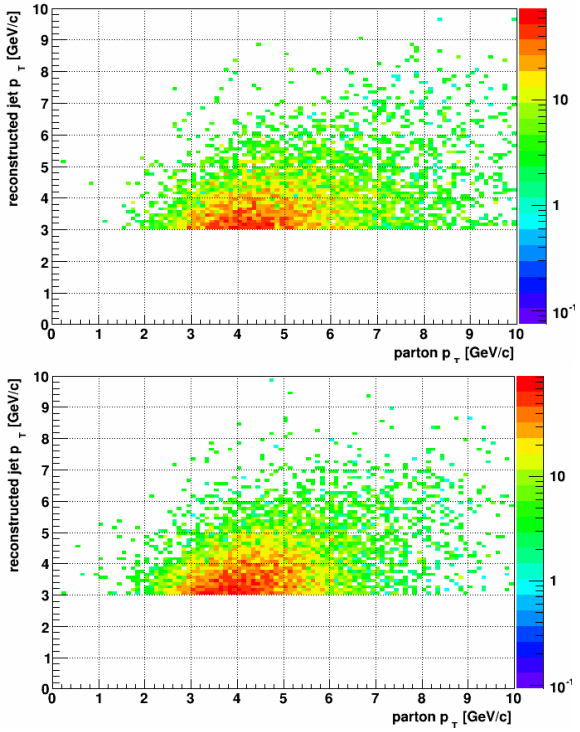


Figure 3-22: Transverse momentum smearing for reconstructed jets compared to that of the associated parton. The upper figure shows the smearing for jets with $2 < \eta < 3$ and the lower figure for those with $3 < \eta < 4$.

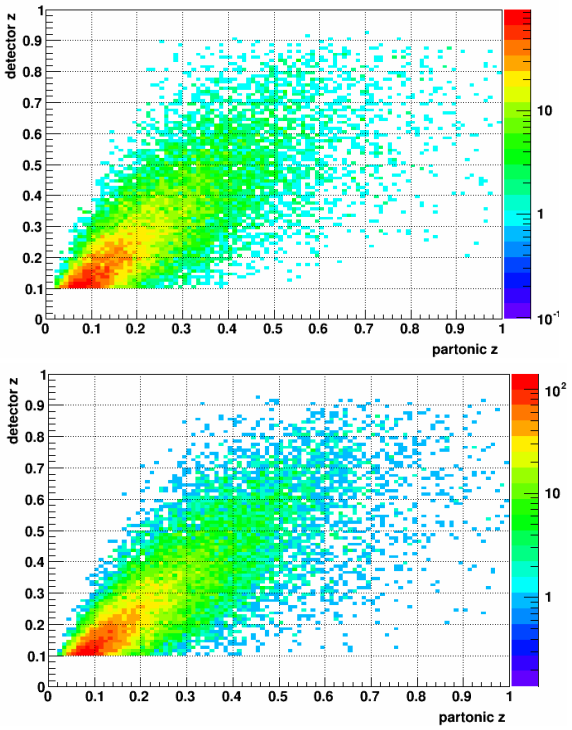


Figure 3-23: Smearing of $z$, the fractional momentum of the outgoing parton/jet carried by the outgoing hadron. The upper figure shows the smearing for jets with $2 < \eta < 3$ and the lower figure for jets with $3 < \eta < 4$.

### 3.4.2 Drell-Yan capability

The formidable challenge of DY measurements is to suppress the overwhelming hadronic background. The total DY cross-section is on the order of $10^{-5} \sim 10^{-6}$ of the hadron production cross-sections, therefore the probability of mis-identifying a hadron track as $e^+/e^-$ has to be suppressed down to the order of 0.1% while maintaining reasonable electron detection efficiencies. To that end we have studied the combined electron/hadron discriminating power of the proposed forward tracking and calorimeter systems. We found that by applying multivariate analysis techniques to the features of EM/hadronic shower development and momentum measurements we can achieve hadron rejection powers of 200 to 2000 for hadrons of 15 GeV to 50 GeV with 80% electron detection efficiency. The hadron rejection power has been parameterized as a function of hadron energy and pseudo-rapidity and has been used in a fast simulation to estimate DY signal-to-background ratios. In the subsection we will describe the procedures of our simulation and discuss some of the results.

We have implemented the exact geometry of the proposed forward calorimeter system in section 2.1 into the STAR simulation framework. With both the EM and hadronic sections as well as the high-granularity of the EMCal we will be able to measure the shower development in both longitudinal and transverse directions. We have simulated the response of the FCS to single electrons and $\pi^-$. To discriminate EM shower against hadronic shower we have used three observables:

1. **Eratio:**
   the ratio of a 5x5 EMCal cluster energy to the sum of the energies of the same 5x5 EMCal cluster and the projected 5x5 HCal cluster.
2. **Swidth:**
   the effective EMCal shower width defined as $R_p = \sum_i r_i E_i^{0.4} / \sum_i E_i^{0.4}$ where $r_i$ is the distance of the $i$th tower to the centroid of a 5x5 EMCal cluster, $E_i$ is the energy of that tower. The summation is over the 25 towers in the 5x5 EMCal cluster around the highest tower.
3. **NTratio:**
   the number of EM towers with energies above 100MeV divided by the total number of EMCal and HCal towers above the same threshold. All the towers come from a pre-defined 5x5 EMCal cluster around the highest tower and the corresponding 5x5 HCal cluster.

Figure 3-24 shows the distribution of these three variables for 30 GeV electrons and $\pi^-$ respectively.

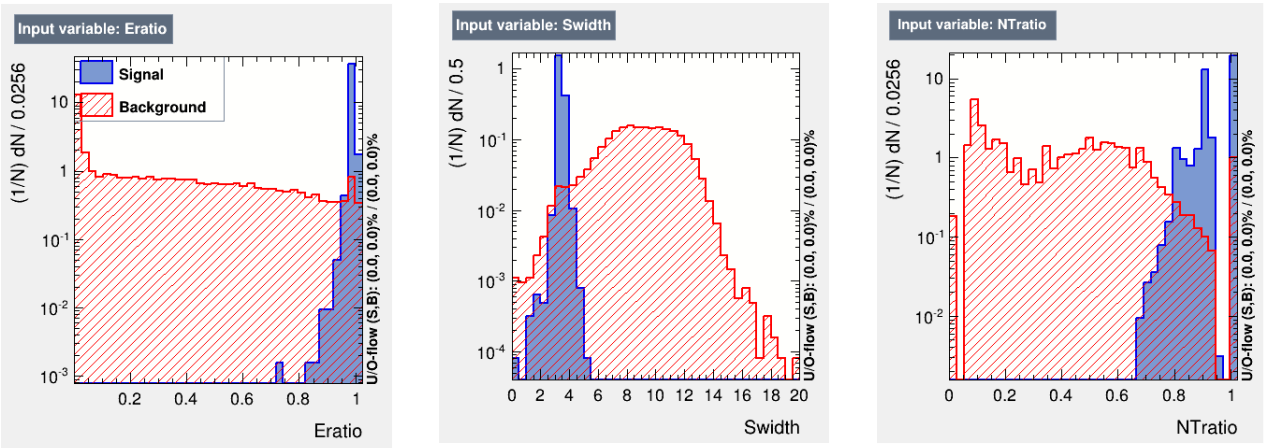


Figure 3-24: Eratio, Swidth & NTratio distribution for 30 GeV electrons (Signal) and $\pi^-$(Background). See text for explanation.

The FTS helps rejecting hadrons by measuring total track momentum. The ratio of energy deposit in EMCal to track momentum (E/P ratio) could serve as an additional information in separating $e^{+/-}$ from charged hadrons. The momentum resolution was evaluated from a standalone simulation of the forward tracking system with typical expected performance for the technology choice and parameterized as a function of energy and pseudo-rapidity. Figure 3-25 shows the parameterized momentum resolution at $\eta = 2.5$ and 4.0. Figure 3-26 shows the energy to momentum ratio, *E/p*, for 30 GeV electrons and $\pi^-$.

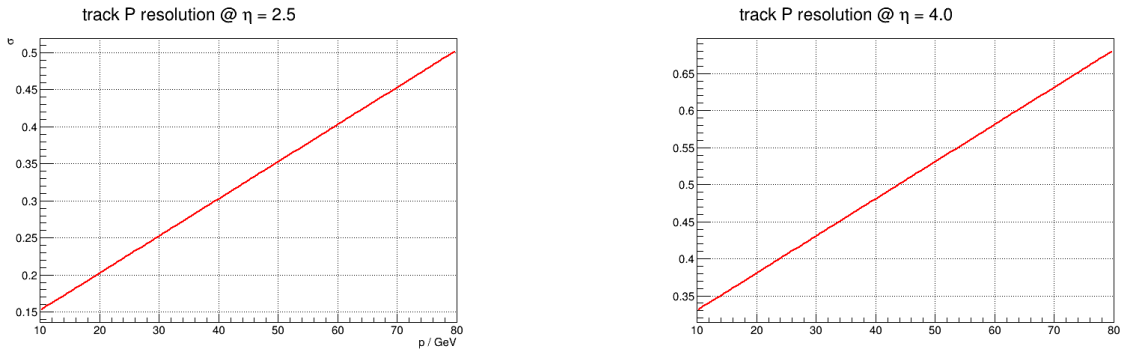


Figure 3-25: expected track momentum resolution of the forward tracking system from simulations.

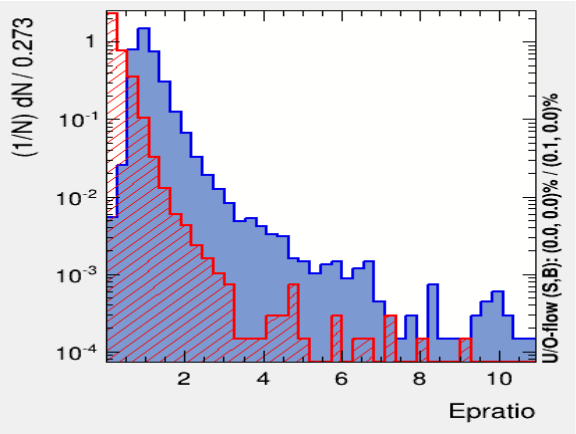


Figure 3-26: *E/p* ratio of 30 GeV electrons (blue) and $\pi^-$ (red)

These observables from the FTS and FCS have been used as inputs to a Boosted Decision Trees (BDT) algorithm. The BDT contains 1000 binary decision trees each has a depth of 4 and corresponds to a particular partition of the 4-dimensional feature space into signal(electron) and background(hadron) regions. They are trained sequentially using half of the electron/ $\pi^-$ samples generated. Mis-identified tracks from the previous decision trees were given a higher weight in training the subsequent trees. In the end each decision tree was given an index representing its performance during the training. In the validation stage the decision of each track identification was made based on the collective response of all of the decision trees, with each of their responses weighted by the performance index. The boosting algorithm takes advantage of using not only the discriminating power of each single observable but also the correlations among them.

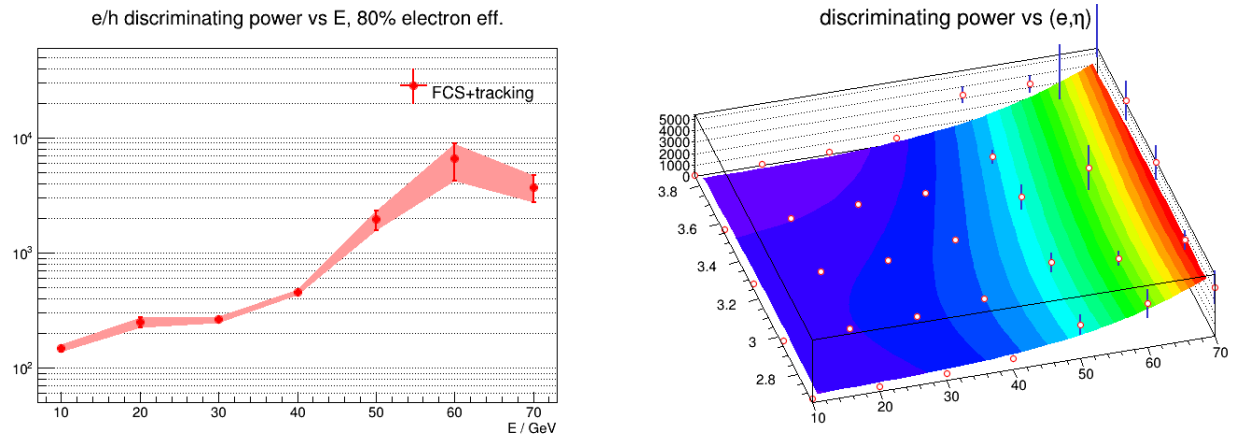


Figure 3-27: e/h discriminating power as a function of the track energy (left panel) and the variation over the pseudo-rapidity (right panel) from combined forward tracking and calorimeter systems

To estimate the DY signal to background ratio the e/h discriminating power has been parameterized as a function of the track energy and the pseudo-rapidity as is shown in Figure 3-27 We have generated 4 billion PYTHIA pp events at 200 GeV with *CKIN(3)* = 3 GeV and a forward filter requiring a total $p_T$> 3 GeV in any of the four jet-patch-like regions in $2.5 < \eta < 4.0$. All basic QCD 2→2 scatterings as well as heavy flavor channels were enabled. As a reference we note that 2.5 pb$^{-1}$ p+Au luminosity is equivalent to 500 pb$^{-1}$ p+p luminosity, which corresponds to 240.5 billion p+p events with the above setting. The DY productions through $q\bar{q}$ annihilation and qg scattering processes were separately generated and scaled to 500 pb$^{-1}$.

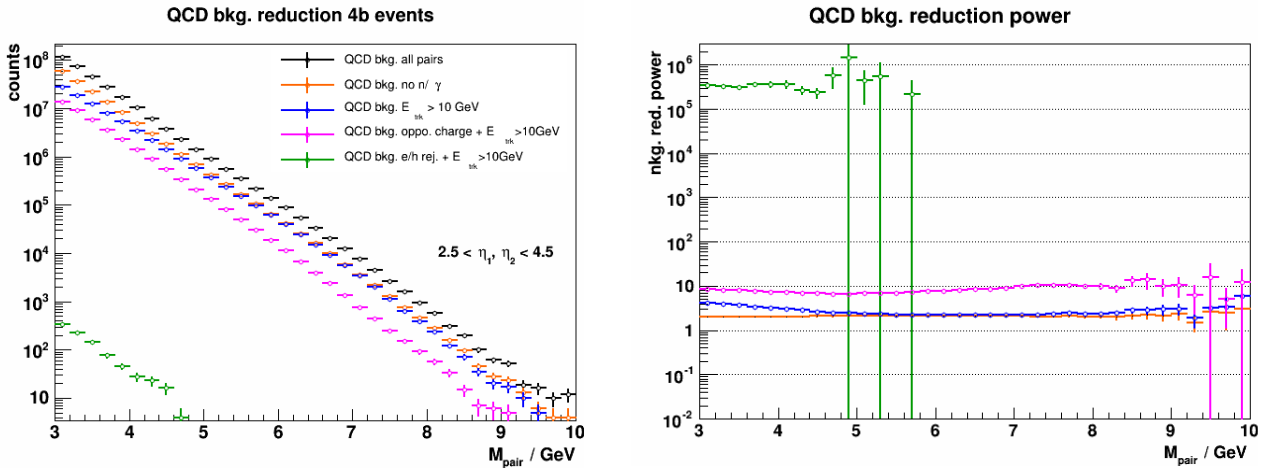


Figure 3-28: QCD background reduction with kinematics cuts and e/h rejections

Figure 3-28 (left panel) shows the yield of track pairs from QCD background sample with the proposed cuts applied accumulatively to illustrate the background reduction process from each step. The final background yields from the 4 billion sample after gamma/neutron removal + track energy cuts + charge sign requirement and e/h discrimination are shown by the green points. The right panel of Figure 3-28 shows the accumulative background reduction factor after each step of applying the cuts.

The final background yields as a function of pair masses were then fit by an exponential function and rescaled to a total luminosity of 500 pb$^{-1}$. The left panel of Figure 3-29 shows the normalized background yield along with the expected DY productions. The green band represents the statistical uncertainties of the background yield and its shape. The right panel shows the DY signal to the QCD background ratio as a function of pair masses.

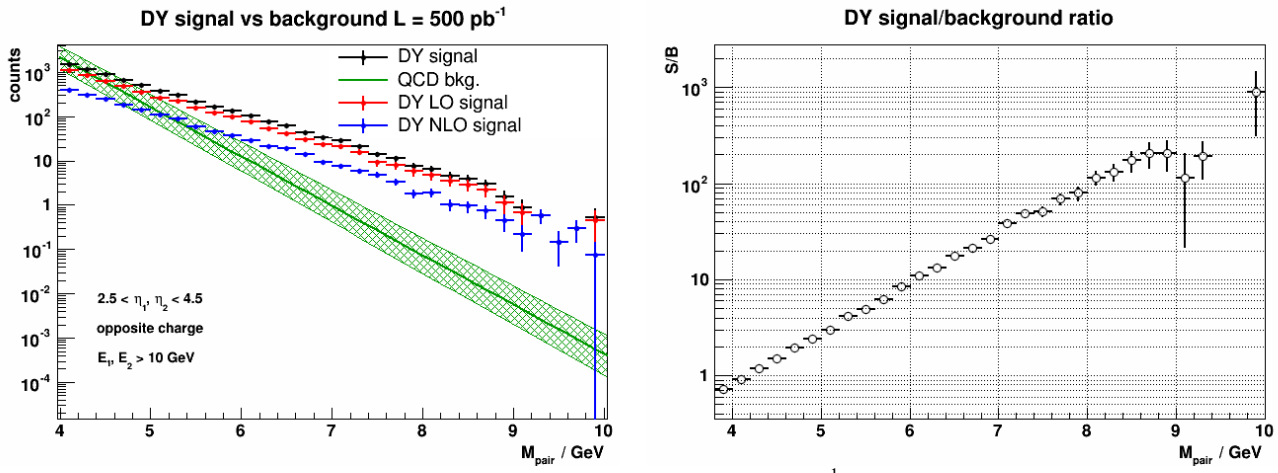


Figure 3-29: DY signal and background yield from 500 $pb^{-1}$ p+p 200 GeV collisions

Finally we note that we have only considered the QCD background in the DY signal/background ratio presented in this subsection. We expected additional backgrounds from photon conversion from materials. Without a detailed design of the beam pipe and the FTS and its supporting structure, we do not have a reliable GEANT model to simulate the photon conversion background yet. Rough estimate indicated that these additional backgrounds may be on the same order for the QCD background if care is taken to minimize the materials in the fiducial acceptance of the forward detectors.

### 3.4.3 Physics observables

Section 2 describes the envisioned science program with the FCS and FTS. Jets are among the experimentally more elaborate probes in this program. The remainder of this section focuses on two of the proposed jet measurements and quantifies the anticipated precision from simulation.

#### *Longitudinal Spin Physics*

The STAR measurement of the double beam-helicity asymmetry in inclusive jet production at mid-rapidity provides the at present best sensitivity to gluon polarization in the polarized proton and shows, for the first time, that gluon polarization is positive and of similar size as the polarization of the quarks and anti-quarks combined. The main limitation, that of quite limited coverage in gluon fractional momenta $x$, can be addressed via measurements with jets at forward rapidity, in particular measurements of di-jets.

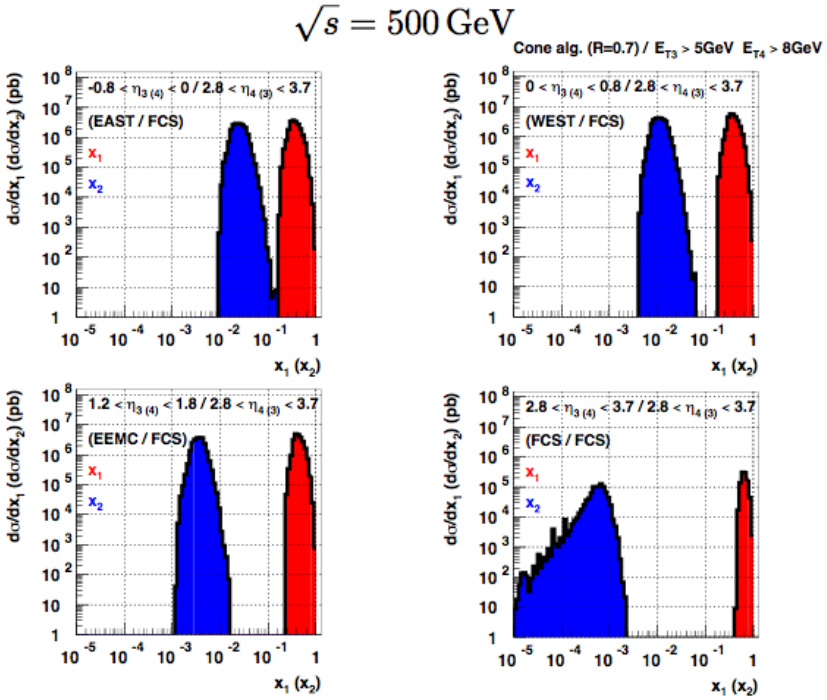


Figure 3-30: $x_1$ / $x_2$ range for the forward STAR acceptance region in $\eta$ of $2.8 < \eta < 3.7$.

Figure 3-30 shows the $x$ coverage for four topological di-jet configurations involving at least the forward system labeled as FCS in combination with either EAST, WEST, EEMC and FCS. It is in particular the EEMC / FCS and FCS / FCS configuration which would allow to probe $x$ values as low as $10^{-3}$ in $x$.

Figure 3-31 shows for the same topological di-jet configurations the actual asymmetries as a function of the invariant mass $M$. The theory curves at NLO level have been evaluated for DSSV and GRSV- STD [116] where DSSV refers also to the first global fit result including data at RHIC in polarized p+p collisions [14]. The systematic uncertainty assumed to be driven by the relative luminosity uncertainty of $\delta R = 5 \cdot 10^{-4}$ is clearly dominating over the size of the statistical uncertainties. Any future measurements in this topological configuration of very forward measurements would clearly benefit from improved relative luminosity control and measurements. This also includes the expected benefit from a fully commissioned spin flipper system at RHIC. However, even with the assumed Run 9 relative luminosity result, a measurement of strong impact can be achieved comparing the $A_{LL}$ curves for DSSV and GRSV-STD evaluated at NLO level. Such measurements would probe for the first time the unexplored kinematic region around $10^{-3}$ in $x$ prior to a future Electron-Ion Collider program. The recent global analysis released by the DSSV group concludes that low-$x$ data are 'badly needed' [14]. A measurement of forward di-jet production would provide such measurements.

Figure 3-32 shows the correlation of the particle and detector di-jet mass based on a fast simulation framework discussed earlier. Good correlation is found for all four topological di-jet configurations. This study assumes only a forward calorimeter system. The impact of a tracking system based on silicon disks would have only a marginal effect on the $p_T$ reconstruction considering the STAR magnetic field configuration. However, a tracking system is expected to improve the actual localization and separation of jets, in particular for the FCS / FCS di-jet topology that gives access to the lowest possible values of Bjorken-$x$. High rate capability and efficiency are essential performance measures in particular for background rejection. The FCS and FTS upgrade is

required for these measurements. Besides di-jet correlation measurements, we anticipate to make measurements of $\pi^0$-jet correlations with a neutral pion reconstructed at forward rapidity as a systematic cross-check [117]. The NLO framework for hadron / hadron jet measurements exists [118].

The proposed forward di-jet production measurements, shown in Figure 3-31, in combination with measurements of the current STAR acceptance region would allow to probe spin phenomena of gluons well below the region of $0.05 < x < 0.2$, which is currently accessible. Such measurements would provide critical initial insight into the nature of the proton spin. The proposed program offers unique and timely opportunities to advance the understanding of gluon polarization in the polarized proton, prior to a future Electron-Ion Collider that with sufficient energy will probe the $x$ dependence of the gluon polarization to well below $10^{-3}$ in $x$ with high precision [119].

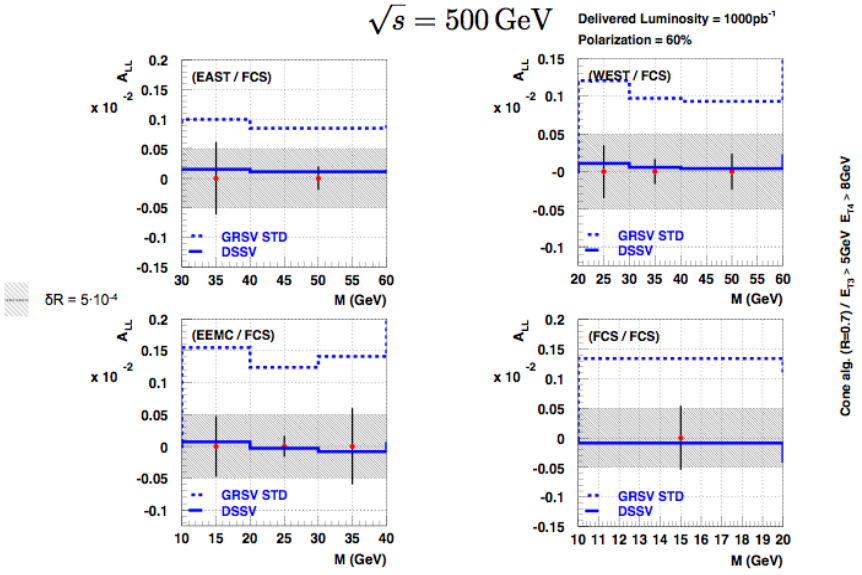


Figure 3-31: $A_{LL}$ (NLO) for the forward STAR acceptance region in $\eta$ of $2.8 < \eta < 3.7$ together with projected statistical and systematic uncertainties,

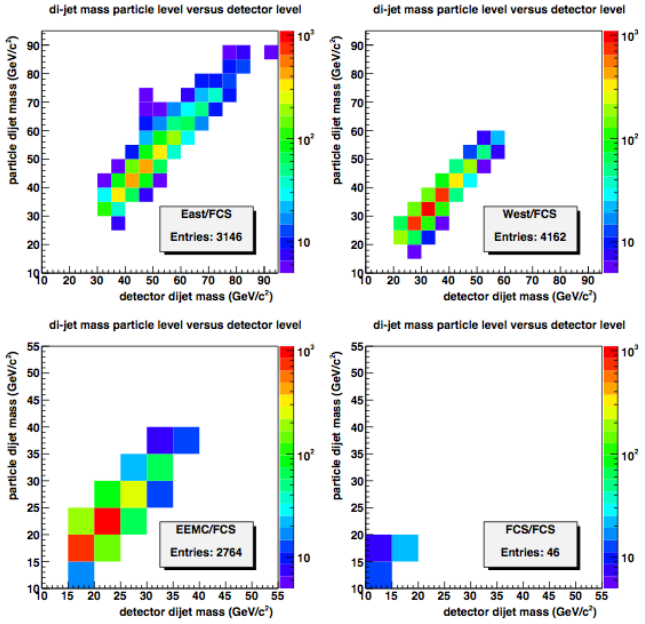


Figure 3-32: Correlation of the particle and detector di-jet mass including effects for the forward STAR acceptance region.

As was discussed in section 2.2.2, the spin-dependent azimuthal distribution of charged particles within jets is sensitive to quark transversity × Collins fragmentation. The asymmetries are known as Collins asymmetries. RHIC measurements are complementary to those that will be made at Jefferson Laboratory with unique sensitivity at forward rapidity. In Figure 3-33 we show the expected Collins asymmetries for $p^{\uparrow} + p \rightarrow jet + \pi^{\pm} + X$ at $2.8 < \eta < 3.7$ and $\sqrt{s} = 500$ GeV. Jets are required to have a minimum $p_T$ of 3 GeV/$c$. The 2008 transversity and Collins fragmentation function parameterization by the Torino group [46] has been inserted into a leading-order PYTHIA simulation using CDF Tune A. Jets are reconstructed utilizing an anti-$k_T$ algorithm, and the asymmetries are calculated relative to the associated hard-scattered parton. The projections assumed 1 fb$^{-1}$ of luminosity with 60% beam polarization. Particle kinematics are reconstructed assuming a fast simulation for detector smearing based on a silicon forward tracking system and electromagnetic and hadronic caolorimetry. Asymmetries of nearly 2% are expected for both flavors of pions. In Figure 3-34 we show a comparison of di-hadron asymmetries at the "detector" level, with the fast simulation detector smearing, to those at the "particle" level, before simulated detector smearing. Based on the simulation, the effects of kinematic smearing to the asymmetries are expected to be quite small. This suggests that within the same subsystem, one can simultaneously measure in a robust fashion the Collins asymmetry within the TMD framework and the di-hadron asymmetry within the collinear framework. These measurements are critical for extending current understanding of transversity and questions concerning TMD evolution, factorization breaking, and universality, as well as longstanding questions about the nature of large inclusive asymmetries seen in p+p collisions.

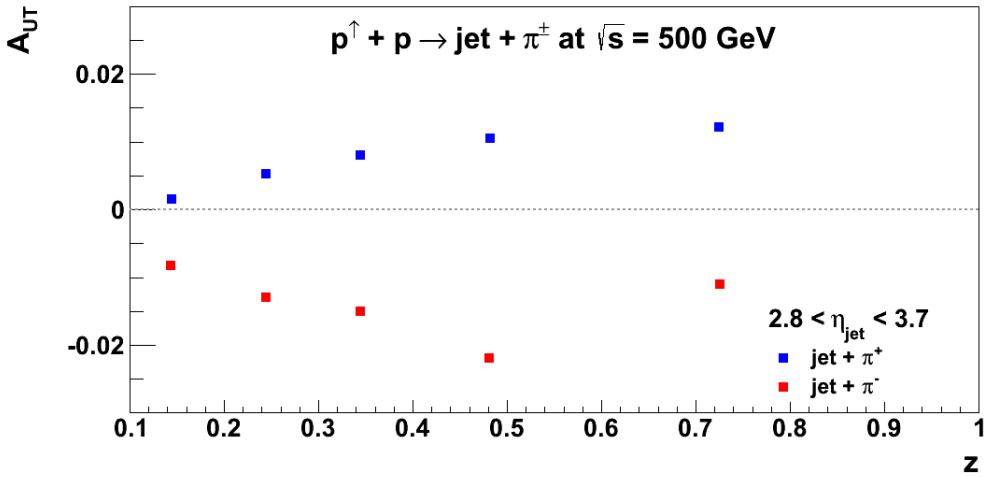


Figure 3-33: Expected Collins asymmetries assuming the Torino parameterization [46] within a leading-order PYTHIA Monte Carlo for charged pions within jets produced with $2.8 < \eta < 3.7$ and $p_T > 3$ GeV/$c$. The expectations assume 1 fb$^{-1}$ of integrated luminosity, and statistical uncertainties are smaller than the size of the points. Jets are reconstructed utilizing an anti-$k_T$ algorithm, and the asymmetries are calculated relative to the axis of the hard scattered parton.

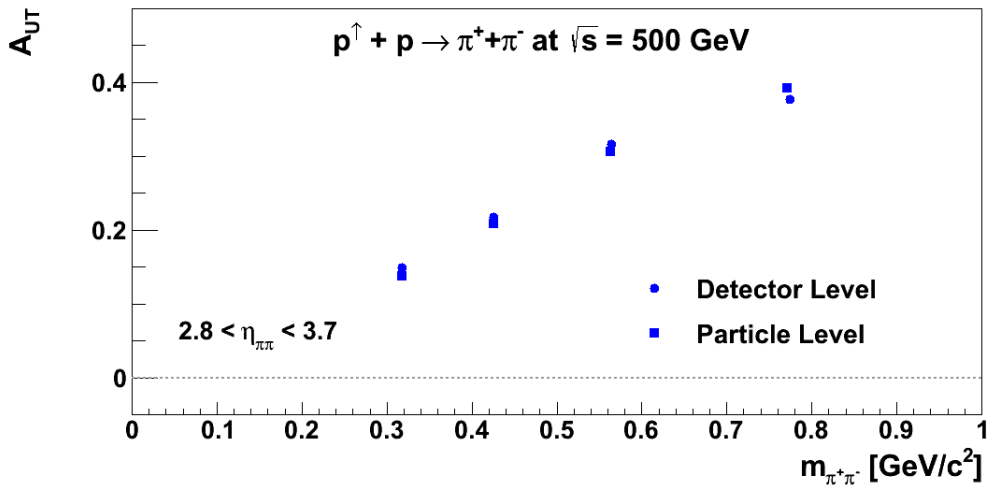


Figure 3-34: Comparison of IFF asymmetries at the "detector" level and at the "particle" level for charged pions produced within $2.8 < \eta < 3.7$. Asymmetries are shown as a function of di-hadron invariant mass, and assuming a parameterization inspired from fragmentation function measurements at Belle [45]. The projections assume 1 $fb^{-1}$ of integrated luminosity, and statistical uncertainties are smaller than the size of the points.

In Figure 3-35 we show the expected Sivers asymmetries [120] for $p^{\uparrow} + p \rightarrow jet + X$ at $2.8 < \eta < 3.7$ and $\sqrt{s} = 500$ GeV. Jets are reconstructed in the same manner as discussed above for the Collins asymmetries, and the Torino parameterization is assumed for the Sivers function [46]. Since the inclusive jet asymmetry provides only a single hard scale, namely, jet $p_T$, the twist-3 framework is most naturally suited for theoretical interpretation. However, the current estimates give a sense for the size of such effects. One can see that for 1 $fb^{-1}$ statistics may be sufficient to observe a nonzero asymmetry. However, the effects are expected to be quite small, at an order less than 1%. The magnitude of this projection is qualitatively similar to existing inclusive jet asymmetries at forward pseudorapidity [121].

Recent theoretical work [122] has found that by taking into account initial-state and final-state interactions between the hard scattered parton and the polarized remnant, extractions of the Sivers function from SIDIS data [40,41] are consistent with existing inclusive jet data from p+p scattering [121]. The extracted Sivers functions were used to derive the twist-3 function $T_{q,F}(x,x)$ [123] that was then used to compute the corresponding inclusive jet asymmetry for p+p scattering. The prediction compares favorable to the measured asymmetry, indicating a process-dependence to the Sivers effect. Due to the small size of the apparent inclusive jet asymmetries more precise measurements are needed.

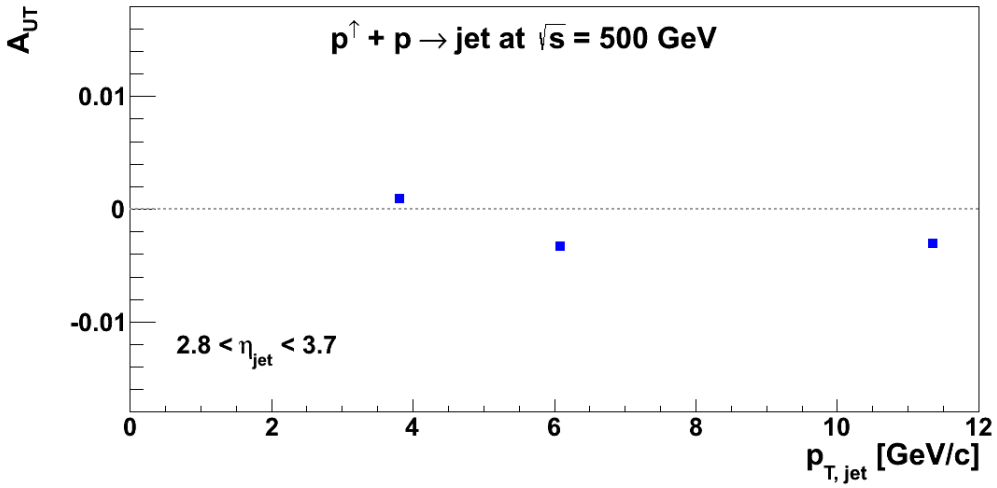


Figure 3-35: Expected Sivers asymmetries based on the Torino parameterization [46] within a leading-order PYTHIA Monte Carlo for jets produced with $2.8 < \eta < 3.7$ and $p_T > 3$ GeV/$c$. The expectations assume 1 fb$^{-1}$ of integrated luminosity, and statistical uncertainties are smaller than the size of the points. Jets are reconstructed utilizing an anti-$k_T$ algorithm, and the asymmetries are calculated relative to the axis of the hard scattered parton.

In addition to the inclusive jet measurements outlined above, di-jet measurement allow further probes of the transverse momentum dependent structure of the nucleon. Here the relative transverse momentum between the jets, $k_T$, gives the additional soft scale needed for the TMD framework. In addition, accessing functions like Sivers [120] and Boer-Mulders [124] in p+p collisions allows one to explore additional asymmetries that may result from the "color-entanglement" in p+p, which also leads to the breakdown of factorization theorems [125].

# 4 The Forward Calorimeter System (FCS)

## 4.1 Introduction

The design of the FCS is driven by detector performance, integration into the STAR system and cost optimization. The FCS combines the strength of the ZEUS calorimeter [126], with its excellent hadronic energy resolution and the H1 calorimeter[127], with its excellent electromagnetic energy resolution; arguably both of these are among the best sampling calorimeter systems operated in the past. The proposed system has very good electromagnetic and hadronic energy resolutions. It is probably the most compact calorimeter system (for given energy resolution) tested to date. It can operate within a magnetic field and in a fairly high radiation environment. By design the system is scalable and easily re-configurable.

The design of the FCS' is a follow up development of the original proposed FCS system and is driven by detector performance, integration into STAR and cost optimization. The big reduction in the cost for the FCS' is achieved by replacing the originally proposed W/ScFi SPACAL ECal with the refurbished PHENIX sampling ECal. In addition, the FSC' will utilize the existing Forward Preshower Detector ($2.5 < \eta < 4$) operated in STAR since 2015. The proposed FCS' system will have very good (~ 8%$\sqrt{}$ (E)) electromagnetic and (~ 70%/$\sqrt{}$ (E)) hadronic energy resolutions. FCS' consists of 2000 of the 15552 existing PHENIX EMCal towers and 480 HCal towers covering an area of approximately 3 m × 2 m. The hadronic calorimeter is a sandwich lead scintillator plate sampling type, based on the extensive STAR Forward Upgrade and EIC Calorimeter Consortium R&Ds. Both calorimeters will share the same cost effective readout electronics and APDs as photo-sensors. It can operate without shielding in a magnetic field and in a high radiation environment. By design the system is scalable and easily re-configurable. Integration into STAR will require minimal modification of existing infrastructure.

A new method of construction for compensated hadronic calorimeters was developed during the STAR R&D program. A calorimeter system similar to the FCS is considered as a baseline design in the outgoing hadron region of a dedicated EIC detector.

## 4.2 Choice of Technology

There are several factors which lead us to adopt the technology choice for the proposed FCS. The electromagnetic energy resolution at the level of about 10%/$\sqrt{}$ (E) and hadronic energy resolution at level of about 55%/sqrt(E) are sufficient to carry out proposed measurements outlined in previous chapters. The same levels of energy resolution are desired for a future EIC detector as was carefully studied in[5]. For comparison, the best hadronic energy resolution of 44%/$\sqrt{}$ (E) was achieved by the ZEUS collaboration in their compensated uranium sampling calorimeter. Calorimeters in ATLAS and CMS at LHC have hadronic energy resolution > 100%/$\sqrt{}$ (E). Hadronic energy resolution at the level of 55%/$\sqrt{}$ (E) requires a compensated calorimeter system. Compensation, in turn, requires relatively low sampling fraction. In case of lead as an absorber material, the sampling fraction needs to be kept below 2.4%.

The forward calorimeter system has to be very compact for the STAR forward upgrade. This is required by the configuration of the STAR IP and existing STAR detector. The whole calorimeter system should be about one meter deep to fit into the STAR IP. Obviously, the small sampling fraction required for compensation is also required for compactness. However, small sampling

fractions in both EM and HAD sections and required compactness are challenging for traditional readout schemes. A readout scheme similar to one used for ZEUS or H1, mentioned above, will not work for two reasons. They are not compact and both used PMTs as photo-detectors. In the past, fiber calorimeters, for example, very often had a readout structure which was longer than the absorber/scintillator structure as a requirement for uniform light collection. In addition, fringe magnetic fields at STAR and the future EIC detector will prohibit use of PMTs as photo-detectors. We chose SiPMs as photo-detectors for both the EM and HAD sections of the FCS. The choice of SiPM technology will be explained in detail later.

The FCS has to be designed so that the hadronic calorimeter can be assembled in place. The access at the FCS location is limited, with no overhead crane available. Thus it will be preferable to have the whole detector assembled from relatively light parts *in situ*, preferably by undergraduate and graduate students, who can provide important man power resources in the STAR collaboration.

## 4.3 Hadronic Section -- Technology and Design

The design of the sampling structure of the HCal section is modeled after the ZEUS Pb/Sc compensated prototype, which was the first compensated calorimeter. The HCal section mechanically is a stack of layers of absorber and scintillation plates. The easiest way to describe the assembly process is to imagine building an entire HCal block from LEGO style parts layer-by-layer. The basic mechanical structure of the HCal mechanical prototype is shown in Figure 4-1.

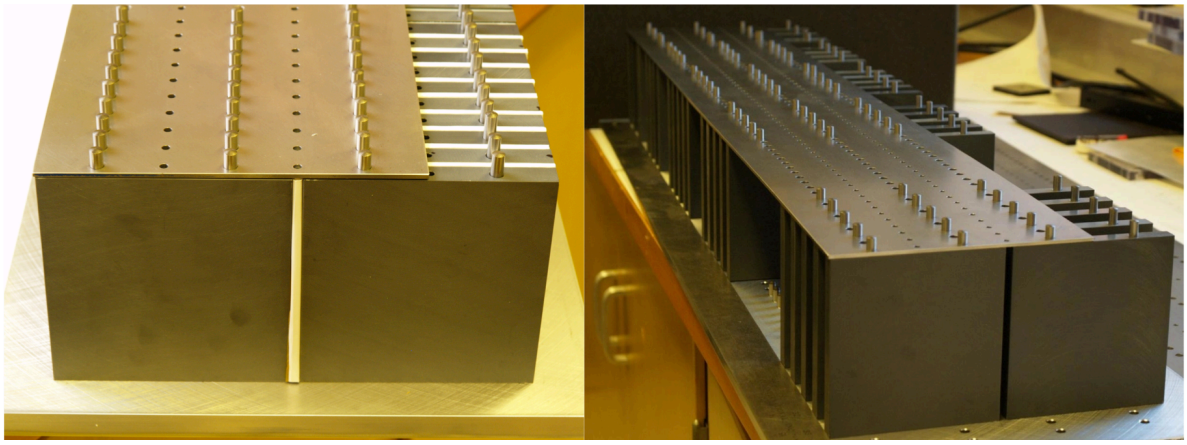

Figure 4-1. LEGO type HCal mechanical structure. Absorber plates (gray in color) positioned with the aid of dowel pins. Scintillation and WLS plates (white in color) inserted in between absorber plates. Steel master plates works as a links between adjacent rows and front and back plates of the calorimeter.

Holes in the bottom base plate of the detector provide locations of the absorber plates. Each absorber plate has four holes for dowel pins, two at the bottom and two at the top. Steel dowel pins (5 mm in diameter) position absorber plates with respect to the bottom base and top steel master plates. A single master plate covers one and a half rows of HAD towers, providing interlinks: between all absorber plates within one tower, between front and back steel plates of the HAD section and between adjacent rows of the HAD towers. The thickness of the absorber plates is 10 mm. They are made of lead-antimony alloy (4% Sb) and painted with white diffusive reflective paint (Sherwin Williams F63WC134). The gap between two adjacent absorber plates is 3.1 mm. Scintillation plates of thickness 2.5 mm (EJ-212) are placed inside these gaps. There are 63 absorber plates and 64 scintillation plates in a single HCal tower. Scintillation light from a single tower is collected with a 3 mm thick wavelength shifting (WLS) plate (EJ-280), which is placed in the gap between the two adjacent HCal towers. All scintillation and WLS plates are “floating” within each

layer (there are no mechanical loads on these elements). Figure 4-2 shows an assembled HCal prototype. We assembled this prototype in place at the FNAL test beam to validate the construction technique. It took about eight hours for four people to build the sixteen-channel HCal prototype from the individual components at the test beam site.

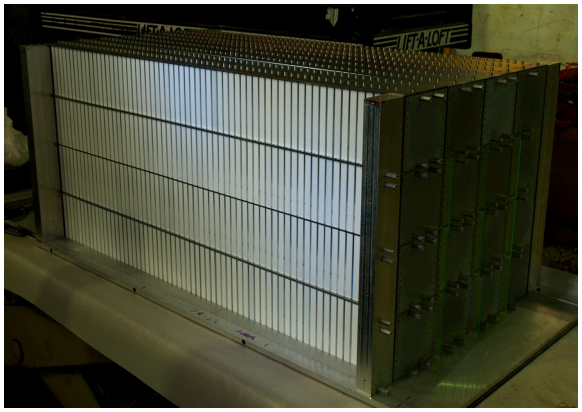

Figure 4-2. A full scale HCal prototype during assembly at FNAL test run in 2014. The prototype consisted of sixteen individual towers. It was assembled from individual parts directly at the test beam site.

The light collection scheme of the HCal was optimized to provide uniform and efficient light collection from all scintillation tiles along the depth of the HCal tower. All optical connections (except for coupling of the silicon photo-multipliers to the WLS) in the HCal were made through a thin air gap. We found that the good combination of reflective materials for the WLS plate is white diffusive reflector (Bicron BC-620) at the far end (from the photo-detector) and aluminized mylar at the back side (opposite to the edge of the scintillation tiles) of the WLS. The mylar film also serves as an optical isolator between HCal towers within one layer of the HCal. To achieve uniform light collection (within 10%) along the depth of the HCal tower, we placed a variable density filter printed on a clear mylar sheet inserted between scintillation tiles and the WLS plate. MC calculations show that without such a filter, the energy resolution of the HCal degrades by about factor of two for the energy range above 20 GeV compared to an ideal detector. Variation of light from tile-to-tile in the tower within 10% has negligible effect on energy resolution. Bench test measurements show that variation of the thin air gap between the scintillation tiles and WLS plate (due to mechanical tolerances required for HCal assembly) has a negligible effect on energy resolution of the detector as well. We found no degradation in light collection efficiency for unwrapped scintillation tiles placed between painted absorber plates compared to that for scintillation tiles wrapped with Tyvek.

## 4.4 Photo-sensors and Front-End Electronics

We have developed a new compact readout for the FCS. For both the EMCal and HCal sections we decided to use silicon photo-multipliers (Hamamatsu Multi-Pixel Photon Counters (MPPC) S10931-025p used in FANL test Run in 2014). They are very compact, fast and insensitive to magnetic fields and sufficiently radiation hard for FCS readout in STAR [128]. SiPMs do not require HV for operation, which can significantly simplify the readout system. The cost of SiPMs continues to drop, while performance of these devices is becoming better and better for all manufacturers. Two other important considerations in choosing a photo-detector include the speed of light collection and the nuclear counting effect (NCE). These two considerations effectively preclude the usage of APDs as readout sensors for FCS. Anomalous APD signals due to NCE[129] would be impossible to suppress for a fiber calorimeters without doubling of the number of readout channels. The methods that the CMS collaboration developed to treat such signals in a PWO based calorimeter will not work for fiber calorimeters due to the much shorter light collection time. SiPMs

are immune to NCE.

The measured light yield (with a very efficient light collection scheme and PMTs) from the EMCal prototype in the first test run in 2012 was approximately 2000 p.e./GeV. We estimated that with 4 MPPC per tower for the EMCal section and with 8 MPPC per tower for the HCal section we will collect enough light to keep the contribution from photo-statistics to the energy resolution of the detector at a negligibly small level. The geometrical efficiency (ratio of active area of eight MPPCs to the output surface area of the WLS plate) of the light collection scheme for HCal is 8.2% and ~21% for EMCal towers. A light collection scheme with WLS plates for HCal towers provides perfect light mixing. The situation is different for the EMCal section where light from the scintillation fibers is collected by the MPPC through a short (25 mm long) light guide/mixer. A bench test measurement prior to the test run showed that with this scheme, non-uniformity of the light collection might be as high as 20% (difference between the hottest spots just under the MPPCs and at the corners of the towers). We decided to proceed with this scheme anyway to measure the absolute light yield with readout based on MPPCs and later redesign the light collection scheme for the EMCal section depending on results of the test run. The optical, mechanical and electrical integration of the readouts for the EMCal and HCal sections are given below.

We used two different sets of front end electronics to readout the FCS with the MPPC during the test run. The front end electronics for the HCal section is shown in Figure 4-4-3 and Figure 4-4. The HCAL front end board is designed for low power and reliable, low cost integration into a large detector system. The unregulated 90VDC input is regulated to the required SiPM bias voltage set by two DAC channels, one incorporating a thermistor. In this way, both the voltage and temperature compensation slope (to maintain a constant gain of the SiPM) are programmable. Signals from four SiPM's are directly summed at the input of a single preamplifier, which is a regulated common-base stage using BFR92A transistors. The amplifier input impedance is very low, a few Ohms; as a result the high capacitance (1.3nF) of the four parallel SiPM's does not limit the charge collection time as it would with a 50 Ohm input. The preamplifier is followed by a differential output driver providing a 4 V peak-to-peak signal to be used with low cost, low mass twisted pair cables to an external ADC system. The large signal swing and differential interface ensure satisfactory performance with a robust high dynamic range even when there is an external EMI or ground noise in the system. The read-out scheme for the HCal will be further optimized in the coming months when we work towards the final electronics design.

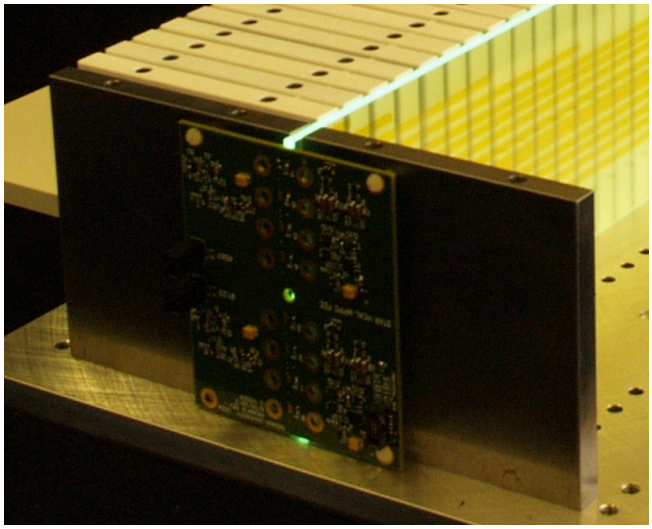

Figure 4-4-3: HAD FEE attached to WLS plate during bench tests.

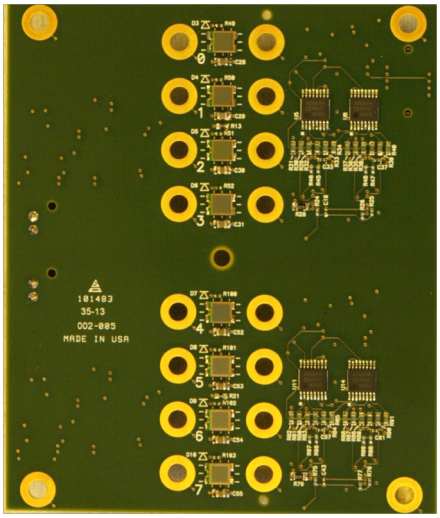


Figure 4-4: HAD FEE Board with 8 SiPMs installed.

For readout of the EMCal towers, four SiPMs per tower were grouped through pre-selection based on lab testing of the SiPMs (shown in Figure 4-4-5) so that all of them had almost equal responses at the same bias voltage. A single bias voltage was used for all sixteen towers. A simple resistive divider was used to set the required bias voltage for individual towers. There was no temperature compensation of the bias voltage for the EM prototype. Analog signals from these MPPCs were summed with the OPA691 operational amplifier. MPPC sensors for the EMCal prototype were first mounted on the FEE board, calibrated, and then potted with Dow Corning Sylgard 184 silicone. This silicone layer (~ 2 mm thick) served as an optical cookie and as a spring to keep the FEE board firmly attached to the light guide with a single plastic screw (visible at the center of the light guide).

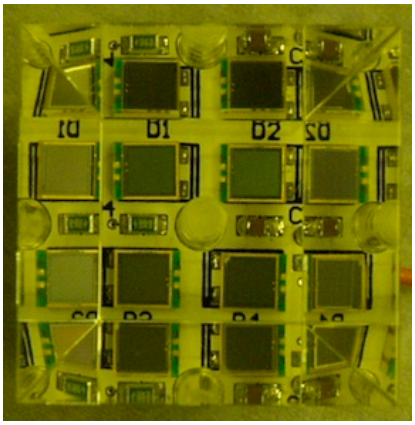

Figure 4-4-5: View from the backside of the short light guide similar to one used in the EMCal prototypes with the attached FEE board. Light from each EMCal tower was collected by four SiPMs located next to the mounting screw in the center of the light guide. The other twelve images of SiPMs are reflections from the sides of the light guide.

The design of the light guide was not completely optimized prior to the test run. The light guide is an acrylic truncated pyramid with a height of 25 mm, base 25 mm x 25 mm and 13 mm x 13 mm at top. The distance between the centers of the MPPCs is 7 mm. Geometrical efficiency of the light collection scheme for the EMCal is approximately 21%.

## 4.5 Performance of the FCS in the Test Run at FNAL in 2014

We tested the response of the FCS prototype with hadrons, electrons and muons in the energy range 3-32 GeV at Fermi Lab. Electrons were identified with a differential Cherenkov counter (standard equipment at the MTBF). Impact position was defined by a scintillator XY hodoscope (4.9 mm wide scintillator square rods with readout by SENSL SiPMTs). We minimized the amount of material upstream of the calorimeters in the beam line to about 4 cm of scintillation counters. Additionally, MTBF personnel installed He- filled beam pipes between our apparatus and the upstream Cherenkov counter. The initial setup of our apparatus in the beam line is shown in Figure 4-6. Two MTBF MWPCs (one is seen in Figure 4-6) were used as additional monitoring devices during the beam energy scans to track reproducibility of the beam settings at different energies. The HCal was oriented with a fixed angle (2.5 degrees) between the beam and the primary axis of the HCal towers. The EMCal prototype was attached to the front steel plate of the HCal. The angle between the axis of EMCal towers and beam was kept at 4 degrees. All channels of the FCS were equipped with an LED monitoring system. Events for LED monitoring signals and pedestals were continuously recorded at a rate about 1 Hz most of the time during the test run. Preliminary analysis of these data showed that stability of the gain for HCal and EMCal front end electronics was better than 1% during a typical twelve hour shift of data-taking. All SiPM's were tested and

calibrated with a laser system prior to the test run. With this system we measured that the response of the MPPC assemblies for both HCal and EMCal prototypes were set equal to within 1%. We found that no additional tower-by-tower calibration of the EMCal prototype with the beam was required. This was expected based on our previous beam test results in 2012 when we measured excellent internal homogeneity for the EMCal modules built with our construction technique.

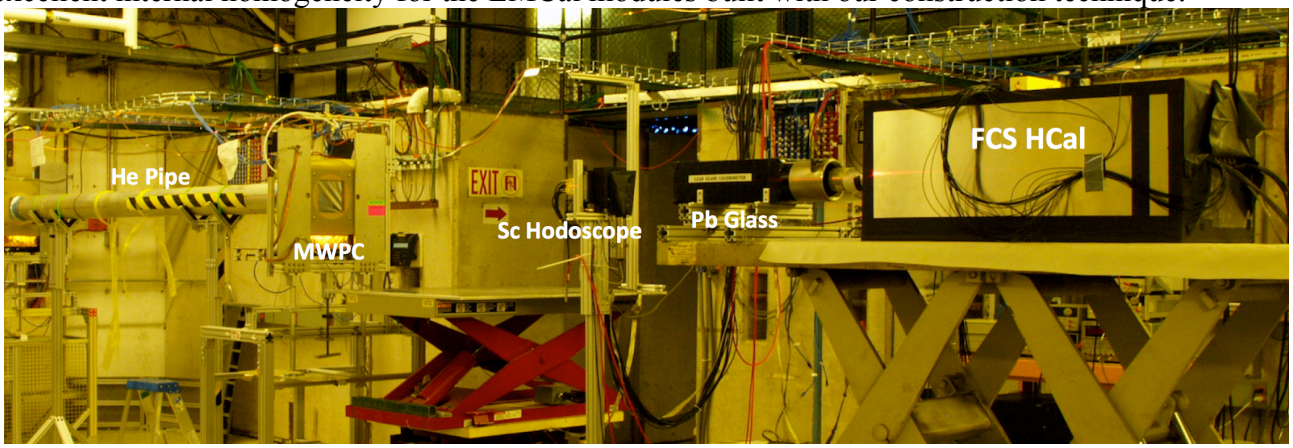


Figure 4-6: FCS prototype at the beam line. Pb glass calorimeter in front of HCal was used for initial beam studies.

The HCal required additional tower-by-tower calibrations with MIPs. For that an absorber was inserted into the beam line (8 GeV muon mode for the MT6 test line). A MIP peak was selected in each HCal tower using an isolation requirement (a single muon hit in a tower with no other energy deposition in the rest of the HCal). For calibrations with MIPs the EMCal prototype was removed from the beam line. We found that quite large corrections at the level of approximately 20% were needed in addition to the calibrations made prior to the test run. About 10% of this shift can be explained by the alignment of the WLS plate and the MPPCs (both have a 3 mm active area, about 250 microns misalignment is possible due to positioning of the MPPCs on the FEE board). The rest can be attributed to the quality of optical components: one possible source is the variations in the response of the WLS tiles used in different HCal towers (concentration of dopants and attenuation length have not been measured for every WLS tile used in the HCal, and we assumed that they are all identical).

The response of the FCS prototype module to hadrons is illustrated in Figure 4-7. In an ideal, completely compensated calorimeter detector, the reconstructed energy of the incoming hadron is a simple sum of the energy deposited in the EMCal and HCal sections (assuming that the responses in both sections are equalized and energy independent). To obtain the best energy resolution for hadrons in the FCS prototype module we found that a weighting factor for the EMCal section should be energy dependent. The factor changes from about 2 to 1.2 for beam energies ranging from 3 to 20 GeV and stays approximately flat above 20 GeV. With this energy dependent weighting of the EMCal energy, we measured the e/h ratio for the FCS prototype module to be close to 0.95 and almost constant above 10 GeV.

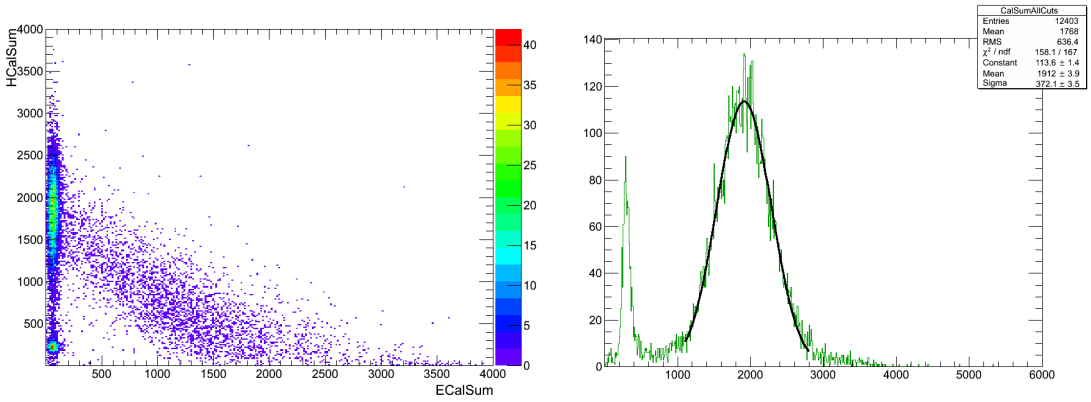


Figure 4-7. Response of the FCS prototype module to hadrons. Energy deposition in HCal section (Y-axis) vs energy deposition in EMCal section (X-axis) for 12 GeV hadrons (left panel). A weighted sum of the energy deposited in EMCal and HCal section for 12 GeV hadrons (right panel).

We did not perform any corrections due to leakages in the transverse and longitudinal directions in the FCS prototype module. Qualitatively, this result is close to MC predictions, however in our MC model we did not include some of the structural elements between the EMCal and HCal sections as well as the limited size of the prototype tested at FNAL. The questions of optimal weighting factor and the final expected e/h ratio in the FCS prototype module will need to be clarified with a MC model of the exact geometry of the detector that was used in the test run.

The response of the FCS prototype module to electrons is illustrated in Figure 4-8. Due to non-uniform light collection with MPPCs the response of the EMCal section depends on the impact position. We corrected the energy deposition in the EMCal section according to impact position and restricted the impact area only to the circle with a diameter of 1.4 cm at the center of the EMCal tower.

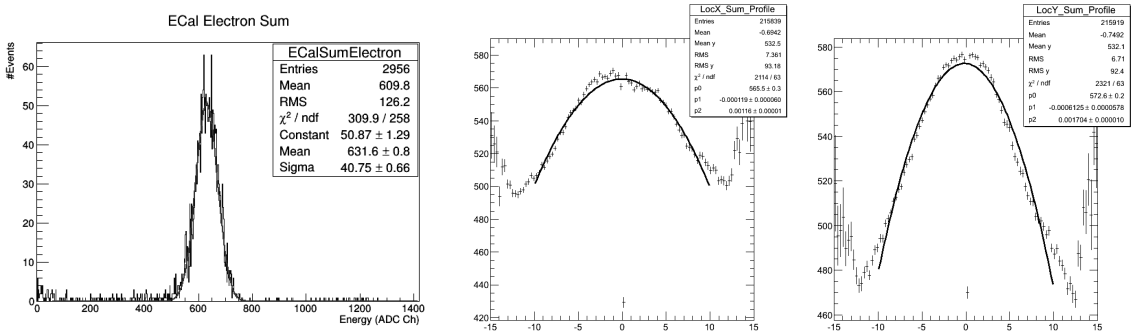


Figure 4-8. Response of FCS EMCal prototype module to electrons. Energy deposition in the EMCal section for 4 GeV electrons, with the impact point restricted by the scintillation hodoscope to an area 5 mm x 5 mm (left panel). Dependences of energy deposited in EMCal section are shown as a function of impact positions in local X coordinate (center panel) and local Y coordinate (right panel).

Local coordinates of the impact positions were determined using calorimeter information only. We used a logarithmic weighting method with the cut-off parameter set at 3.8. The difference in the shapes of the responses of the EMCal section in the X and Y directions is due to a tilt of the EMCal prototype of 4 degrees around the Y axis.

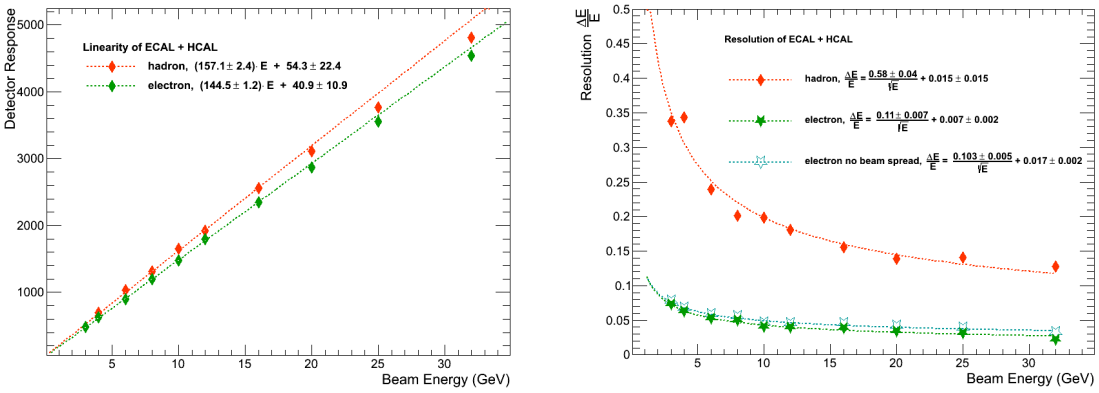


Figure 4-9 Responses of the FCS prototype module to electrons and hadrons versus energy (left). Energy resolution of the FCS prototype module for hadrons and electrons versus energy (right).

The performances of the FCS prototype module during the beam test in 2014 are summarized in Figure 4-9. The responses to electrons are approximately linear, while the responses to hadrons show clear deviations from linearity above 15 GeV. The most likely reasons for this deviation are the weighting procedure of the fraction of energy deposited in the EMCal section and leakages from the FCS prototype module. We tested the HCal section alone (with EMCal section removed from the beam line) and did not observe a similar deviation from linearity in this energy range. The energy resolution of the FCS prototype module for hadrons, shown in Figure 4-9, is about 15% worse compared to MC predictions for the FCS module at 10 GeV. One of the reasons is likely the transverse leakage from the FCS prototype module, which was not taken into account for the test beam results. We also note that the energy resolution of the FCS in the MC simulation depends on the physics list used in GEANT4. We used a LHEP physics list, which, in our studies, provides the most accurate description of the FCS performance. The electromagnetic energy resolution of the FCS prototype module is close to MC predictions. There are two fits to our experimental results shown in Figure 4-9. One assumed that the momentum spread of the beam is

zero. In this case the stochastic term is close to 10% and the constant term is 1.7%. If we use our earlier (2012) estimates for the momentum spread of the beam to be 2.7 % below 4 GeV and 2.3% above 4 GeV, then the stochastic term becomes 11% and constant term is close to zero.

The absolute light yield measured in the EMCal section is about 400 pixels/GeV, with the front face of the EMCal prototype painted with the white diffusive paint BC-620. The measured absolute light yield for the HCal section is about 130 pixels/GeV. MPPCs for both EMCal and HCal sections should behave almost linearly with these amounts of light yields for the energy range used in the test run. The light yield measured for the EMCal prototype is sufficient so that we can introduce a mask between the scintillation fibers and the light guide to improve the light collection uniformity in future. Given the fact that the most recent generation of MPPCs already have much better PDE compared to the MPPCs used in the test run (and anticipated future improvements in SiPMs), we believe that there is no need for any type of reflectors at the end of the scintillation fibers. This will significantly simplify the construction of the EMCal section. According to our measurements in 2012, with EMCal prototypes equipped with a good mirror versus with a black tape at the end of the fibers, all degradation in the energy resolution can be explained by photo-statistics alone, *i.e.*, degradation due to light attenuation length in the scintillation fibers is not critical in this case.

## 4.6 Summary of Technology Development for FCS.

We have developed a new construction technique for a high-resolution lead scintillation tile hadronic calorimeter. The FCS system with EMCal and HCal sections was designed specifically for the STAR forward upgrade. The performance of the FCS system from the test run data met our expectations. The novel compact readout scheme based on SiPM readout works well for the HCal prototype. For the EMCal section, improvements in the uniformity of light collection have to be made in the near future. With the amount of light yield measured at the test run, introduction of properly designed masks between scintillation fibers and light guides should solve the non-uniformity issue in the light collection.

## 4.7 Mechanical Integration into STAR

The FCS in STAR will be located at the space presently occupied by the FMS. Mechanical integration will require reinforcement of the existing FMS platform. We had preliminary discussions with the engineers involved in the design of this platform. There is no problem to reinforce the existing FMS platform. We performed preliminary FEA calculations of seismic loads and long-term stability of the FCS at BNL location. These calculations were carried out by a mechanical engineer at UCLA and need to be reviewed and certified by project mechanical engineer. There were no problems found in preliminary analysis of seismic stability and long term creeps of the FCS structure (for absorber plates made of Pb/Ca alloy, for the test run prototype we used Pb/Sb from cost considerations).

## 4.8 FCS Electronics Overview

FCS electronics includes trigger, readout of SiPMs, low-voltage system for SiPMs, low voltage power, slow control functions, calibration and monitoring controls, and interfaces to the STAR trigger, DAQ and slow controls. The bulk of the front-end electronics functionality, including signal processing, digitization, buffering, formation of trigger primitives will be carried out by STAR QT boards. The existing STAR FMS readout system based on QTs can be completely

reused for the HCAL section, requiring about 30% of the FMS electronics. The rest of FMS electronics will be used for the EMCal section. Additional QT boards will need to be produced to complete the readout of the EMCal section.

The slow controls for the FCS, probably, will be duplicated from the STAR Forward Preshower Detector (FPD) being constructed for run 2015. The FPD is using modified front-end electronics which was developed for the hadronic section of the FCS. Information about performance of the FPD electronics and operation experience of the FPD during 2015 and 2016 will guide the final design of the FCS slow control system.

The front end electronics developed for HAD section during R&D will need minor modifications for interfacing with the QTs; again, some refinement of this part will probably come from the operational experience of the FPD. Advances in SiPMs technology by the time of finalization of the FCS electronics may also require additional changes in HCAL and EMCal FEE designs.

The front end electronics for the EMCal section will require additional R&D efforts. The overly simplified version of the electronics used for the test run in 2014 will be revisited. It will be required to have similar functionality for SiPMs controls and preamplifier that we developed for the HCal electronics. The density of channels for the EMCal section is much higher than that for the HCal section. At present we envision that a single FEE board will be used for readout and control of SiPMs from four EM towers corresponding to a single EMCal super-block. All SiPMs will require the same bias voltage and temperature compensation. We confirmed with Hamamatsu that we can order gain-matched SiPMs for that. A single light source (LED mounted on FEE board) will be used to monitor stability of sixteen SiPMs.

In the last test run both EMCal and HCal sections used monitoring system with optical fibers to distribute light to individual towers. For HCal section this scheme will work well in the final detector configuration. However, for the EMCal section such implementation is not practical due to the high density of readout channels. At present we envision two different monitoring/calibration schemes for EMCal and HCal sections of the FCS.

## 4.9 Production Plan

The design of the HAD section of the FCS has relied on existing standard technological processes to produce components of the detector in industry. For the full scale prototype, all components were produced in a way that we envisioned for the final detector with the exception for the scintillation tiles. In the prototype detector we used scintillation tiles produced by Eljen (the tiles were cut to the desired size and were polished at UCLA). For the scintillation tiles to be used for the proposed FCS we plan to use an injection molding technique to produce these tiles, similar to the construction techniques used for the ATLAS and LHCb calorimeters. The same technique is planned for the proposed sPHENIX HCAL. One possibility is to use existing capabilities at IHEP (Protvino, Russsia) which is a member institution of the STAR collaboration. The other is to work with the same company that sPHENIX is working with at present for their HCAL. The design of the HCAL tiles is straightforward and any technical risk to produce them is very low. University groups involved in this project will carry out QA for HCAL components, tests and calibration of the FEEs and SiPMs. The project team will perform the final assembly of the detector in place at BNL with help from the STAR technical support group. The STAR technical support group will be responsible for modification of the existing FMS platform.

## 4.10 Additional R&D

Additional R&D will be required to solve the problem of non-uniformity in light collection for the EMCal section with a compact readout based on SiPMs. We have already made the necessary measurements in the lab at UCLA with the EMCal prototype module that was tested at FNAL. The design of the new light collection scheme with an appropriate filter between the fibers and SiPMs is in progress. We plan to test a re-built EMCal prototype at FNAL in 2015.

The development of the EMCal front end electronics with an integrated monitoring system will continue. We would like to accomplish this task during the CD1 stage.

Long term tests of the EMCal modules under pressure will need to be performed. We have performed preliminary measurements of mechanical properties of the EMCal modules, investigated different epoxies to glue the back plate to the EMCal modules (including thermal stress test in a limited temperature range). These tests need to be completed and be certified by a mechanical engineer.

The study of effects of radiation damage on SiPMs will be continued. This R&D program is currently being carried out by the BNL group of the EIC calorimeter consortium. Additional insight will be gained during operation of the FPD at STAR in 2015-2016. FPD is located at the proposed FCS location and will be read out by SiPMs.

In 2014 we reported measurements of thermal neutron fluxes at different locations in the STAR experimental hall during RHIC Run 13 with proton–proton collisions at $\sqrt{s}$ = 510 GeV. We compared these measurements to calculations based on PYTHIA as a minimum bias event generator, detailed GEANT3 simulation of the STAR detector and experimental hall, and with GCALOR as the neutron transport code. A fairly good agreement (factor of two) was found between simulation and measurements[10]. Thus we demonstrated that it is possible to do reliable estimation of the neutron fluxes in the STAR detector.

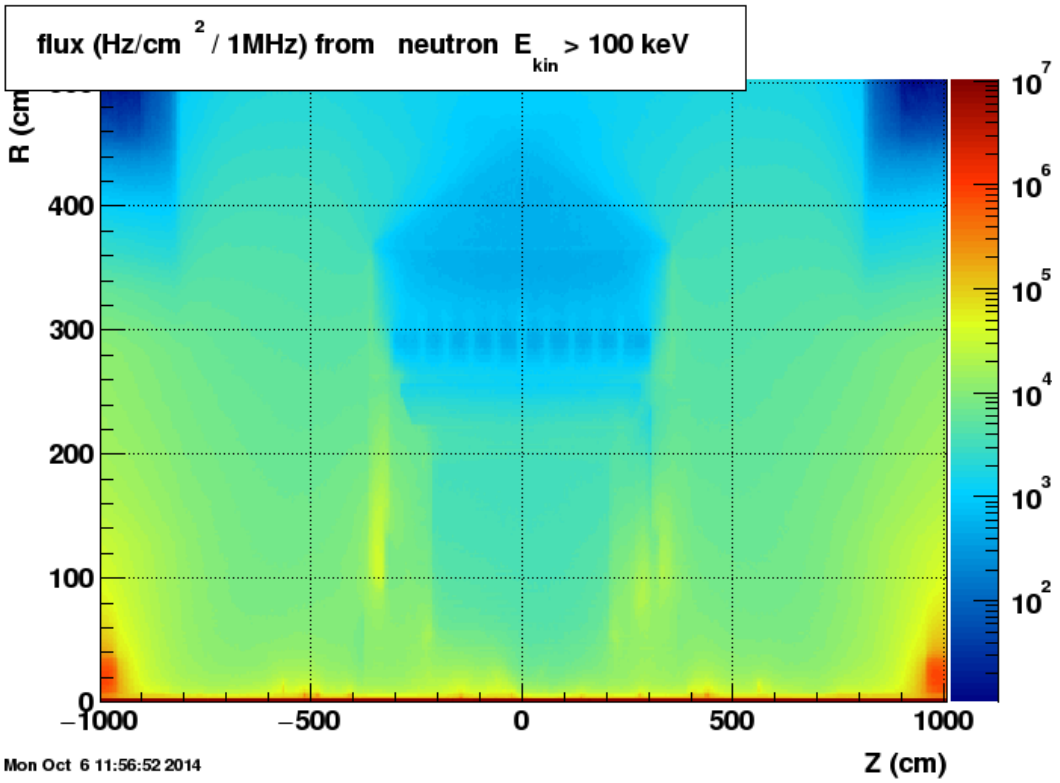


Figure 4-10 A normalized neutron flux in the STAR experiment during Au-Au Run 14 .

As an example, MC generated neutron fluxes at STAR for Run 14 Au-Au configuration are shown in Figure 4-10, they were normalized to 1 MHz minimum bias collisions rate. An integrated

during 93 days of running in 2014 flux of neutrons with $E_{kin} > 100$ keV at location of the FCS according to this simulations are 3.4 x $10^9$ and 5.1 x $10^9$ n/cm$^2$ at pseudo rapidity 2.5 and 4 respectively. Many different groups (CMS, GLUEX, CALICE etc.) reported some degradation in performance of SiPMs at this level of irradiation. In our view, the consequences radiation exposure in terms of using these devices for calorimeter readout not yet fully understood. An EIC calorimeter consortium curried series of tests in the past year to quantify effects of radiation damages on SiPMs. For that sensors were irradiated at BNL and LANCE Facility (Los Alamos) up to 7 x $10^{10}$ n/cm$^2$. With irradiations up to $10^9$ n/cm$^2$ apart from loss in a single pixel resolution, increased dark and leakage currents response of the SiPMs to the light pulses expected in our calorimeters stays about the same. With higher doses of irradiations some losses in photon detection efficiency and as a consequence changes in the response to different levels of light were observed. The degradation effects measured by CMS collaboration were shown Figure 4-11.

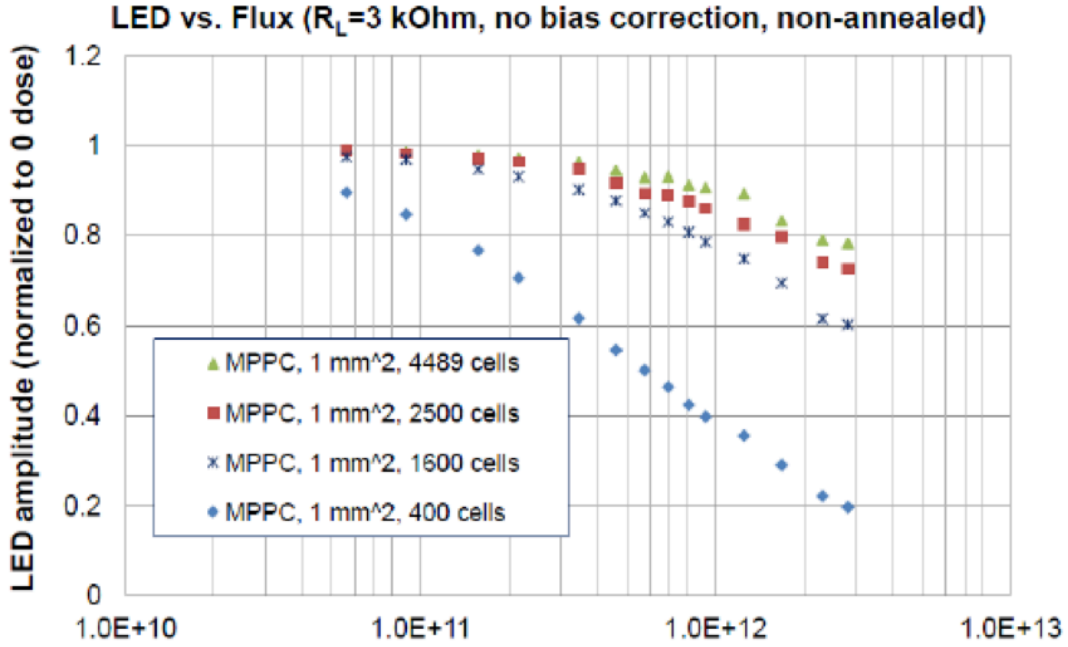


Figure 4-11 Degradation of performance of different SiPMs vs irradiation n/cm$^2$.

A very good understanding of degradation effects is necessary for proper design of the front end electronics and monitoring schemes and integration of the readout electronics with the detector. One possible option is replacement of sensors on most affected areas of the calorimeters every year. The current optical and mechanical integration of the readout allows doing that. That was demonstrated in the latest test run at FNAL when two different prototypes of the EM calorimeters were sequentially successfully tested with the same sets of readout boards.

We plan to carry out at least one additional beam test run with a full-scale preproduction prototype. It is possible that calibration test run with the final readout electronics will be required as well.

# 5 The Forward Tracking System (FTS)

## 5.1 Overview

The physics case for the STAR forward FCS and FTS upgrade is described in section 2 of this document. For transverse spin asymmetry measurements of charged pions in the forward direction in p+p and p+A collisions, it is necessary to distinguish positively charged pions from negatively charged ones with momentum up to 80 GeV/c. For Drell-Yan and $J/\psi$ (direct photon and photon+jets) measurements in the forward direction, excellent electron (photon) identification capability is demanded to suppress large hadron background by 3-4 orders of magnitude. Adding a Forward Tracking System (FTS) becomes essential to achieve such goals. The FTS can separate particles with different charge signs, based on the different bending directions in the 0.5 Tesla STAR Solenoid magnet field. The FTS can improve electron identification by measuring charged particle momenta and comparing with their energy depositions in the FCS. The FTS can also aid photon identification by vetoing on hits from charged particles. In order to achieve these, the FTS needs to have good position resolution and low material budget.

## 5.2 Proposed Configurations

STAR is currently looking into a detector technology, based on silicon-strip sensors, to build the FTS. Design considerations for the FTS are discussed below.

## 5.3 Support Structure

The STAR collaboration has successfully designed and installed a WEST support cylinder (WSC) with an internal support mechanism for GEM disks as part of the existing STAR Forward Gem Tracker (FGT). Figure 5-1 shows a photograph of the WSC (left) along with a photograph of the inside of the WSC showing a FGT-type disk supported in the horizontal direction by carbon fiber rail using rail supports allowing to slide each disk on the actual rail. This is an important feature for installation and extraction and will be discussed in more detail below including the need for an in-situ installation. The forward tracking upgrade options discussed here will re-use this lightweight support system.

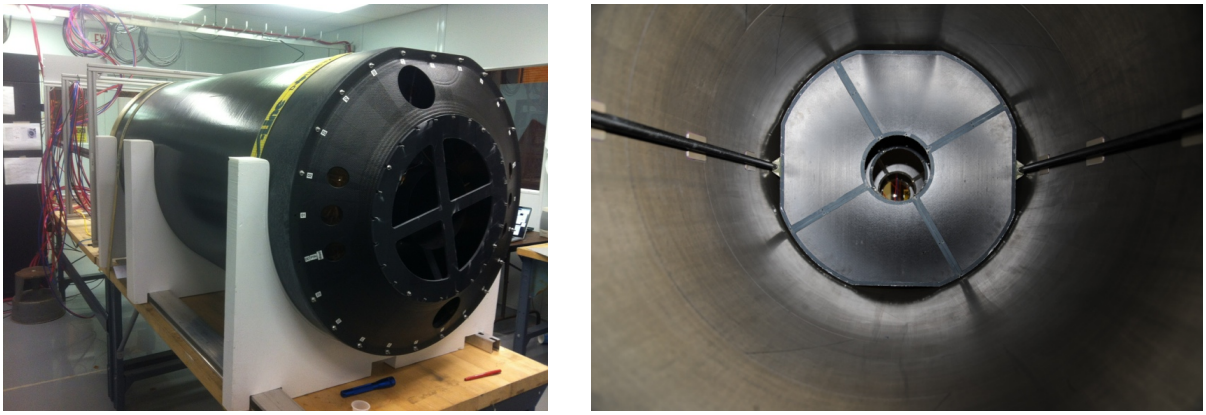

Figure 5-1: Photographs of the WSC prior to installation (left) and (right) of the inside of the WSC with two carbon rails suppring one FGT disk.

## 5.4 Silicon-Based FTS Option

Silicon detectors have been widely used in high-energy physics experiments. STAR has recently built a Silicon micro-vertex detector, the Heavy Flavor Tracker (HFT), to study heavy flavor production at mid-rapidity ($|\eta|<1$) in high-energy nuclear collisions. The HFT includes 3 sub-systems, the Silicon Pixel detector (PXL) made of Monolithic Active Pixel Sensors (MAPS), the Intermediate Silicon Tracker (IST) made of single-sided double-metal Silicon Ministrip sensors, and the Silicon Strip Detector (SSD) made of double-sided Silicon Strip sensors.

In order to achieve good charge separation and momentum resolution, the silicon sensors for the FTS need to have precise position resolution in the azimuthal direction (c.f. section 3.3.2). The requirement on the resolution in the radial direction is not very demanding. As it is mandatory to keep the ghost hit rate and occupancy under control, especially in the A+A collisions, it is proposed to use single-sided double-metal Silicon Ministrip sensors with fine granularity in $\phi$ and coarse granularity in r. These sensors will be read out from their edges at larger radii, so that the frontend readout chips, cooling pipes and liquid can be placed outside of the $2.5 \leq \eta \leq 4$ region to minimize the amount of materials in the FTS acceptance.

A FTS using Silicon Ministrip sensors can take advantage of the successful experience of the STAR IST detector. The latter has good S/N ratio (25:1), high hit efficiency (~99%), and small readout dead time (4%@1kHz with potential improvement). The FTS would consist of three or more planes of Silicon sensors facing perpendicularly to the beam axis. In order to have the longest level arm for momentum measurements, the nearest (farthest) FTS plane to the center of STAR will be placed at Z~70 (140-180) cm. These locations are constrained by the requirement to have $\eta$ coverage between 2.5 and 4, and by the outer (inner) radius of the beam pipe (Carbon fiber cone to support the HFT). As shown below, such a design can provide optimal charge-sign separation and momentum resolution in p+p and p+A collisions, with minimal materials (0.4-0.6% $X_0$) in the acceptance. We estimate that the average occupancy in the Silion-based FTS option is 3.2 (10) % at $\eta$ = 4 (2.5) in the 0-3% most central Au+Au collisions at $\sqrt{s_{NN}}$ = 200 GeV. This estimate is based on the charged particle multiplicities measured with the PHOBOS experiment[130], taking into account that the number of primary tracks is 50-60% of the total number of tracks.

### 5.4.1 Silicon Ministrip Sensors

The abovementioned FTS design uses single-sided double-metal Silicon Ministrip sensors, in which a second Al layer is needed to bring the signals from inner radii to the outer radius edge of the sensors. Silicon sensors will have It is important to perform R&D studies to validate and optimize the sensor design. STAR has started an R&D project to look into it. Shown in Figure 5-2 are sensor masks currently under development. Shown in Figure 5-3 are finite element simulation results for the sensor electrical properties and its response to charged particles passing through. It is expected that prototype Silicon Ministrip sensors will be produced and fully tested by Spring 2017, so that a full design of the FTS may be available.

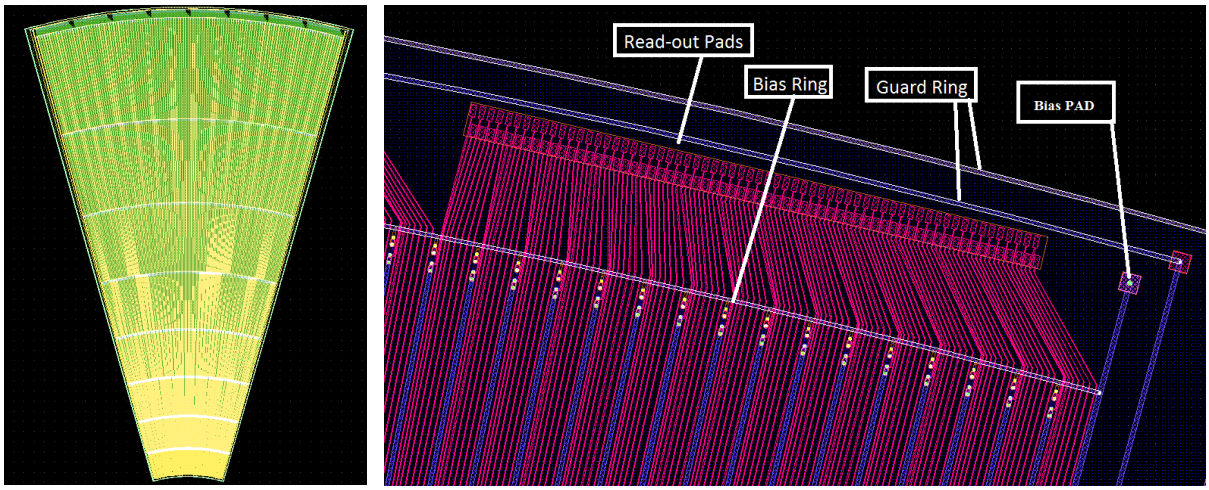

Figure 5-2: (Left) Full view of a FTS Silicon sensor mask. (Right) Zoomed-in view of the sensor mask.

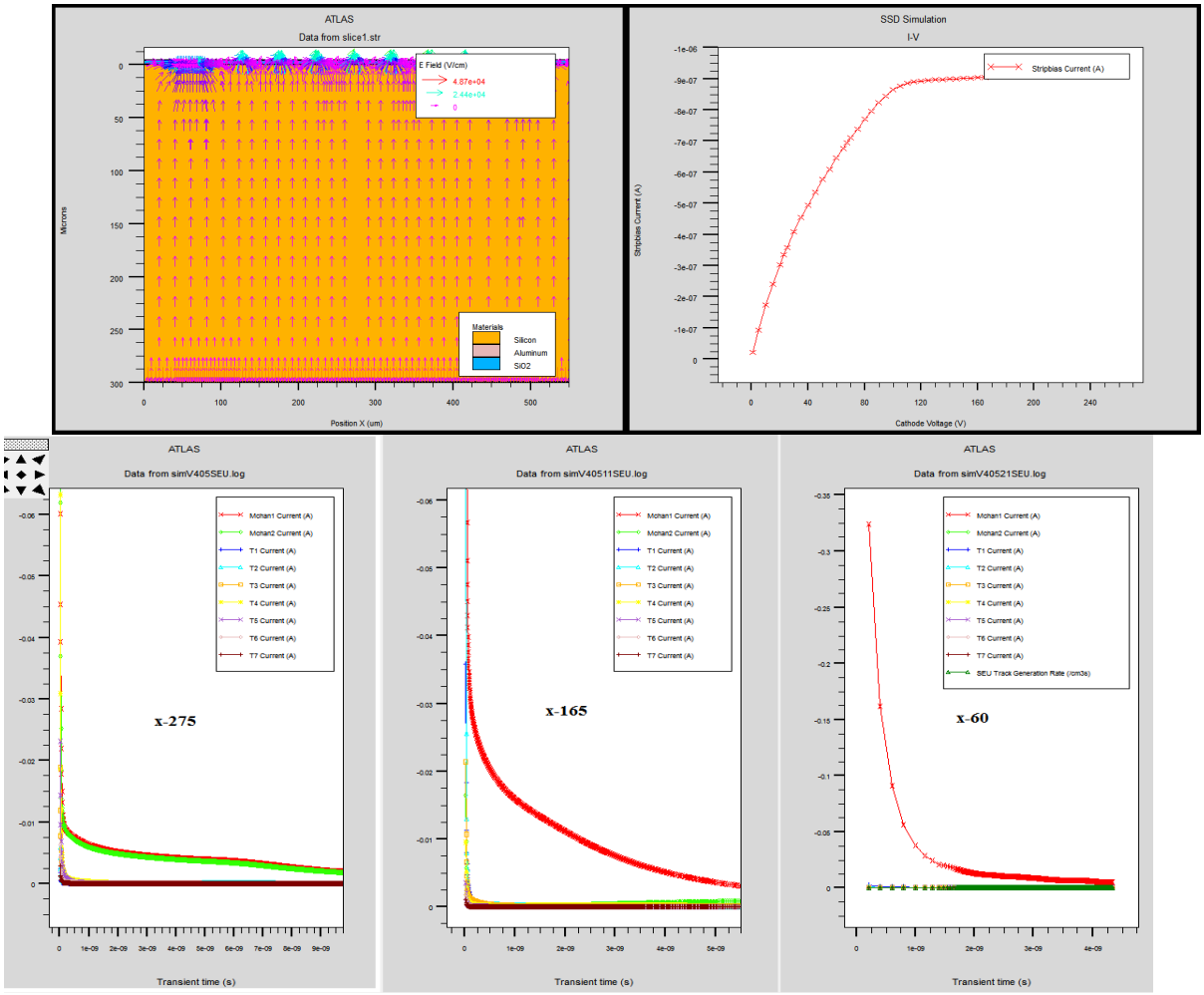


Figure 5-3 Finite element simulation results of a FTS Silicon Ministrip sensor. Top-left: electrical field lines in the sensor cross-section view. Top-right: sensor leakage current vs bias voltage. Bottom: transient electrical signals from the top layer Al strips when a charged particle hit in the middle of (left), at one quarter of the distance between (middle), or on top of one of the (right) two azimuthally neighboring Silicon P+ implant strips. The red and green curves correspond to the top layer Al strips on top of the Silicon P+ implant strips, while the others are the top layer Al strips to bring signals from smaller radius P+ implant strips to the sensor outer radius edge.

### 5.4.2 Frontend Readout Chips

Different frontend chips are available to read out Silicon Ministrip sensors. The APV25-S1 chip has been used in the IST. It has 128 channels each with a charge sensitive pre-amplifier, shaper, and 4 μs long pipeline (see Figure 5-4). Events are read into the pipeline at 40MHz. Events in the pipeline are selected by triggers and marked for readout. A single differential pair per chip reads out each of the 128 channels in series for a selected event. The APV25-S1 chip can also be used to read out FTS sensors, in which case the same DAQ system as that of the IST can be used to minimize electronics engineering work. While a final decision has not been made on this, a sufficient amount of APV chips has been obtained to keep such an option viable.

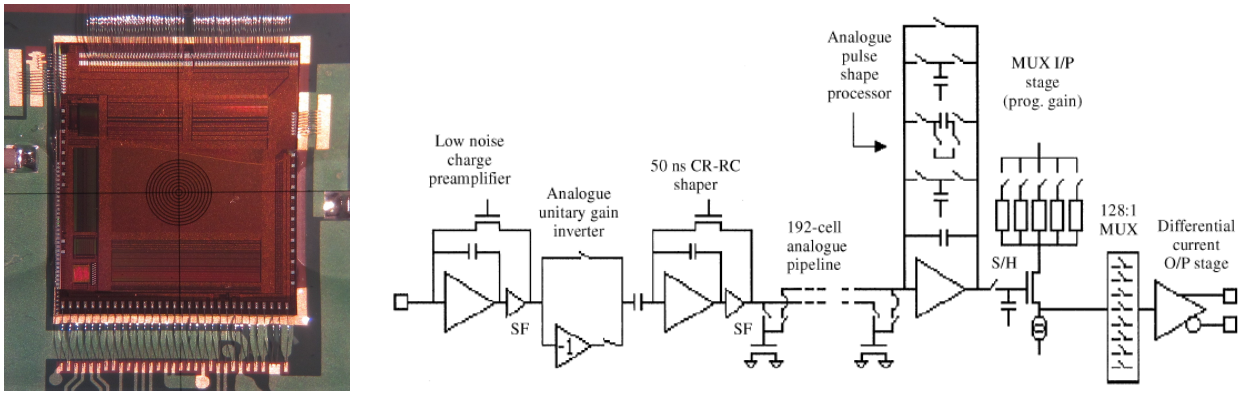


Figure 5-4: Left: Picture of an APV25-S1 chip. Right: block diagram of one channel of the APV25.

### 5.4.3 FTS Wedge

A complete design for the FTS wedge has not been worked out. However, based on previous experience, it can be imagined that a FTS wedge will be made of low mass materials such as Carbon fiber or Beryllium as supporting structures, with Silicon Ministrip sensors and frontend readout chips mounted on a thin flexible printed circuit hybrid. The Silicon sensors will be wire-bonded to frontend readout chips at larger radius edge (see Figure 5-5). Cooling pipes will run beneath the readout chips to keep the chips and sensors at low temperature. Compared to the configuration of reading out from the sensor edges along the radial direction, the material budget in the FTS acceptance will be much smaller (0.4−0.6% $X_0$) since the frontend readout chips, power and signal buses and cooling lines will be located outside of the detector acceptance.

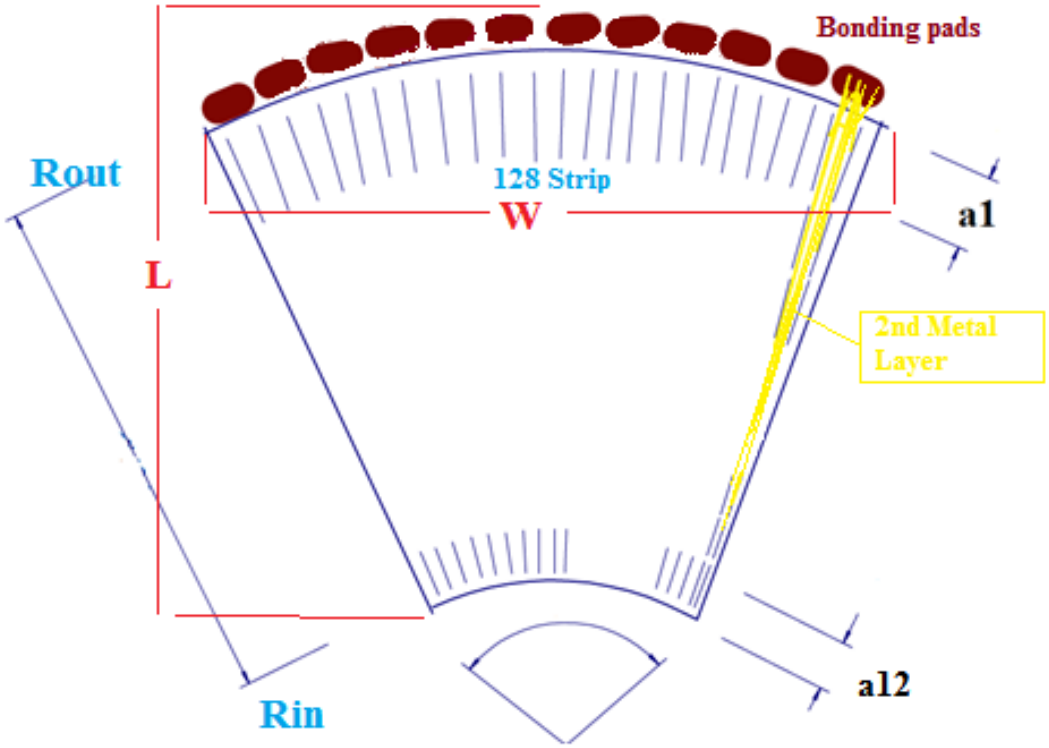


Figure 5-5: Schematic view of a FTS wedge. A Silicon Ministrip sensor with 128*12 strips and 12 frontend readout chips are shown.

### 5.4.4 DAQ System

If STAR decides to use APV chips to read out the Silicon-based FTS, the DAQ system used for the IST can be used for the FTS. The DAQ system has a modular design, which is based on a passive compact PCI backplane running a custom protocol, connecting 6 readout modules to a readout controller module. The readout modules provide all necessary functions, including isolated power supplies, to operate up to 24 APV25 chips per module with high-impedance ground isolation. The frontend boards contain a minimal set of components as they are located inside the STAR TPC inner field cage and are inaccessible except during long shutdown periods. The frontend boards connect to the readout modules with cables up to 24 m in length, carrying unbuffered analog readout signals from the APV25 as well as power, trigger, clock and control. The readout module digitizes the APV analog samples to 12-bits at 37.532 MHz, and buffers the data. The readout controller distributes trigger and clock from the central trigger system, gathers the data over the backplane, and ships it to a linux PC via a 2.125 Gbps optical data link (Detector Data Link (DDL) from ALICE). The PC gathers data from multiple readout controllers and dispatches it to the STAR event builders. The readout modules, controllers, and backplanes are housed in a common crate together with the Silicon sensor HV bias power supplies. The DAQ system is shown in .

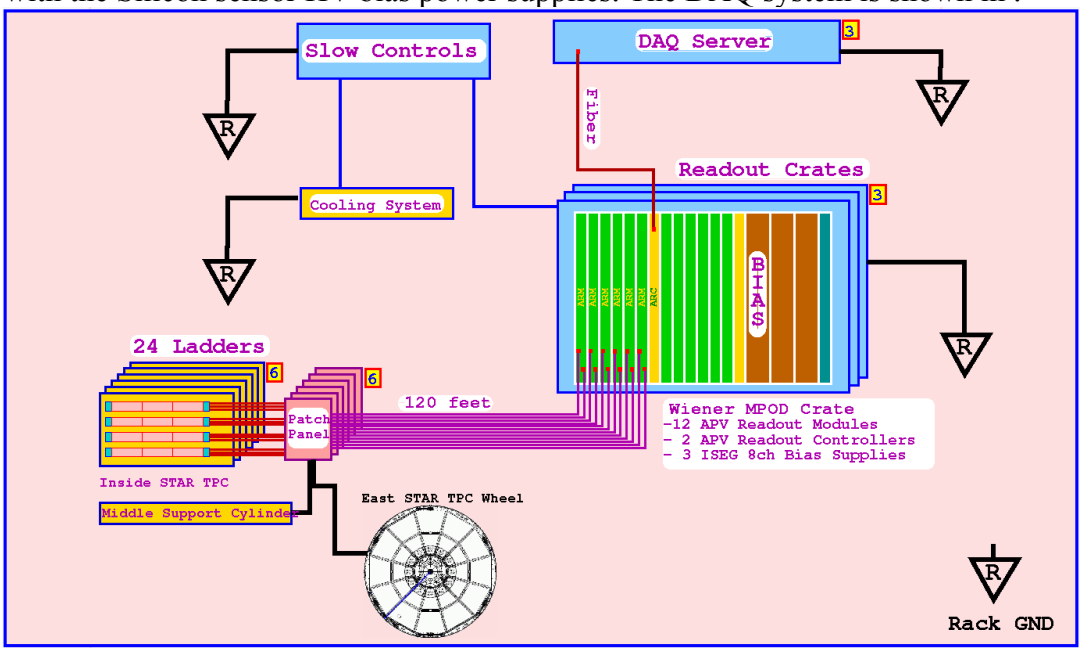


Figure 5-6: DAQ System for the FTS based on APV-chip readout.

### 5.4.5 Cooling System

The amount of heat generated by an APV chip is around 0.3 W. In order to keep the APV chips and Silicon sensors at low temperature, the APV chips need to be cooled. By replicating the cooling system of the STAR IST, as shown in , a cooling system can be readily used for the FTS.

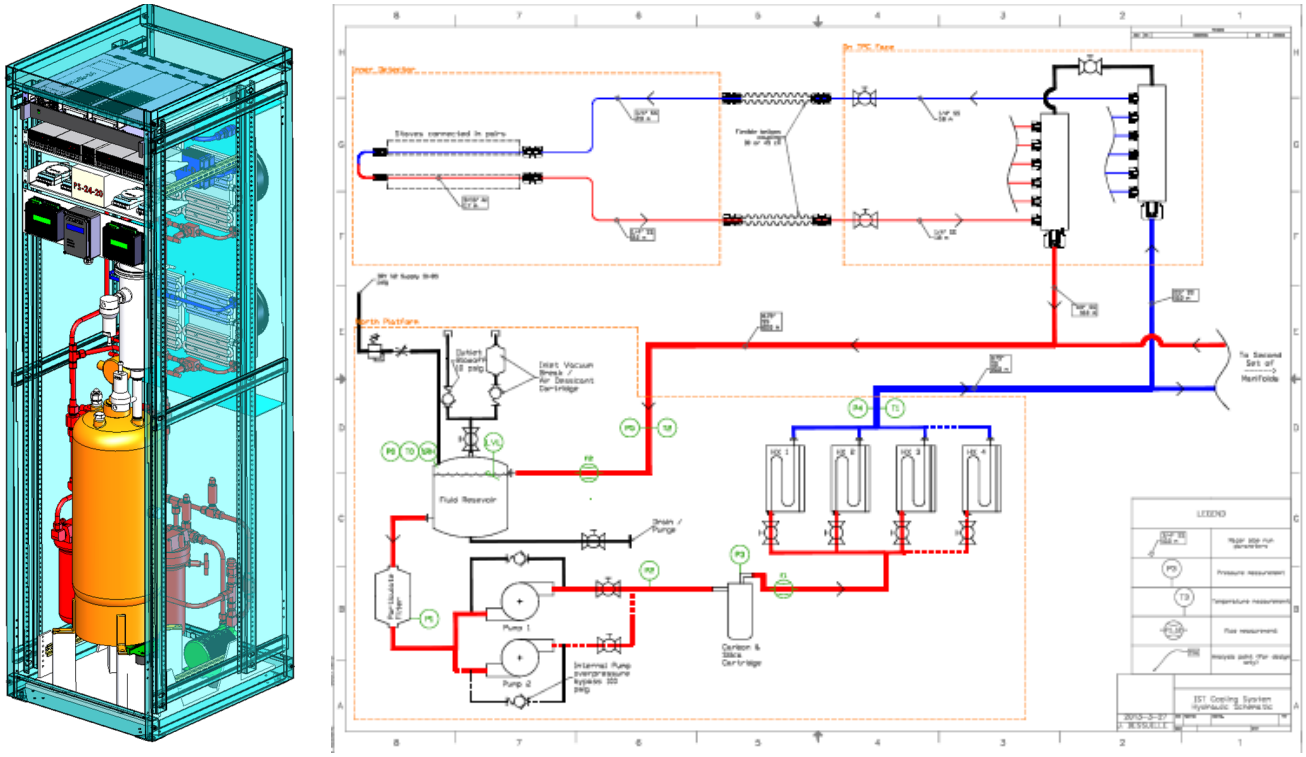

Figure 5-7: FTS cooling system. (Left) CAD drawing of the cooling system rack. (Right) Connections and flows.

### 5.4.6 Slow Control System

The slow controls system will serve as the primary means for controlling and monitoring the working parameters of the FTS. These parameters, such as temperatures, component currents and voltages will be interfaced with the standard STAR alarm system. The alarm system logs the parameter history and alerts the shift crews if operating limits are exceeded. The slow controls for the FTS and readout crates will be handled exclusively by Ethernet traffic to the FTS Linux box, through the ALICE DDL link to the readout crates, and then finally through the RDOs to the APV's via the local $I^2C$ link. There will be no other hardware needed for slow controls. All power supplies will be fitted with an Ethernet controls interface.

### 5.4.7 Radiation Exposure

The primary concerns in radiation damage to Silicon Ministrip detectors include possible damage to frontend readout chips by ionizing energy losses of charged particles, and to Silicon sensors by non-ionizing energy losses of hadrons. The former won't be a concern if APV chips would be chosen for the FTS. The APV chip was designed for the much higher radiation environment at the LHC. It is manufactured using an IBM 0.25μm radiation hard process and can tolerate 20+ Mrad radiation dose. The expected ionizing radiation exposure at STAR is orders of magnitude smaller, as shown in Table 5-1. From the running experience of the STAR IST at a radius of 14 cm from the beam, the non-ionizing radiation at RHIC is also small. After 14 weeks of Au+Au collisions at $\sqrt{s}$=200 GeV in 2014, the bias current increased by 1-2 μA per IST sensor, which has a volume of $0.03\times4\times7.7$ $cm^3$. This suggests that 1-MeV neutron equivalent fluence in

Run14 was les than $5\times10^{10}$ $cm^{-2}$. As the closest distance of the FTS sensor to the beam would be around 2.6 cm, the 1-MeV neutron equivalent fluence received in the proposed p+p and p+A running should be less than $1\times10^{13}$ $cm^{-3}$, which won't have a significant impact on the sensor performance. Therefore it can be safely assumed that radiation damage to the APV chips and Silicon sensors are not of a concern during normal data taking. Caution will be taken during beam injections and machine studies by turning off the powers to the APV chips and Silicon sensors.

| Radius [cm] | 200 GeV Au+Au [krad] | 500 GeV p+p [krad] |
|---|---|---|
| 2.5 | 5.3-28 | 29-133 |
| 14 | 0.2-1 | 1-4 |
| 22 | 0.1-0.4 | 0.4-2 |

Table 5-1: Radiation field in krad from physics collisions in the center of STAR extrapolated to RHIC II luminosities for different radial positions for 12 weeks of run time.

### 5.4.8 Additional R&D

To validate and optimize the FTS design based on the Silicon Microstrip detector technology, R&D is needed to develop appropriate Silicon Ministrip sensors to meet the requirements. STAR has started an R&D program to study this and anticipates that prototype sensors will be delivered and examined in 2017. It is also important to decide on the front-end readout chips. While the APV chip is attractive, as the full designs of backend readout and DAQ systems are available from the STAR IST detector, a survey of the chips available on the market will be performed before the final decision. In order to have a full system design for the FTS, mechanical designs for the FTS disk and support structure are needed. These will be investigated in the near future.

## 5.5 Survey and Alignment

The FTS planes will have to be aligned both with respect to each other, and with respect to the STAR reference frame. This will be achieved by survey measurements and ultimately by using tracks in p+p, p+A, and A+A collisions. In the Silicon-based FTS, the internal structure of the Silicon sensors will be known with an accuracy of better than 1 μm, far beyond the physics requirements. This information is obtained through the production mask drawings of the Silicon sensors and accessed through alignment marks on the Silicon sensors. The FTS planes and mechanic mounting structures will again be surveyed after their assembly and before the installation into STAR. Once the FTS is installed into STAR, tracks produced in p+p, p+A, and A+A collisions will travel through the FTS planes. The relative positions and rotations between FTS planes and between FTS and mid-rapidity detectors will be determined by using an iterative residual method for the reconstructed tracks.

## 5.6 Installation Procedure

Following cosmic-ray, source, and beam tests, the FTS will be transported to Brookhaven National Laboratory for final assembly and integration. It is planned to design and use a suitable extension of the existing West-Support-Cone internal rail structure on the West side of the STAR experiment, similar to the insertion mechanism of the FGT shown in Figure 5-8. Besides installation, this support will allow systematic in-situ tests of the FTS with STAR services as well as maintenance repair between RHIC runs without having to move the main detector to the assembly hall.

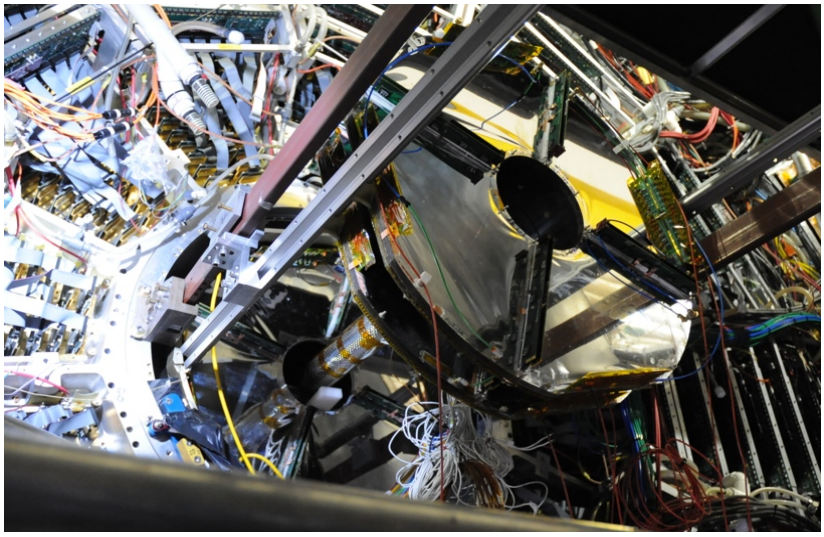

Figure 5-8: Rail setup for the STAR in-situ installation of the FGT subsystem. A similar concept is proposed for the FTS.

# 6 Project Cost, Schedule, and Management

Below is the cost information for FCS'.

FCS' WBS Level 3.

| WBS Number | WBS Description<br>**FCS' EMCal** | Base Cost | Contingency |
|---|---|---|---|
| y.1.1 | APDs | $200,000 | $30,000 (15%) |
| y.1.2 | Calibration System | $5,000 | $1,500 (35%) |
| y.1.3 | Readout Electronics (FEE/Digitizers/Cables) | $240,000 | $84,000 (35%) |
| y.1.4 | Light guides | $20,000 | $7,000 (35%) |
| y.1.5 | Calibration of FEEs (students labor 26% overhead) | $20,000 | $7,000 (35%) |
| Base Cost | | $485,000 | |
| Contingency | | $129,500 | |
| Total Cost | | $614,500 | |

| WBS Number | WBS Description<br>**FCS' HCal** | Base Cost | Contingency |
|---|---|---|---|
| x.1.1 | HAD Absorber Plates | $544,000 | $136,000 (25%) |
| x.1.2 | HAD Scintillator and WLS | $192,000 | $48,000 (25%) |
| x.1.3 | HAD Structural elements | $89,000 | $32,000 (35%) |
| x.1.4 | Mechanical Integration into STAR | $100,000 | $35,000 (35%) |
| x.1.5 | HAD Final Assembly Labor (stacking, students labor 26% overhead) | $40,000 | $14,000 (35%) |
| x.1.6 | APDs (exclusive of electronics) | $50,000 | $7,500 (15%) |
| x.1.7 | Calibration System | $5,000 | $1,500 (35%) |
| x.1.8 | Readout Electronics (FEE/Digitizers/Cables) | $56,000 | $20,000 (35%) |
| Base Cost | | $1,076,000 | |
| Contingency | | $294,000 | |
| Total Cost | | $1,370,000 | |

| WBS Number | WBS Description<br>**FCS' FPD** | Base Cost | Contingency |
|---|---|---|---|
| x.1.1 | Refurbished SiPM readout boards | $20,000 | $5,000 (25%) |
| x.1.2 | DEP readout electronics (Digitizers) | $25,000 | $9,000 (35%) |
| Base Cost | | $45,000 | |
| Contingency | | $14,000 | |
| Total Cost | | $59,000 | |

In addition, we provide the cost information for 4-disk FTS below.

FTS' WBS Level 3.

| WBS Number | WBS Description<br>**FTS (4-disk)** | Base Cost | Contingency |
|---|---|---|---|
| y.1.1 | Electronics | $1,100,000 | $385,000 (35%) |
| y.1.2 | Mechanics | $600,000 | $240,000 (40%) |
| y.1.3 | Assembly and Testing | $600,000 | $210,000 (35%) |
| y.1.4 | Integration | $450,000 | $225,000 (50%) |
| Base Cost | | $2,750,000 | |
| Contingency | | $1,060,000 | |
| Total Cost | | $3,810,000 | |

Adding two additional disks will add 1-1.5 million USD to the FTS project.

# 7 Bibliography


[1] STAR BES White-Paper, STAR Note 598 available from https://drupal.star.bnl.gov/STAR/starnotes
[2] A. Accardi et al, Electron Ion Collider: The Next QCD Frontier – Understanding the glue that binds us all, arXiv:1212.1701
[3] E.C. Aschenauer et al., eRHIC Design Study: An Electron-Ion-Collider at BNL, arXiv:1409:1633 (2014)
[4] The STAR Decadal Plan: http://www.bnl.gov/npp/docs/STAR_Decadal_Plan_Final[1].pdf
[5] A polarized p+p and p+A program for the next years, STAR Note 605 available from https://drupal.star.bnl.gov/STAR/starnotes
[6] eSTAR Letter-of-Intent: https://drupal.star.bnl.gov/STAR/starnotes/public/sn0592
[7] H1 Collaboration, F. Aaron *et al.*. JHEP, **01**:109, 2010. arXiv:0911.0884.
[8] G. Bunce, N. Saito, J. Soffer, and W. Vogelsang, *Ann. Rev. Nucl. Part. Sci.* **50** (2000) 525.
[9] B. Abelev *et al.* (STAR Collaboration), *Phys. Rev. Lett.* **97**, 252001 (2006).
[10] B. Abelev *et al.* (STAR Collaboration), *Phys. Rev. Lett.* **100**, 232003 (2008).
[11] L. Adamczyk *et al.* (STAR Collaboration), *Phys. Rev.* **D86**, 032006 (2012).
[12] STAR Collaboration, arXiv: 1405.5134 [hep-ex], submitted to PRL.
[13] R. D. Ball et al., Nucl. Phys. **B 849**, 112 (2011) [Errata: ibid **854**, 926 (2012) and **855**, 927 (2012)]; R. D. Ball et al., Nucl. Phys. **B 855**, 608 (2012).
[14] D. de Florian, R. Sassot, M. Stratmann, and W. Vogelsang, Phys. Rev. Lett. **113**, 1 (2014).
[15] E.R. Nocera et al, Nucl. Phys. **B887**, 276 (2014).
[16 ] E. Leader, A.V. Sidorov, and D.B. Stamenov, Phys. Rev. D 82, 114018 (2010).
[17] M. Stratmann, *Word Scientific - DIS 2006 Conference (Tsukuba, Japan)* **1**, 715 (2006).
[18] M. Walker, PhD Thesis, MIT (2011), B. Page, PhD Thesis IUCF (2013).
[19] A. V. Efremov and O. V. Teryaev, Sov. J. Nucl. Phys. 36, 140 (1982) [Yad. Fiz. 36, 242 (1982)]; Phys. Lett. B 150, 383 (1985). J.-W. Qiu and G. F. Sterman, Phys. Rev. Lett. 67, 2264 (1991); Nucl. Phys. B 378, 52 (1992); Phys. Rev. D 59, 014004 (1999)
[20] L. Adamczyk et al., Phys. Rev. **D 89** (2014) 012001; arXiv:1309.1800
[21] B. I. Abelev *et al.*, Phys. Rev. Lett. **101**, 222001 (2008), arXiv: 0801.2990
[22] L. Adamczyk et al., Phys. Rev. **D 86** (2012) 051101; arXiv:1205.6826
[23] K. Kanazawa, Y. Koike, A. Metz, D. Pitonyak, arXiv:1404.1033.
[24] S. Heppelmann, CIPANP-2012, https://indico.triumf.ca/getFile.py/access?contribId=349&sessionId=44&resId=0&materialId=slides&confId=1383
[25] B. I. Abelev *et al.* (STAR Collaboration), Phys. Rev. Lett. **101**, 222001 (2008).
[26] M. M. Mondal, talk at DIS-2014: http://indico.cern.ch/event/258017/session/6/contribution/216/material/slides/1.pptx
[27] P. Sun and F. Yuan, Phys. Rev. D. 88 (2013) 114012
[28] P. Sun, J. Isaacson, C.-P.Yuan and F. Yuan aeXiv:1406.3073
[29] M.G. Echevarria, A. Idilbi, Z.-B. Kang and I. Vitev, Phys. Rev. **D 89** (2014) 074013, arXiv:1401.5078
[30] J. Collins, arXiv:1409.5408
[31] Z.-B. Kang and J.-W. Qiu, Phys. Rev. Lett. **103** (2009) 172001, arXiv:0903.3629
[32] A. Metz and J. Zhou, Phys. Lett. B **700** (2011) 11, arXiv:1006.3097
[33] S. Fazio, talk at DIS-2014, http://indico.cern.ch/event/258017/session/11/contribution/219/material/slides/0.pptx
[34] E.A. Hawker et al., Phys. Rev. Lett. **80**, 3715 (1998)
[35] J. Ralston and D.Soper, Nucl. Phys. **B 152**, 109 (1979).
[36] R. Jaffe and X. Ji, Nucl. Phys. **B 375**, 527 (1992).
[37] P. Mulders and R. Tangerman, Nucl. Phys. **B 461**, 197 (1996).
[38] J. C. Collins, Nucl. Phys. **B 396**, 161 (1993).
[39] J. C. Collins, S. F. Heppelmann, and G. A. Ladinsky, Nucl. Phys. **B 420**, 565 (1994).
[40]A. Airapetian *et al*. (HERMES Collaboration), Phys. Rev. Lett. **94**, 012002 (2005); **103**, 152002 (2009); Phys. Lett. **B 693**, 11 (2010).
[41] V. Y. Alexakhin *et al*. (COMPASS Collaboration), Phys. Rev. Lett. **94**, 202002 (2005); E. S. Ageev et al. (COMPASS Collaboration), Nucl. Phys. **B 765**, 31 (2007); M. G. Alekseev et al. (COMPASS Collaboration), Phys. Lett. **B 673**, 127 (2009); M. G. Alekseev et al. (COMPASS Collaboration), Phys. Lett. **B 692**, 240 (2010); C. Adolphetal. (COMPASS Collaboration), Phys. Lett. **B 717**, 376 (2012); N. Makke (COMPASS Collaboration), arXiv:1403.4218.
[42] A. Airapetian *et al.* (HERMES Collaboration), JHEP **0806**, 017 (2008).

[43] C. Adolph *et al*. (COMPASS Collaboration), Phys. Lett. **B 713**, 10 (2012).
[44] R. Seidl *et al.* (Belle Collaboration), Phys. Rev. Lett **96**, 232002 (2006); Phys. Rev. **D 86**, 039905(E) (2012).
[45] A. Vossen *et al.* (Belle Collaboration), Phys. Rev. Lett. **107**, 072004 (2011).
[46] M. Anselmino *et al.,* Phys. Rev. **D 75**, 054032 (2007); Nucl. Phys. B, Proc. Suppl. **191**, 98 (2009); Phys. Rev. **D 87**, 094019 (2013).
[47] A. Bacchetta, A. Courtoy, and M. Radici, Phys. Rev. Lett. **107**, 012001 (2011).
[48] K. Adkins, Proceedings Spin 2014
[49] A. Vossen, *Il Nuovo Cimento* **C 35**, 59 (2012).
[50] R. L. Jaffe and X. Ji, Phys. Rev. Lett. **67**, 552 (1991); Nucl. Phys. **B 375**, 527 (1992).
[51] A. Airapetian *et al.* (HERMES Collaboration)*,* Phys. Lett., **B 577**:37–46, 2003, arXiv:hep-ex/0307023; Phys. Lett. **B 684**:114–118, 2010. arXiv:0906.2478.
[52] W. Brooks and H. Hakobyan, Nucl. Phys, **A 830**:361c–368c, 2009. arXiv:0907.4606.
[53] W. Brooks, Physics with nuclei at an Electron Ion Collider. 2010. arXiv:1008.0131.
[54] M. Vasilev *et al*. (E866 Collaboration), Phys. Rev. Lett., **83**:2304–2307, 1999. arXiv:hep-ex/9906010.
[55] H. Paukkunen, DIS-2014, http://indico.cern.ch/event/258017/session/1/contribution/222/material/slides/0.pdf
[56] H. Weigert, Prog. Part. Nucl. Phys. **55** (2005) 461.
E. Iancu and R. Venugopalan, hep-ph/0303204.
F. Gelis, E. Iancu, J. Jalilian-Marian, and R. Venugopalan, Ann. Rev. Nucl. Part. Sci. **60** (2010) 463.
Y. V. Kovchegov and E. Levin, Quantum Chromodynamics at High Energy. Cambridge University Press, 2012.
J. Jalilian-Marian and Y. V. Kovchegov, Prog. Part. Nucl. Phys. **56** (2006) 104.
[57] I. Arsene *et al*. (BRAHMS Collaboration), Phys.Rev.Lett. **93**, 242303 (2004), nucl-ex/0403005.
[58] J. Adams *et al.* (STAR Collaboration), Phys.Rev.Lett. **97**, 152302 (2006), nucl-ex/0602011.
[59] A. Adare *et al.* (PHENIX Collaboration), Phys.Rev.Lett. **107**, 172301 (2011), 1105.5112.
[60] J. L. Albacete and C. Marquet, Phys.Rev.Lett. **105**, 162301 (2010), 1005.4065.
[61] Z.-B. Kang and F. Yuan, Phys.Rev. **D 84**, 034019 (2011), 1106.1375.
[62] Y.V. Kovchegov and M.D. Sievert, Phys. Rev. **D 86**, 034028 (2012), Erratum-ibid. **D 86**, 079906 (2012) arXiv:1201.5890.
[63] D. Boer, A. Dumitru, and A. Hayashigaki, Phys. Rev. **D 74** (2006) 074018.
D. Boer and A. Dumitru, Phys. Lett. **B 556** (2003) 33.
D. Boer, A. Utermann, and E. Wessels, Phys. Lett. **B 671** (2009) 91.
[64] Z.-B. Kang and F. Yuan, Phys. Rev. **D 84** (2011) 034019.
[65] Y. V. Kovchegov and M. D. Sievert, Phys. Rev. **D 86** (2012) 034028.
[66] J.-W. Qiu, talk at the workshop on "Forward Physics at RHIC", RIKEN BNL Research Center, BNL, 2012.
[67] T. Toll and T. Ullrich, arXiv:1307.8059 [hep-ph] (2013).
[68] T. Toll and T. Ullrich, Phys. Rev. **C 87**, 024913 (2013).
[69] H. Kowalski, L. Motyka, G. Watt, Phys. Rev. **D 74**, 074016 (2006).
[70] H. Kowalski and D. Teaney, Phys. Rev. **D 68**, 114005 (2003).
[71] S. Munier, A. M. Stasto and A. H. Mueller, Nucl. Phys. **B603**, 427 (2001).
[72] K. J. Eskola, H. Paukkunen and C. A. Salgado, JHEP **0904**, 065 (2009).
[73] H.L. Lai et al., Eur. Phys. J. **C12**, 375 (2000).
A.D. Martin, R.G. Roberts, W.J. Stirling, and R.S. Thorne, Eur. Phys. J. **C4**, 463 (1998).
[74] J. Jalilian-Marian, Prog.Theor.Phys.Suppl. **187** (2011) 123, arXiv:1011.1601.
[75] J. Jalilian-Marian and A. Rezaeian, Phys. Rev. **D 86**, 034016 (2012); A. Rezaeian, Phys. Rev. **D 86**, 094016 (2012).
[76] T. Sjöstrand, S. Mrenna and P. Skands, Comput. Phys. Comm. **178**, 852 (2008).
[77] Dijet production from PYTHIA-8.189 is scaled down due to its overestimation of inclusive $\pi^0$ yields than those reported by BRAHMS in Phys. Rev. Lett. **98**, 252001 (2007) and STAR in Phys. Rev. Lett. **97**, 152302 (2006).
[78] F. Arleo and S. Peigné, JHEP **03** (2013) 122.
[79] F. Arleo and S. Peigné, private communication.
[80] A. Adare *et al.* (PHENIX Collaboration), Phys. Rev. Lett. **107**, 142301 (2011).
[81] R. Aaij *et al.* (LHCb Collaboration), JHEP **1402** (2014) 072.
[82] B. Abelev *et al*. (ALICE collaboration), arXiv:1308.6726.
[83] E. Ferreiro, F. Fleuret, J.P. Lansberg and A. Rakotozafindrabe, Phys. Rev. **C 88** (2013) 047901.
[84] J. Albacete *et al.*, Int. J. Mod. Phys. **E 22** (2013) 1330007.
[85] J. Adams et al. (STAR Collaboration), Phys.Rev.Lett. 95, 152301 (2005); B. Abelev et al. (STAR Collaboration), Phys.Rev. C80, 064912 (2009); B. Alver et al. (PHOBOS Collaboration), Phys.Rev.Lett. 104, 062301 (2010); B. Abelev et al. (STAR Collaboration), Phys.Rev.Lett. 105, 022301 (2010).
[86] CMS Collaboration, Vardan Khachatryan et al. JHEP 1009 (2010) 091.

[87] CMS Collaboration, Serguei Chatrchyan et al., Phys. Lett. B718 (2012) 795; B. Abelev et al. (ALICE Collaboration), Phys.Lett. B719 (2013) 29; G. Aad et al. (ATLAS Collaboration), Phys.Rev.Lett. 110, 182302 (2013).
[88] B. Abelev et al. (ALICE Collaboration), Phys.Lett. B726 (2013) 164.
[89] A. Adare et al. (PHENIX Collaboration) (2014), 1404.7461. STAR paper to be submitted.
[90] B. Abelev et al. (ALICE Collaboration), Phys.Rev.Lett. 110, 082302 (2013).
[91] K. Dusling and R. Venugopalan, Phys.Rev. D87, 054014 (2013).
[92] BRAHMS Collaboration, I. Arsene et al., Nucl.Phys. A 757, 1 (2005); PHOBOS Collaboration,, B.B. Back et al., Nucl.Phys. A757, 28 (2005);STAR Collaboration, John Adams et al., Nucl.Phys. A 757, 102 (2005);PHENIX Collaboration, K. Adcox et al., Nucl.Phys. A 757, 184 (2005).
[93] U. Heinz and R. Snellings, Ann.Rev.Nucl.Part.Sci. 63,123 (2013).
[94] D. Teaney, Phys. Rev. C **68**, 034913 (2003); P. Romatschke and U. Romatschke, Phys. Rev. Lett. **99**, 172301 (2007); H. Song and U. W. Heinz, Phys. Rev. C **77**, 064901 (2008); K. Dusling and D. Teaney, Phys. Rev. C **77**, 034905 (2008); H. Song *et al*., Phys. Rev. Lett. **106**, 192301 (2011).
[95] J. Jia and P. Huo, Phys.Rev. C 90, 034905 (2014); Phys.Rev. C 90, 034915 (2014).
[96] J. Adams et al. (STAR), Phys. Rev. C 72, 014904 (2005); A. Adare et al. (PHENIX), Phys. Rev. Lett. 105, 062301 (2010); K. Aamodt et al. (ALICE), Phys. Rev. Lett. 107, 032301 (2011); S. Chatrchyan et al. (CMS), Eur. Phys. J. C 72, 2012 (2012); G. Aad et al. (ATLAS), Phys. Rev. C 86, 014907 (2012).
[97] C. Gale *et al*., Phys.Rev. Lett. 110, 012302 (2013).
[98] JET collaboration, Phys. Rev. **C 90**, 014909 (2014).
[99] D. Kharzeev, E. Levin, and M. Nardi, Nucl. Phys. A **730**, 448 (2004); **743**, 329(E) (2004); Nucl. Phys. A **747**, 609 (2005).
[100] J.E. Bernhard *et al*., arxiv:1502.00339.
[101] H. Wang et al. (STAR Collaboration), Nucl.Phys.A931 (2014)293.
[102] B. Schenke, P. Tribedy and R. Venugopalan, Nucl.Phys.A 931 (2014) 288.
[103] U. Heinz *et al*., arxiv:1501.06477.
[104] S. Pratt, E. Sangaline, P. Sorensen and H. Wang, arXiv:1501.04042.
[105] A Proposal for STAR Inner TPC Sector Upgrade (iTPC), https://drupal.star.bnl.gov/STAR/starnotes/public/sn0619
[106] Proposal for an Event Plane and Centrality Detector for BES II, (internal STAR note) https://drupal.star.bnl.gov/STAR/system/files/STAR_R_and_D_proposal_EPD.pdf
[107] D. Kharzeev, E. Levin, and M. Nardi, Nucl. Phys. A **730**, 448 (2004); **743**, 329(E) (2004); Nucl. Phys. A **747**, 609 (2005).
[108] L.G. Pang, Q. Wang et al., Phys.Rev. C 86, 024911 (2012); arXiv:1205.5019 .
[109] L.G. Pang, G.Y. Qin et al., arXiv:1410.8690 (2014); private communications.
[110] Z. Qiu and U. W. Heinz, Phys. Rev. **C84**, 024911 (2011), arXiv:1104.0650 [nucl-th] .[
[111] F. G. Gardim, F. Grassi, M. Luzum, and J.-Y. Ollitrault, Phys. Rev. **C85**, 024908 (2012), arXiv:1111.6538 [nucl-th] .
[112] A. Dobrin (ALICE), Nucl. Phys. **A904-905**, 455c (2013), arXiv:1211.5348 [nucl-ex] .
[113] G. Aad *et al.* (ATLAS Collaboration), https://atlas.web.cern.ch/Atlas/GROUPS/PHYSICS/CONFNOTES/ATLASCONF-2014-022 .
[114] See e.g. J. Dunkelberger et al, Fermilab All Experimenters Meeting, March 2014, http://www.fnal.gov/directorate/program_planning/all_experimenters_meetings/special_reports/Dunkelberger_T-1018_Slides_03_17_14.pdf
[115] E. Aschenauer, A. Kiselev et al, EIC Detector R&D Progress Report, project eRD1, Jan. 2015.
[116] M. Glück *et al*., *Phys. Rev.* **D63**, 094005 (2001).
[117] W. Vogelsang, private communication (2013).
[118] D. de Florian, *Phys. Rev.* **D79**, 114014 (2009).
[119] A. Accardi *et al.,* arXiv:1212.1701 (2012).
[120] D. Sivers, Phys. Rev. **D 41**, 83 (1990); 43, 261 (1991).
[121] L. C. Bland *et al.* ($A_N$DY Collaboration), arXiv:1304.1454.
[122] L. Gamberg, Z.-B. Kang, A. Prokudin, Phys. Rev. Lett. **110**, 232301 (2013).
[123] A. V. Efremov and O. V. Teryaev, Sov. J. Nucl. Phys. **36**, 140 (1982); Phys. Lett. **150B**, 383 (1985); J.-W. Qiu and G. Sterman, Phys. Rev. Lett. **67**, 2264 (1991); Phys. Rev. **D 59**, 014004 (1998).
[124] D. Boer and P. J. Mulders, Phys. Rev. **D 57**, 5780 (1998).
[125] T. Rogers, Phys. Rev. **D 88**, 1, 014002 (2013).
[126] Bernardi E *et al*. 1987, Nucl. Instr. & Meth. **A262**, 229.
[127] R.-D. Appuhn *et al.* 1996, *The H1 Lead/Scintillating-Fiber Calorimeter*, DESY 96-171.

[128] Y. Fisyak *et al*. 2014, Nucl. Instr. & Meth. A756, 68.
[129] D.A. Petyt *et al*. 2012, J. Phys. Conf. Ser.Vol 404, 012043.

[130] B. Alver et al (PHOBOS Collaboration), Phys. Rev. C83, 024913 (2011).
[139] J. Jia, S. Radhakrishnan, M. Zhou (2015), 1506.03496
[140] A. Bzdak, D. Teaney, Phys. Rev. C87(2), 024906 (2013), 1210.1965
[141] A. Monnai, B. Schenke (2015), 1509.04103
[142] A. Mazeliauskas, D. Teaney (2015), 1509.07492
[143] R.S. Bhalerao, J.Y. Ollitrault, S. Pal, D. Teaney, Phys. Rev. Lett. 114(15), 152301 (2015), 1410.7739
[144] G. Aad et al. (ATLAS), ATLAS-CONF-2015-051 (2015).
[145] V. Khachatryan et al. (CMS), Phys. Rev. C92(3), 034911 (2015), 1503.01692
[146] G. Aad et al. (ATLAS), Phys. Rev. C92(3), 034903 (2015), 1504.01289
[147] G. Aad et al. (ATLAS), Phys. Rev. C90(2), 024905 (2014), 1403.0489
[148] G. Denicol, A. Monnai, S. Ryu, B. Schenke , arXiv:1512.08231 [nucl-th]
[149] G.Denicol, A.Monnai and B.Schenke, arXiv:1512.01538 [nucl-th]
[150] ATLAS detector, Tech. Rep. ATLAS-CONF-2015-051, CERN, Geneva (Sep 2015). URL http://cds.cern.ch/record/2055672